1983

Picosecond photophysical processes in iodoanthracenes

Cristiano G. Morgante
Iowa State University

INFORMATION TO USERS

This reproduction was made from a copy of a document sent to us for microfilming. While the most advanced technology has been used to photograph and reproduce this document, the quality of the reproduction is heavily dependent upon the quality of the material submitted.

The following explanation of techniques is provided to help clarify markings or notations which may appear on this reproduction.

1. The sign or "target" for pages apparently lacking from the document photographed is "Missing Page(s)". If it was possible to obtain the missing page(s) or section, they are spliced into the film along with adjacent pages. This may have necessitated cutting through an image and duplicating adjacent pages to assure complete continuity.

2. When an image on the film is obliterated with a round black mark, it is an indication of either blurred copy because of movement during exposure, duplicate copy, or copyrighted materials that should not have been filmed. For blurred pages, a good image of the page can be found in the adjacent frame. If copyrighted materials were deleted, a target note will appear listing the pages in the adjacent frame.

3. When a map, drawing or chart, etc., is part of the material being photographed, a definite method of "sectioning" the material has been followed. It is customary to begin filming at the upper left hand corner of a large sheet and to continue from left to right in equal sections with small overlaps. If necessary, sectioning is continued again—beginning below the first row and continuing on until complete.

4. For illustrations that cannot be satisfactorily reproduced by xerographic means, photographic prints can be purchased at additional cost and inserted into your xerographic copy. These prints are available upon request from the Dissertations Customer Services Department.

5. Some pages in any document may have indistinct print. In all cases the best available copy has been filmed.

University Microfilms International
300 N. Zeeb Road
Ann Arbor, MI 48106

Morgante, Christiano G.

PICOSECOND PHOTOPHYSICAL PROCESSES IN IODOANTHRACENES

Iowa State University PH.D. 1983

Picosecond photophysical processes in iodoanthracenes

by

Cristiano G. Morgante

A Dissertation Submitted to the
Graduate Faculty in Partial Fulfillment of the
Requirements for the Degree of
DOCTOR OF PHILOSOPHY

Department: Chemistry
Major: Physical Chemistry

Approved:

Signature was redacted for privacy.

In Charge of Major Work

Signature was redacted for privacy.

For the Major Department

Signature was redacted for privacy.

For the Graduate College

Iowa State University
Ames, Iowa

1983

TABLE OF CONTENTS

CHAPTER 1. INTRODUCTION

A vast variety of interesting chemical dynamics occur on the picosecond or subpicosecond time scale. For example, the photophysics of vision-related molecules, internal conversion and intersystem crossing between excited electronic states, photodissociation and recombination processes, isomerization, rotational diffusion, proton and electron transfer, and relaxation and redistribution of nonthermal vibronic energy all can occur in this time regime, especially in the condensed phase (1, 2, 3). Almost all of the chemical and physical processes studied by chemists and biologists take place in the liquid phase, where the system of interest is constantly influenced by the microscopic and macroscopic properties of the solvent. With this consideration, a large number of investigators have applied picosecond laser technology to chemical systems in attempts to elucidate the dynamics and mechanisms of these solute-solvent interactions.

Our ability to monitor the evolution of dynamical systems quantitatively has always been contingent on the availability of experimental systems capable of producing the required time resolution. The first picosecond light pulses were generated in 1965 by passively mode-locking a ruby laser (4) and, soon thereafter in 1966, by passively mode-locking a neodymium:glass laser (5). Within two years, picosecond time-resolved experiments were being performed to establish ground state recovery times in the mode-locking dyes used to generate picosecond pulses (6, 7), and in other systems of intrinsically chemical interest (8).

Following those initial studies, the number of experiments utilizing picosecond techniques has grown substantially, producing copious experimental information which has demanded revision in radiationless relaxation theories and has prompted the creation of new areas in chemical dynamics (9).

One major area of investigation has utilized picosecond technology to elucidate reaction rates and mechanisms of photoexcited molecules. Consider a molecule that has been excited to its first excited spin-allowed state, usually designated S_1. The system can undergo a number of processes to dissipate its excess energy (Figure 1): fluorescence to the ground state; photodissociation in cases where a labile bond is energetically accessible; intersystem crossing (ISC), a spin-forbidden process in which the molecule crosses from one electronic state to another with different spin multiplicity; internal conversion (IC), a spin-allowed process of energy exchange between two electronic states of the same multiplicity; conformational changes to different isomers; or as is usually the case, a combination of several of these processes (10). All of these dissipation mechanisms are influenced by coupling between vibrational levels and electronic states, locations and shapes of potential surfaces, and interactions between the pumped molecule and its environment. These are amenable to theoretical descriptions only after enough experimental information has been compiled to establish a zero-order foundation.

Spectroscopists have employed both emissive and absorptive properties of molecules to gain dynamical information. Fluorescence detection

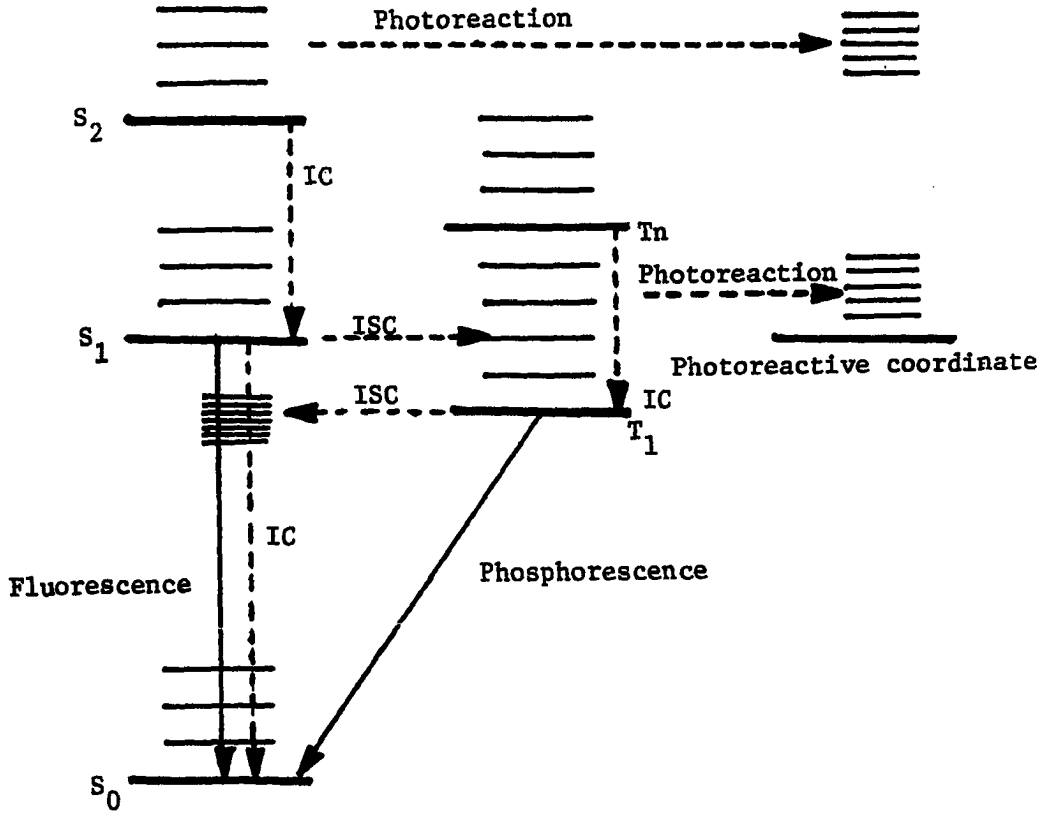

Figure 1-1. Typical relaxation pathways in excited molecules. Dashed lines indicate nonradiative processes; solid lines indicate radiative processes

is usually preferred owing to signal to noise considerations (11). With picosecond intermediates, however, absorptive techniques often have inherent advantages over fluorescence studies. The quantum yield of fluorescence depends on the lifetime and formation yield of the emissive state and its oscillator strength to the terminal state. If the emissive state is extremely short-lived due to competing relaxation avenues, such as in azulene (12), or has a poor radiative rate constant, as in the $^1(n,\pi^*)$ S_1 state of acridine in a hydrocarbon solvent (13), the quantum yield can be extremely small, and the fluorescence is correspondingly difficult to detect. In addition, absorption studies provide the only means of studying recovery times of a nonfluorescing ground state in photobleaching experiments.

A variety of schemes can be employed to implement absorptive experiments. Four common ones are shown in Figure 2. All of these represent variations of the "pump and probe" concept in which the reaction is initiated by a pump pulse which excites the system to a desired state. A second pulse delayed by a known time increment then probes the excited species. Modulation of the probe beam by the excited species is detected by changes in attenuation, gain, or frequency shift of magnitudes proportional to dynamically changing populations of the excited state.

Figure 2a illustrates the procedure used in one of the earliest picosecond experiments performed on azulene (8). Picosecond pulses were generated by a passively mode-locked Nd:glass laser. The 1.06 μm fundamental was used for probe pulses and the frequency-doubled wavelength 532 nm was used for pump pulses. Azulene's first excited state, S_1,

Figure 1-2. Four common schemes utilized in pump-probe experiments. Narrow solid lines indicate the excitation pulses; the dashed lines with arrows indicate nonradiative pathways. The broad solid arrows represent the time-resolved signal which is usually monitored during the experiment. Schemes (a-d) portray excited state fluorescence after biphotonic absorption, ground state recovery after photo bleaching, transient absorption, and gain of stimulated emission, respectively

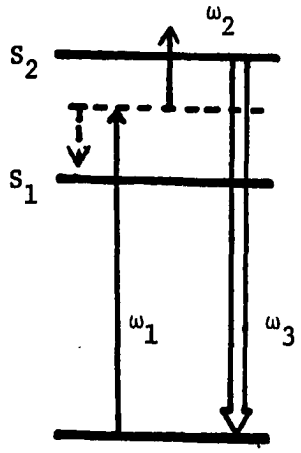
ω_2
S_2
S_1
ω_1
ω_3

(a)

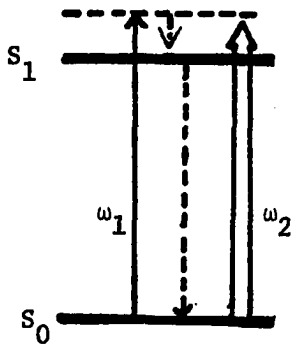
S_1
ω_1
ω_2
S_0

(b)

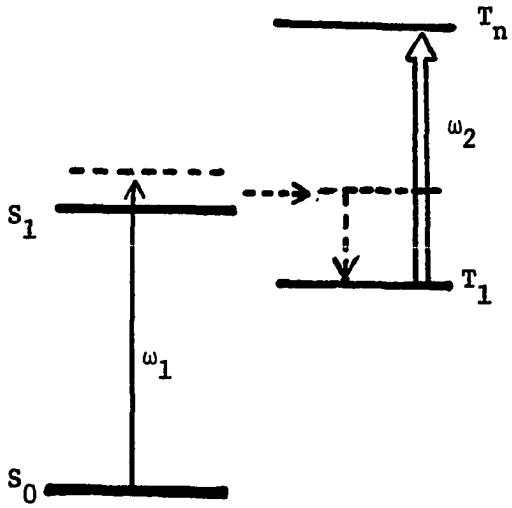
T_n
ω_2
S_1
T_1
ω_1
S_0

(c)

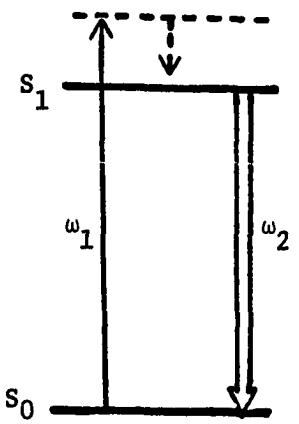
S_1
ω_1
ω_2
S_0

(d)

exhibits negligible fluorescence (fluorescence quantum yield, $\phi_f \sim 10^{-6}$, (8)), whereas its second excited state, S_2, has a modest fluorescence yield of 0.031 (14). This disparity in fluorescence yields was exploited to monitor the populations in the two states. The pump photon had only enough energy to populate a lower vibrational level in the S_1 state. When a probe pulse encountered a molecule in the excited vibronic S_1 level, it promoted it into the fluorescent S_2 state (at the energy ω_2 in Figure 2a). The amount of fluorescence (denoted by ω_3 in Figure 2a) observed is proportional to the number of molecules the probe beam encountered. By varying the time delay between the pump pulse and probe pulse and correlating this delay with fluorescence intensity, Rentzepis established the decay rate of the vibronic level of S_1 in azulene. It is interesting to note that this first experiment in picosecond spectroscopy depended on the fortuitous matching of the electronic states of azulene with picosecond laser wavelengths available in 1968. Although this technique has been used to gain further information on azulene (12, 15, 16), and has been extended to several other organic systems (17, 18), chemical physicists needed more flexible procedures for application to a wider class of systems.

Ground state bleaching (GSB), Figure 2b, has been used to study the repopulation kinetics of number of molecules, especially organic dyes (6, 7, 19, 20, 21). In this scheme, an intense pump pulse is strongly absorbed by the ground state of the molecule, depleting its ground state population. As these molecules subsequently decay back into the ground state, the weaker probe pulse, often at the same wavelength as the

excitation pulse, becomes attenuated through absorption by the molecules which have relaxed. The decay of probe beam transmission from its maximum at coincidence with the excitation pulse to a constant absorption at long times gives an estimate of the recovery time of the system. This method does not unambiguously delineate by which route the system is decaying--ISC, IC, dissociation, etc.--but does give information on the overall rate for relaxation back to the ground state.

Figure 2c represents the extension into the ultrafast regime of the flash photolysis technique, pioneered by Norrish and Porter (22) in transient absorption studies on the microsecond timescale. This pump and probe method has been utilized with a great deal of success in investigating a wider variety of dynamic phenomena. After the system has been excited, it can evolve into a number of different transients, each with a characteristic time-dependent absorption spectrum. The transient absorption can then be probed either by a single wavelength (23, 24) or by a probe pulse containing a continuum of wavelengths (25, 26) to gain dynamical information about the system. The proper use of a picosecond continuum as the probe beam enhances the utility of the technique by allowing one to observe different transients simultaneously, and to extract accurate dynamical data in situations in which overlapping transient bands complicate the interpretation of single-wavelength studies (27). One important process that can only be followed by using a continuum is spectral evolution (28, 29). By observing how the spectral distribution of a transient evolves over time, coupling between the vibrational model and electronic states and/or phonons can be evaluated,

and knowledge on how excess energy is randomized in the system can be obtained (30).

Although Figure 2c depicts an absorption from a triplet state, the method is not limited to triplet state detection, as several experiments have been carried out on excited state absorption from singlets (31, 32).

The last technique, illustrated in Figure 2d, measures the gain rather than the attenuation of the probe. This scheme has been used to measure the internal conversion process of S_2 to S_1 in cresyl violet (33). The molecule was excited to its second excited state, S_2, and probed at a wavelength corresponding to the maximum in the fluorescence spectrum of the S_1 state. As the population of S_1 increased due to relaxation of S_2 by IC, the probe beam experienced gain because of stimulated emission. A correlation between gain of the probe with the optical path delay variation between pump and probe allowed an estimation of the rate of internal conversion between S_2 and S_1.

In summary, Figure 2a-d limns some of the concepts that have been used and still are in use today to perform picosecond absorption spectroscopy. The following sections of this chapter review a number of related experiments that have been done in order to put the experiment described in this dissertation in perspective, and to compare the various approaches used to elucidate ultrafast mechanisms in molecular systems.

The generation of picosecond pulses for spectroscopic applications has been principally accomplished by two types of laser systems--passively mode-locked solid state lasers, of which neodymium:glass has

been the most frequently used, and synchronously pumped or passively mode-locked dye lasers. Both systems have unique features which both extend and limit their capabilities.

Absorption Experiments Utilizing Solid State Laser Systems

Ever since the first picosecond pulses were generated in solid state lasers (4, 5), solid state lasers have been used extensively by spectroscopists. The three major types that have been employed are the neodymium:glass, neodymium:YAG and ruby lasers. The minimum pulse duration, Δt, of any laser system is governed by its pulse frequency bandwidth, $\Delta\omega$, through the uncertainty principle (34). Represented in mathematical form, the time-band width product

$$\frac{\Delta\omega\ \Delta t}{2\pi} \geq K\ , \qquad (1.1)$$

where the value of K depends on the pulse shape and is on the order of unity.

In the neodymium:glass laser, the neodymium ion is surrounded by an amorphous glass environment which results in an inhomogeneously broadened fluorescence bandwidth of approximately 250 Å. In comparison, the active ions of the Nd:YAG or ruby are imbedded in a single-crystalline environment which results in narrower fluorescent bandwidths on the order of 5 Å (35). The disparity in spectral properties between glass and crystalline hosts manifests itself in the minimum pulse durations routinely available. A passively mode-locked Nd:glass laser has produced pulses reportedly optimized to 1-3 ps fwhm (36, 37) and typically 6-8 ps fwhm,

whereas Nd:YAG and ruby generally produce pulses in the 20-50 ps range (38, 39). This lack of temporal resolution in the crystalline systems has resulted in the widespread use of Nd:glass systems, especially before the development of picosecond dye lasers.

The theory of mode-locking, detailed characteristics of the Nd:glass laser system, and its attendant detection and data analysis systems will be treated in Chapter 2. The laser fundamental wavelength is 1.06 μm, with a typical pulse duration of 6-10 ps fwhm. Since the pulses have energies in the millijoule range, the peak powers are on the order of gigawatts per pulse. Because of these large power densities, the generation of shorter wavelengths and production of continuum pulses through nonlinear optical processes are relatively facile, with conversion efficiencies of about 15-20% for second and third harmonic generation. The second, third, and fourth harmonic wavelengths are 532 nm, 354 nm and 256 nm, respectively, and are thus common excitation wavelengths in picosecond spectroscopy. The spectral characteristics of the continuum are the result of more complicated nonlinear phenomena, and the discussion of its generation will be treated in detail in Chapter 3. It has been demonstrated that usable picosecond continua can be generated throughout the visible and near IR regions of the spectrum. One of the disadvantages of a Nd:glass system is its agonizingly slow repetition rate--normally one shot per minute--which translates into very tedious data collection and an inability to use signal averaging techniques. Another liability is the poor shot-to-shot reproducibility of the laser pulses. This characteristic is primarily due to the statistical nature

of the pulse generation inside the cavity. This handicap has led researchers to try to acquire as much information as possible per shot to minimize the effects of these shot-to-shot pulse fluctuations.

Finally, the Nd:glass oscillator system is a temperamental beast, and stringent controls on environment, stability of cavity supports, and immaculate optical surfaces must be maintained to keep the system stabile long enough to do an experiment.

The first experiments done on molecular systems using solid state lasers were done by Rentzepis (8) on azulene as described above. Malley and Rentzepis (40) introduced a new "crossed beam" technique, illustrated in Figure 3, which allowed the relaxation history of the sample to be taken with one shot. In this arrangement, the probe beam and the pump beam propagation directions were mutually perpendicular. The pump beam's optical path length through the sample cell was long enough so that with proper timing, it was entirely within the cell when the interrogating probe passed through the cell. The probe pulse, prior to being directed into the cell, had been spatially broadened by a Ronchi ruling. As with the previously described technique, the pump pulse left a wake of excited molecules which was instantaneously probed when the probe intersected the excited region. In this experiment, the ground state recovery of Kodak #9860 dye (used for mode-locking Nd:glass lasers) was being investigated. The probe pulse after passing through the sample cell was directed onto Polaroid Type 413 film where light exposure levels gave an indication of the spatial (and hence time) variation in attenuation. An inherent time resolution limitation of this

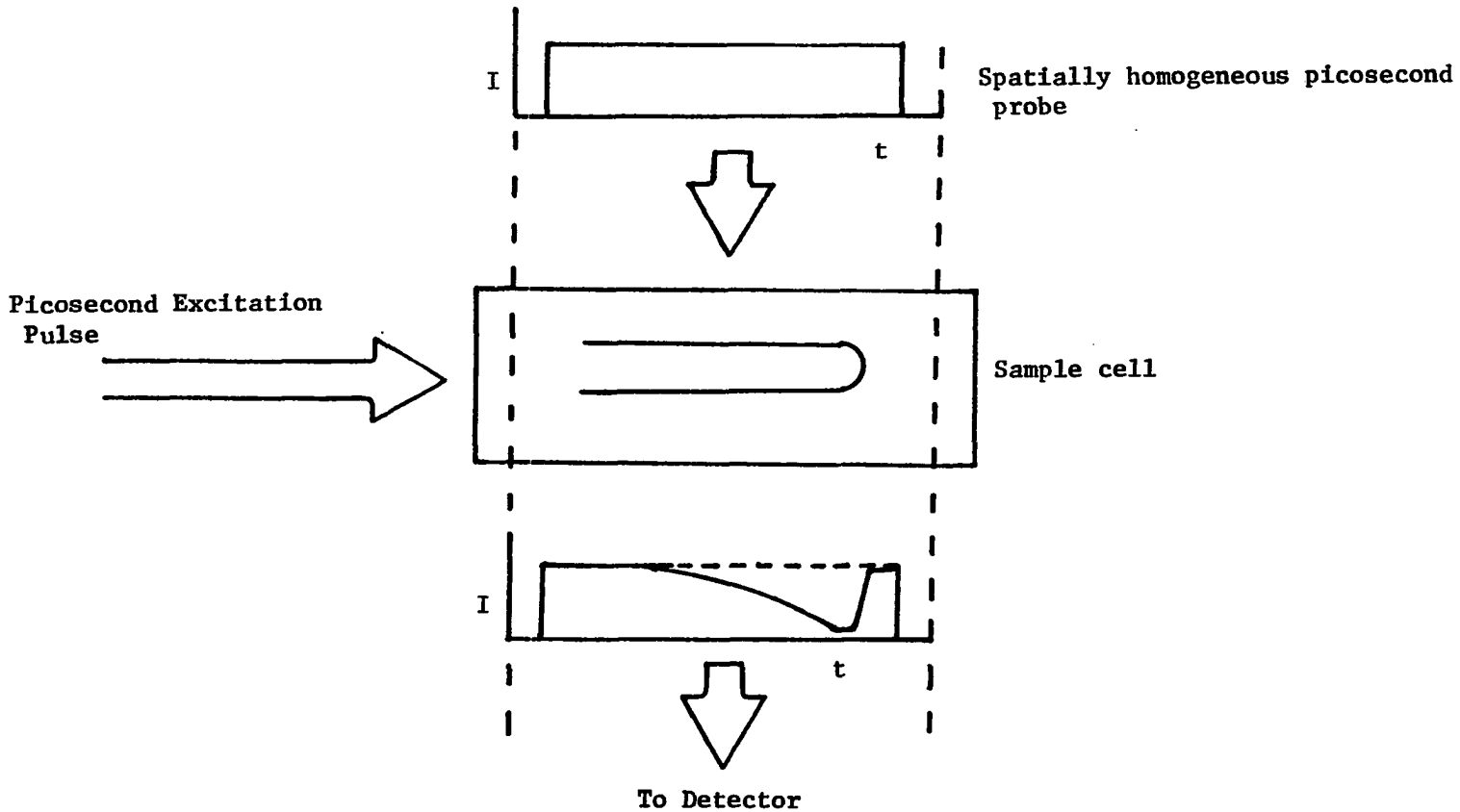

Figure 1-3. The crossed-beam technique

method consists in that the excitation pulse moves as it is being interrogated due to the finite propagation time of the probe pulse. This can be minimized by cells which are thinner along the path of the probe pulse if one increases the optical density of the sample.

A significant advancement in the application of single picosecond pulses to experiments was the introduction of the echelon (41). A transmission echelon is a stepped stack of glass plates which transforms a spatially broadened incident pulse into a series of time-delayed, parallel pulses because different portions of the incident pulse pass through different optical path lengths. The transmission echelon is acceptable if only one wavelength is being passed; however, when the pulse has a significant frequency bandwidth, as in a continuum, then a reflection echelon should be used to avoid the time dispersion caused by the frequency dependence of the refractive index of the glass plates. Both types of echelons are illustrated in Figure 4. The use of the echelon permits the collinear propagation of the excitation beam and probe. Each spatially separated probe pulse samples a different region of the excited ensemble of molecules at a known time after excitation. Again, information spanning a wide time range of stepped delays is obtained with one shot. A major caveat is the concomitant demand for spatial homogeneity of the excitation beam. The probe samples different spatial regions of the excited cross section, and therefore the excited region must be as uniform as possible. This requires the laser to be operated in the lowest order TEM_{00} mode (see Chapter 2). This technique was first applied in an absorption study to investigate the formation time of

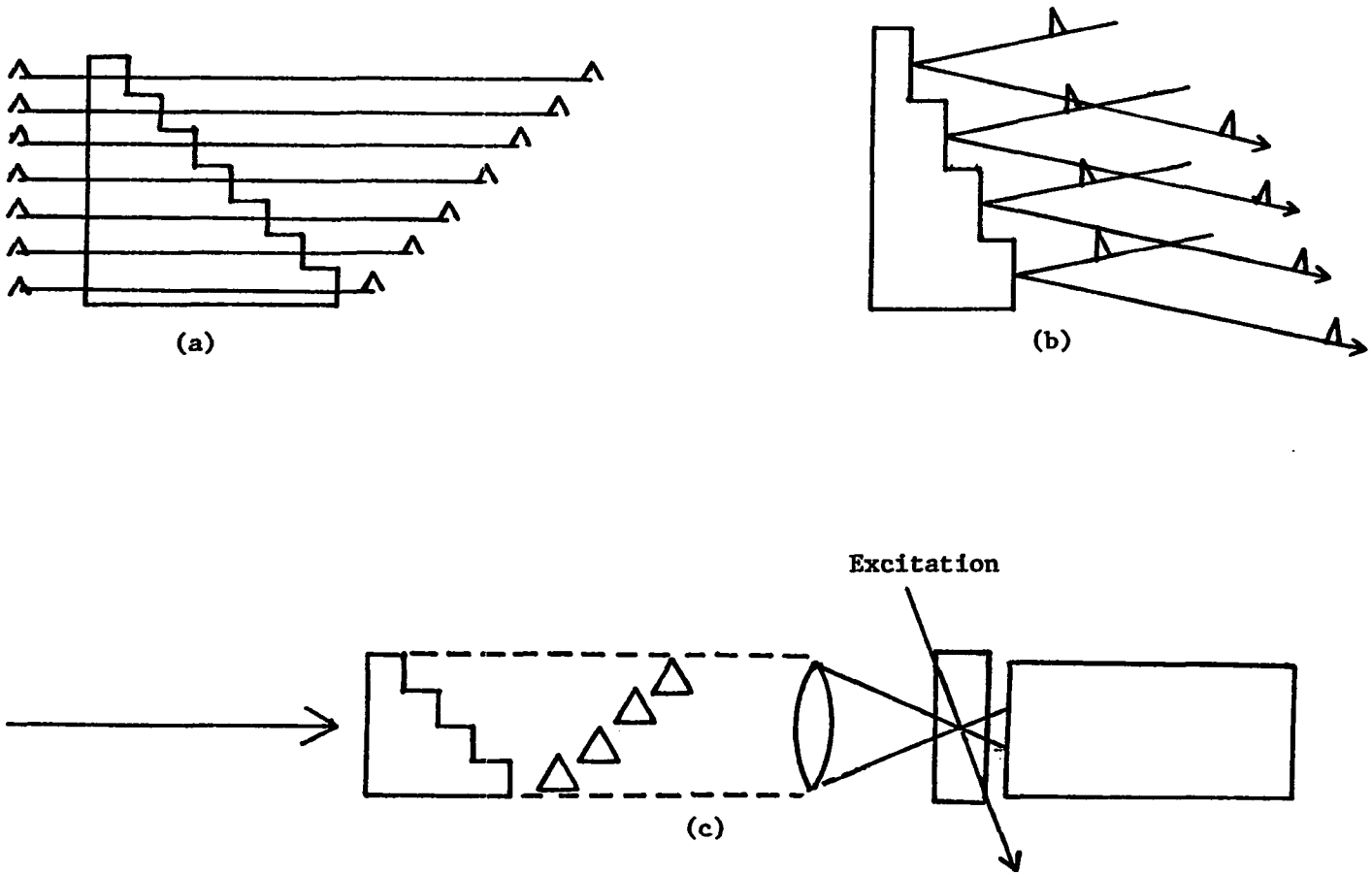

Figure 1-4. Use of (a) a transmission echelon or (b) reflection echelon to disperse a picosecond light pulse temporally. A typical experimental set up utilizing a transmission echelon is shown in (c)

prelumirhodopsin, which was also the first time picosecond spectroscopy was used to obtain information about a biophysical phenomenon (42).

Prelumirhodopsin is formed from rhodopsin by a cis-trans isomerization that occurs on the retinal appendage of the molecule. It is distinguishable from rhodopsin in solution by its strong absorption at 561 nm, at which wavelength the former only absorbs weakly. It was the growth in optical density in this spectral region that permitted the dynamics of this photoisomerization to be followed.

A 532 nm pulse was split into two beams. One was used as the excitation source for the rhodopsin; the other was directed into a cell of benzene to generate a new pulse at 561 nm by stimulated Stokes Raman scattering. This 561 nm pulse was then reflected off an echelon that introduced a 2 ps delay between the train of parallel probe pulses, and focussed into the excited rhodopsin sample. The absorption of the probe pulse was, within experimental error, simultaneous with the excitation pulse, implying that the evolution of rhodopsin into prelumirhodopsin occurs within 6 ps, the time resolution of the experiment.

This experiment, aside from introducing the echelon into picosecond spectroscopy, illustrated the use of nonlinear techniques, in this case stimulated Raman scattering, to overcome the lack of tunability of solid state laser systems. The use of the echelon has since been incorporated into picosecond experiments by a number of research groups (43-45) besides Rentzepis' group at Bell Laboratories.

As mentioned earlier, a picosecond continuum is a crucial tool for overcoming the limitations of a nontunable laser. The continuum, when

coupled with an echelon and a vidicon-Optical Multichannel Analyzer (OMA), can produce a three-dimensional plot of wavelength, time, and intensity of a dynamical process in a single shot (46).

Applications of picosecond continuum pulses were soon realized (47-50) after their suggestion by Alfano and Shapiro in 1971 (25). Busch et al. utilized a continuum and an echelon to study the ground state recovery time of DODCI (47). Magde et al. (48, 49) used a translation stage that delayed the probe pulse with respect to the excitation pulse by changing the transversed optical path length. This eliminated the need for an echelon and hence reduced the rigorous demand for spatial uniformity of the pump beam. Another benefit of using a translation stage to create time delays between pulses is that the delays can be continuously varied rather than incremented as in an echelon, and the time range spanned can be much longer if one builds an extremely stable sliding rail for the stage.

The ability to monitor kinetic processes over a wide range of wavelengths has been responsible for extending picosecond absorption techniques into a much larger arena of natural phenomena.

Greene et al. (27) have extensively explored radiationless relaxation processes in aza-aromatics and ketones. Netzel et al. have done studies on electron transfer mechanisms in porphyrins (51) and the charge transfer characteristics of polypyridine complexes of Iron (II), Ruthenium (II) and Osmium (II) (52). Other groups have studied photodissociation in $Cr(CO)_6$ and $Mn_2(CO)_{10}$ (53, 54).

It is likely that picosecond transient absorption spectroscopy

utilizing solid state laser systems will continue to be employed predominantly throughout the field in the short term for a number of reasons. Picosecond spectroscopists have learned a great deal about the nature of the continuum and its peculiarities and how to compensate for them (see Chapter 3). Moreover, innovations in laser technology have improved the capabilities of solid state systems. New neodymium:phosphate laser glasses (55), better mode-locking dyes (56), and improved cavity design (57) have led to solid state systems with pulses of 1.7 ps duration and repetition rates of 5 Hz. Detector systems have also improved considerably. Intensified silicon vidicons and microprocessor-controlled data acquisition systems offer substantial improvements in ease of collection and analysis. Finally, although dye laser pulses can be amplified to the power densities needed to generate usable continua, it is still a very difficult and tedious task (58). It will require novel advances in dye laser technology before such systems will be capable of producing pulses of high power and still maintain the current advantages dye lasers have over solid state systems.

Picosecond Absorption Experiments Utilizing Dye Lasers

Organic dyes are an ideal medium for the generation of picosecond and subpicosecond pulses since their fluorescent bandwidth is so large (10-100 nm). As mentioned in the first section, this implies that the theoretical pulse durations can be on the order of tens of femtoseconds, and a number of labs have produced 300 femtosecond fwhm pulses (59-62). Recently, a group has reported 35 femtosecond pulses (63).

Besides their intrinsic capability to generate extremely short pulses, dye lasers have potentially a wide wavelength tunability. Picosecond dye laser pulses have been produced by various techniques in the visible, ultraviolet and near IR (64, 65, 66). Another significant property is that they can have high repetition rates ranging from 200 MHz to single shots. Finally, the low pulse energies, about 1 nanojoule, avoid inducing complicating nonlinear optical processes in the sample under study--a nontrivial concern with high power solid state systems (46).

There are two major types of picosecond dye lasers that are presently in use for picosecond transient absorption: passively mode-locked dye lasers and synchronously mode-locked dye lasers. The passively mode-locked was developed independently by two research groups in 1972 (67, 68). Typically, a rhodamine 6G dye laser is pumped by a cw argon ion laser. The saturable absorber dye, DODCI, is used to mode-lock the laser and can be either inside the cavity in a separate jet stream, in contact with a mirror, or mixed with the laser dye. Malachite green, another dye, is often mixed in with DODCI to improve the stability of the pulses (67). Until recently, it has been with these systems that subpicosecond pulses have been generated the most reliably. Passive mode-locking is extremely dependent on the accurate matching of the lasing region of the gain medium and the absorption region of the mode-locking dye. This factor has significantly reduced the tunability of passively mode-locked systems. Continuous tuning while maintaining subpicosecond duration of the pulses has only been achieved in the region

580 nm to 615 nm (69).

Passively mode-locked systems have been used in a number of experiments. The high repetition rate of these systems allows the application of powerful signal averaging techniques that permit observation of extremely weak transient absorption signals. The lifetime of the lowest excited singlet state, S_1, of azulene was investigated by using the subpicosecond resolution of the passively mode-locked system (70). In a manner similar to Rentzepis' initial study of azulene (8), Ippen et al. found that the S_1 state had a lifetime of 1.9 ps and the ground state repopulation in azulene was 1.9 ps. This tends to indicate that the major deactivation pathway in azulene is internal conversion (71) rather than ISC.

In biological processes, the dynamics of the formation of bathobacteriorhodopsin from excited bacteriorhodopsin was followed by observing the increase in absorption with time of the probe pulses delayed with respect to the excitation pulses (72). The procedure used is again conceptually the same as applied by Rentzepis and coworkers in their study on prelumirhodopsin (42). Other experiments have been done on photodissociation of hemoglobin (73), the optically induced changes in surface reflectivity in GaAs (74), and in reverse charge-transfer mechanisms in azurin, a copper protein (75). All of these phenomena exhibit reaction times that occur in a picosecond or less, underscoring the need for systems capable of time resolution on the subpicosecond time scale.

The second type of dye laser, the synchronously mode-locked laser,

is gaining wide acceptance among picosecond spectroscopists because of its wavelength tunability, high repetition rate, good pulse to pulse stability and ease of operation (76). The synchronously pumped laser system has two component lasers: a mode-locked cw ion laser (argon or krypton) and a dye laser with a cavity length either identical to or a submultiple of the cavity length of the pump laser. The mode-locked pulses of the ion laser are generated by an acousto-optic modulator controlled by an extremely stable (better than 1 part in 10^6 Hz) radio-frequency source. Since the cavities of the two lasers are of the same length, the gain of the dye is driven in synchrony with the pump pulses. The dye laser pulse that circulates in the cavity intersects the excited dye molecules simultaneously with the ion laser pump pulse, because its round trip time is the same as the pump pulse repetition rate.

The pulse shortening mechanism is primarily due to two factors: the finite risetime in the gain under the influence of the ion pump pulse, and the depletion of the gain medium by stimulated emission when the dye pulse passes through the dye sheet. The mechanism has been treated in detail by Icsevgi and Lamb (77).

The first synchronously pumped dye lasers were demonstrated in 1968 using high power mode-locked ruby lasers and Nd:glass lasers (78-80). These systems were not extensively utilized and synchronous-pumped system pumped by an actively mode-locked argon ion laser appeared in 1974 (81).

The application of synchronously pumped dye lasers to picosecond absorption spectroscopy has not necessitated substantial modifications in the "pump and probe" concepts, except to take advantage of the high

repetition rates to signal average the data, thereby increasing its precision. The high repetition rate is capitalized on by the use of lock-in amplifier detection. There are some artifacts that are peculiar to dye laser systems, most noticeably coherence coupling phenomena (82, 83) that must be corrected before drawing conclusions from the information collected.

The synchronously pumped dye laser has found wide use in picosecond fluorescence studies, especially when interfaced with a photon-counting apparatus (76). It is interesting to note that the merging of synchronously pumped lasers, supersonic jets and photon-counting techniques has resulted in some extremely interesting dynamical observations (84, 85). The recent observation of quantum beats in a large molecule (86) illustrates the value of these newer techniques.

One method of measuring orientational relaxation of a molecule in a solvent is anisotropic absorption. Synchronously pumped dye lasers have been effectively used to perform these experiments. The method, as described by Shank et al. (87, 88), consists of having both the probe and pump beams linearly polarized and oriented with a 45° angle between their polarization axes. When the pump passes through the system, it creates an anisotropic distribution by saturating the absorption of molecules aligned parallel to the pump polarization. As the probe beam passes through this excited region, the component of the probe which is parallel to the pump polarization is absorbed less than the perpendicularly polarized component. This causes the probe beam to be rotated from its initial orientation and allows partial transmission of the probe

through a polarizer crossed with respect to the initial probe polarization. The signal monitored is this transmitted probe intensity which decays as the anisotropic distribution randomizes.

G. R. Fleming's group at Chicago has applied this technique to study the rotational reorientation time of DODCI as a function of viscosity and temperature (89, 90), and to test the validity of various hydrodynamic models of orientational diffusion of molecules in solution (91).

Although the tunability of synchronously pumped lasers is far better than the tunability of passively mode-locked dye lasers, neither type of system is capable of producing a wide range of probing wavelengths in a single laser. This is in contrast to the broad picosecond continua which are easily generated in a solid state system.

Jain and Heritage (92) have demonstrated the feasibility of overcoming some of the tunability limitations by simultaneously mode-locking two different dye lasers with one argon ion pump laser with a cross correlation jitter between the two dye laser pulses of about 10 ps. Moreover, in the same paper, they reported a dual wavelength laser. By inserting a prism into the dye cavity, they achieved lasing at two wavelengths separated by 300 Å with a cross correlation function of 17 ps. Hesselink and Wiersma (93) have carried out a similar experiment synchronously mode-locking two different dyes, rhodamine 6G and rhodamine B. Although the above methods maintain the advantages of synchronously pumped lasers and the pulse widths are acceptable, the technique is limited to those combinations of dyes that can be pumped by the same

single mode-locked line of the pump laser. One could circumvent this constraint by broad band mode-locking of the pump laser, but this broadens the time duration of the dye pulse.

Another attempt to expand the range of wavelengths available to be used as probes was suggested by Ippen and Shank (94) and implemented by them (95) and by Gillbro and Sundstrom (96). The method is called the "read in-read out" technique and is illustrated in Figure 5. A synchronously pumped laser provides an initial picosecond pulse which is split into two pulses--one to excite the sample, and the second to be mixed with a third beam, the probe. The third beam provides the tunability. Wiesenfeld and Ippen (97) used a cavity-dumped, nanosecond dye pulse at 615 nm as the probe beam. To a process occurring on the picosecond time scale, the nanosecond pulse appears continuous and of constant intensity. The probe beam is directed through the excited sample and experiences some modulation (i.e., attenuation or transmission) dependent on the picosecond processes being investigated. This probe is then directed into a nonlinear crystal and mixed with the second picosecond pulse to yield an upconverted signal which is proportional to the intensity of the modulated probe and the constant intensity picosecond pulse. The time resolution is provided by scanning the picosecond mixer pulse through the modulated probe as one does in an autocorrelation experiment. Gillbro and Sundstrom (96) used a continuous polarized He/Ne beam as a probe. Assuming one can find a nonlinear crystal capable of frequency mixing the picosecond mixer and the probe wavelengths, any constant intensity wavelength source should be usable.

Figure 1-5. The "read-in, read-out" technique. The optical setup is shown in (a) representative time-intensity profiles of (b) the continuous or long pulse duration probe, (c) the time-variable picosecond excitation pulse and (d) the probe modulated (exaggerated for clarity) by a decaying transient

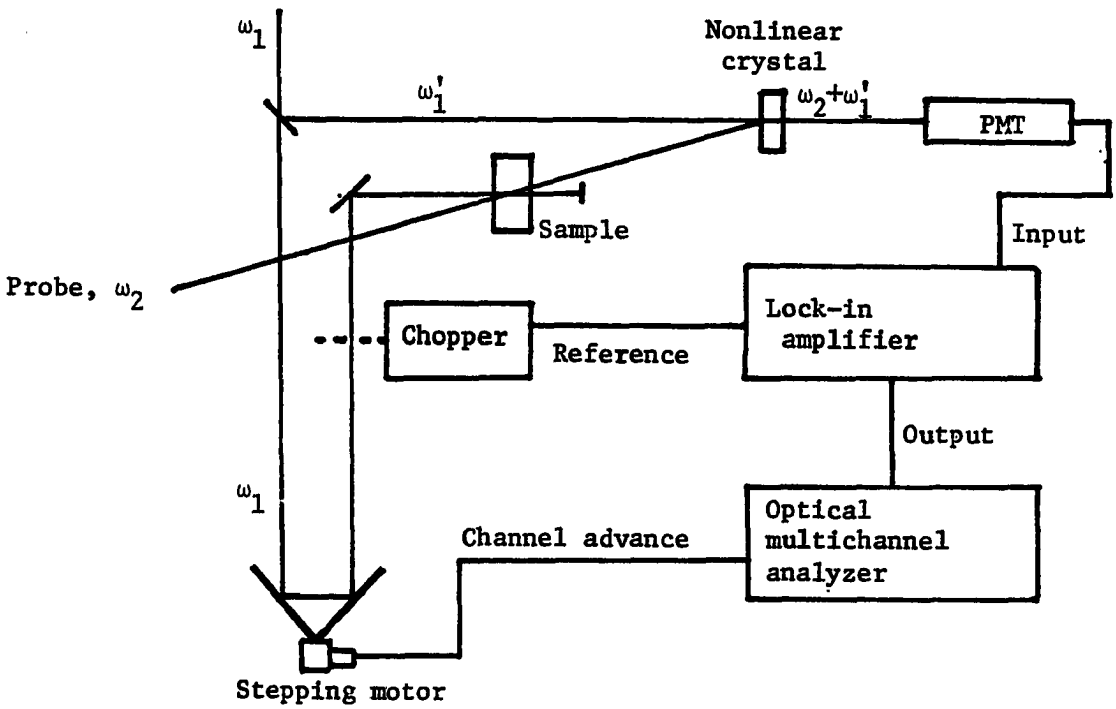

(a)

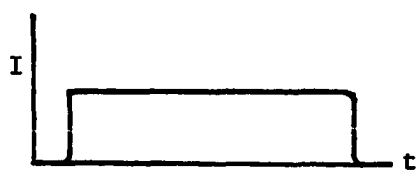

(b) probe pulse, ω_2, before entering sample

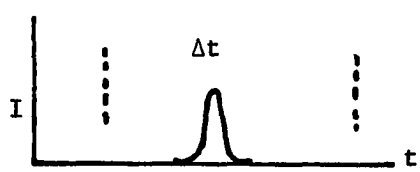

(c) time-variable picosecond excitation pulse, ω_1

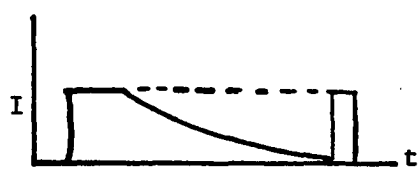

(d) probe pulse, ω_2, after exiting excited sample

Since the experiments based on the continuum generated by Nd:glass laser pulses have been so fruitful, it is not surprising that efforts have been made to amplify the weak dye laser pulses (~1 nanojoule) to levels sufficient to generate continua. This has been accomplished for both passively mode-locked (94) and synchronously pumped (98) dye lasers. A chain of three dye amplifiers pumped by a Q-switched Nd:YAG laser provided a 10^6 increase in dye laser pulse energy (94). The generated continuum is used in the same manner as previously described for solid state systems. The construction of a system using a Q-switched Nd:YAG to pump a chain of dye amplifiers is not a trivial exercise experimentally, and is extremely expensive.

Recent theoretical and experimental studies indicate that, at the present time, the above described system is the minimum necessary to amplify rhodamine 6G pulses to levels capable of generating continua (95). One of the drawbacks to this type of amplification is that the repetition rate of the dye pulses is reduced to the 10 Hz rate of the Q-switched Nd:YAG. Nevertheless, a number of research groups have implemented Nd:YAG pumped dye laser amplifiers (99, 100, 101). Waldeck et al. have amplified synchronously pumped dye pulses by a factor of 30 by pumping a dye amplifier with a cavity-dumped argon ion laser (91). They were able to frequency double their dye laser pulses while maintaining a repetition rate of 756.7 kHz, but these powers are still insufficient to generate broadband continua.

A new technique that seems to have significant potential for detecting extremely weak absorptions has been introduced by Bado et al.

(102, 103). A synchronously pumped laser has many sources of noise, originating in both the argon ion pump laser and in the dye cavity. Variations in the electrical discharge, plasma instabilities, noise in the acousto-optic modulator and mechanical noise in the resonator contribute to the noise level in the argon pump lasers. Temperature changes, dye-jet fluctuations, and other such variables also introduce noise into the dye laser. Heritage (104), Levine and Bethea (105, 106) have demonstrated that the noise levels in synchronously pumped lasers decrease by orders of magnitude in the megahertz range from the levels existing in the kHz range.

Taking advantage of this, Bado and coworkers used radio transmitters and antenna couplers to drive electro-optical modulators which modulated the pump and probe pulses at 14.25 MHz and 10.25 MHz, respectively. An additional 387 Hz modulation was impressed by a chopper onto the pump beam. A photodiode directly connected across the antenna input of a radio receiver tuned to the difference between the pump and probe frequencies, 4 MHz, was used as the detector system. The signal from the photodiode/receiver was fed into a lock-in amplifier referenced to the 387 Hz chopper frequency.

This apparatus had a noise level of 3×10^{-11} w in a 3.6×10^{-2} w beam (approximately shot noise limit). Furthermore, detection at the difference frequency discriminated against scattered light from both the pump and probe beams.

This system was utilized by Bado et al. (103) to study the effect

of solvents on the recombination dynamics of photodissociated I_2.

Summary

The principal aim of this chapter was to identify the chief concepts used in picosecond absorption spectroscopy and to note the primary experimental approaches used to obtain dynamical information on the picosecond time scale. The references cited are intended to be seminal or illustrative, but not exhaustive. Picosecond fluorescence spectroscopy, an area of growing importance because of advances in detection technology and data acquisition, has only been mentioned briefly. More extensive reviews of picosecond spectroscopy are available elsewhere (1, 2, 3, 76, 107, 108, 109, 110) and survey a much broader range of picosecond topics.

The outline for the rest of this dissertation is as follows. Chapter 2 will describe the experimental apparatus. Chapter 3 will discuss the generation and characteristics of the continuum, and Chapter 4, the application of the experimental apparatus to study the photodissociation dynamics of iodoanthracenes. Chapter 5 will provide a conclusion and summation of the technique and results.

CHAPTER 2

Introduction

This chapter describes the experimental apparatus used to perform the picosecond transient absorption experiments on the iodoanthracenes. The system consists of several parts: production, isolation, and characterization of the picosecond excitation and probe pulses; development and alignment of the beam steering and collection optics; calibration and synchronization of the data acquisition system; and computer manipulation of the data.

Principles of laser physics are not treated, because a substantial majority of the scientific community is familiar with lasers. Those readers desiring an introduction to the basic concepts of laser theory are encouraged to examine any one of several excellent texts on the subject (111-114).

Generation of Single Actinic Picosecond Pulses

In our laboratory, we used a neodymium:glass laser to generate trains of picosecond pulses. Such lasers have been used to perform substantial picosecond work in the past fifteen years.

When a trivalent neodymium cation is imbedded in an amorphous glass host, the spectral bandwidth is inhomogeneously broadened because each ion is in a slightly different crystal field environment. This broadening is on the order of 200 Å, in contrast to the 5 Å spectral bandwidth of crystalline neodymium:YAG media in which all the ions are in spatially identical sites. As mentioned in Chapter 1, a wide spectral bandwidth

is needed to generate extremely short duration pulses in accordance with the time-bandwidth product relationship.

In Figure 2-1, the relevant electronic energy levels and the prominent Nd:glass lasing transition are shown. The valence electronic structure of the lanthanide series is derived primarily from the 4f electrons. After excitation of the near IR absorption bands of the neodymium ion, the system rapidly populates the metastable $^4F_{3/2}$ level. Lasing can occur at 900 nm, 1.06 μm and 1.35 μm by transitions to $^4I_{9/2}$ (ground state), $^4I_{11/2}$, $^4I_{13/2}$, respectively. The 1.06 μm line is used almost exclusively.

Neodymium:glass is a four level laser. In this type of laser, the population inversion is maintained between the upper and terminal levels of the laser transition continuously throughout the duration of the pumping pulse by the rapid relaxation of the terminal laser level into a still lower electronic state. In the 1.06 μm transition, $^4I_{11/2}$, the terminal level, has a fast phonon-assisted transition to the ground state manifold $^4I_{9/2}$ (Figure 2-1).

ED2 type laser glass, manufactured by Owens-Illinois (115), was used as Nd^{3+} host. It is a lithium aluminum silicate glass doped to a concentration of 3% neodymium ions ($\sim 2.8 \times 10^{20}$ ions/cm^3). In addition to the spectral broadening properties, glass has several desirable characteristics that make it useful as a host. ED2 glass rods are easily fabricated in high purity, avoiding light absorbing impurities that plague crystalline structures; it can be polished to optical quality and drawn into large dimensions. The major disadvantage of ED2 glass is

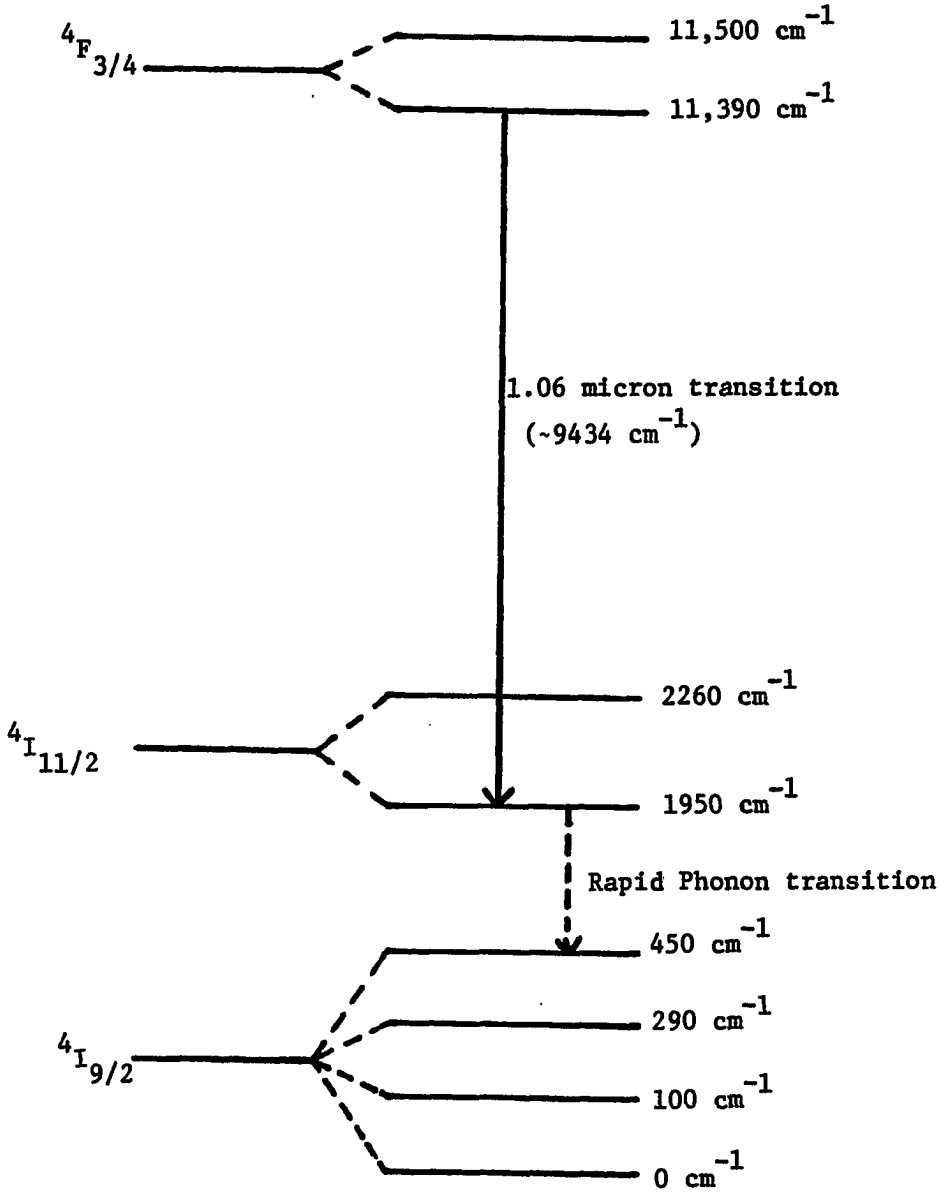

Figure 2-1. Relevant neodymium ion electronic energy levels for the neodymium-glass laser

its low thermal conductivity, 0.012 W $cm^{-1}K^{-1}$ at 300 K, and therefore it cannot dissipate heat rapidly. Thermal inhomogeneity has a pronounced deleterious effect on the operation of any laser. Thermally induced birefringence, thermal lensing and temperature dependent stretching and bending seriously degrade the optical quality of the cavity. Because of this detrimental property, even with water cooling, Nd:glass lasers seldom are fired more than once a minute. This low repetition rate complicates data acquisition because rigorous controls are required to operate a Nd:glass laser reproducibly and reliably over long periods of time (>4 hours). There is, therefore, strong motivation for designing experiments which acquire as much information as possible in a single shot.

The laser oscillator head and power supply were part of an Apollo Model 35 laser system. The laser head housed the Nd:glass rod, a 6" pumped length helical xenon flashlamp and its electrical connections, and provided a water-tight cylindrical rod was 9" x 5/8" diameter (22.9 cm x 1.6 cm diameter) and the ends were cut at Brewster's angle (57°16') and optically polished. Faces cut at Brewster's angle reduce reflection losses at the air/glass interface, thus eliminating the need for antireflection coatings which would be ablated by the high power densities produced by the Nd:glass laser. Furthermore, Brewster's angle polarizes the output of the laser in the plane of incidence by inducing reflection losses for the polarization that has its electric field vector perpendicular to the plane of incidence. The helical lamp configuration has larger pumping surface area and a longer arc length per linear

centimeter than a linear lamp, so that more power can be delivered to the rod per unit pumped length. Xenon is a commonly used gas in flashlamps becaue its conversion efficiency of electrical input to radiant output is 40-60% (116). A schematic diagram of the laser cavity is shown in Figure 2-2. The overall optical cavity length was 1.1 meters, delineated by a curved (R = 3m) 99.9% reflecting (@1.06 μm) end mirror and a flat 45% reflecting (@1.06 μm) output coupler. Both mirrors were mounted in precision mirror mounts (Oriel 1450) with a tuning angle range or ±8° about the vertical and ±4° about the horizontal to a resolution of 1 second. Within the cavity, a variable aperture restricted the lasing to low order TEM_{pq} modes.

The generation of picosecond pulses was accomplished by passively mode-locking the longitudinal modes of the laser. When the large number of longitudinal modes available in Nd:glass laser experience gain and begin to oscillate, each mode oscillates with its own phase. These modes will interfere constructively or destructively throughout the oscillator; modes which propagate through the cavity in a fixed phase relationship represent a significant electromagnetic flux density whereas those modes which destructively interact have small local electromagnetic flux density. The insertion of an intensity-dependent saturable absorber dye into the laser cavity allows the phase-locked modes to continue to oscillate and couple with other in-phase modes while discriminating against out-of-phase modes. The dye effects this selective modulation of the modes by absorbing the low intensity radiation which is generated by the out-of-phase modes and bleaching, due to saturation, when the

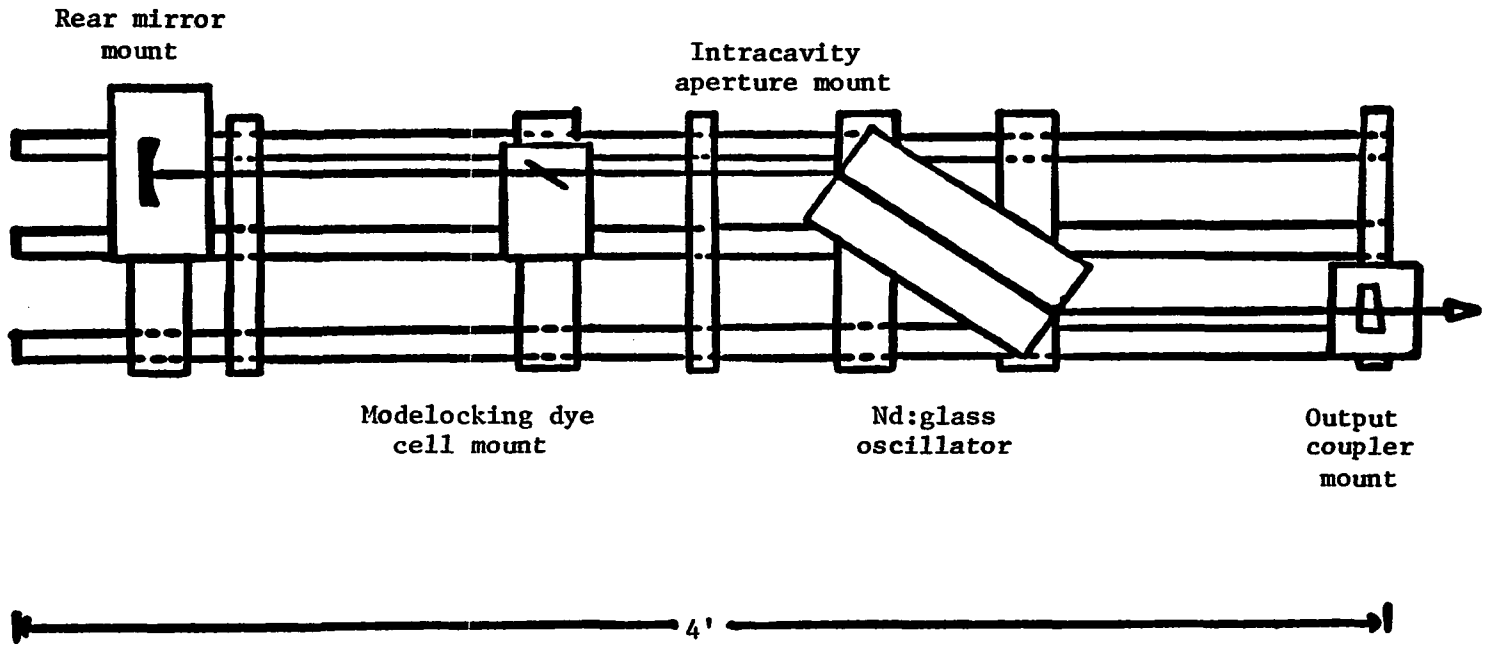

Figure 2-2. Schematic diagram of the neodymium-glass laser oscillator

intense in-phase modes pass through. The larger the number of modes propagating in-phase, the greater the intensity of the pulse and the less attenuation the pulse experiences. Moreover, a large number of longitudinal modes, which are spaced apart in frequency by c/2L where L is equal to the path length of the cavity (111-114), translates into a large bandwidth of frequencies present. According to Fourier transform theory, the bandwidth is inversely proportional to the duration of the pulse derived from the constructive interference of the member electromagnetic waves. In a modelocked Nd:glass laser, this bandwidth can be on the order of 100 cm^{-1}, implying the possibility of picosecond pulses. A further discussion on passive mode-locking is given in Appendix A. The dye we used was Kodak Q-switch dye #9860 which saturates at intensities of approximately 50 MW/cm^2 and has a recovery time of 9 ps (117). A reported problem associated with passive mode-locking is the cogeneration satellite pulses (118-119). These are lower intensity pulses that counterpropagate through the dye cell simultaneously with the main bleaching pulse. By using a 1 cm dye cell, meaning a transient time through the cell of 54 ps in dichloroethane (the dye solvent) and a dye with a short recovery time (~9 ps), the weak pulse propagates through a region of the cell where it encounters relaxed dye molecules and suffers attenuation (120). Our solutions of Kodak #9860 were dissolved in spectroquality dichloroethane and a fresh solution with a transmittance of 61% at 1.06 μm was mixed prior to each run. The dye cell was made of optical grade pyrex and had its optical surfaces parallel to within 5 minutes of each other (121). The

1 cm cell was oriented in the oscillator cavity at Brewster's angle (55°54') and covered with a light shield to retard degradation of the dye from UV light produced by the flashlamps and the ambient room light. The dye solution can also degrade by thermally induced decay but this is a minor contribution compared to the photochemically activated decay.

The mirror mounts, laser head, dye cell and cavity aperture were firmly mounted on a carbon steel/brass frame constructed to minimize cavity length variations and provide a stable platform for the optical elements.

An output pulse of the Nd:glass laser consists of a train of picosecond pulses separated by the roundtrip time of the cavity, 8 nanoseconds. For a number of reasons, it is often desirable to isolate only one of these picosecond pulses and amplify it rather than use the entire pulse train. Because of the nature of the modelocking which occurs in Nd:glass lasers, the pulse durations of generated picosecond pulses vary significantly within the train. Pulses generated late in the train are generally 2 or 3 times longer in duration than those produced in the earlier portion of the train, which are typically 6-8 ps fwhm (37, 122).

The principal cause of this broadening is self-phase modulation induced by the nonlinear interaction of the intense electric fields present in the laser cavity with the laser medium (123-126). Therefore, to work with the shortest pulses, one usually wants to extract one of the earlier pulses. Moreover, if the experiment involves molecules which exhibit photoreactivity or possess long-lived transient states,

successive excitation caused by a train of pulses can alter the photo-processes being studied.

The most common way to extract a pulse from a pulse train is to use an electro-optical shutter. The electro-optic shutter utilized in our laboratory employed a laser-triggered spark gap (LTSG) to provide a source of short duration high voltage pulses to activate a Pockels cell electro-optic modulator.

An electro-optic modulator is an uniaxial crystal that becomes birefringent when subjected to an electric field. When a pulse of light propagates through a properly oriented crystal, its polarization is not affected unless an external electric field has been impressed on the crystal. In that case, the polarization of the pulse is rotated to an extent which depends on the strength of electric field. If the electric field is switched on and off in a few nanoseconds, typically only one pulse in a train of pulses separated by 7-10 nanoseconds will be present in the activated crystal, and will have its polarization rotated. With the use of a polarizer, one can discriminate this pulse from the other pulses and isolate it.

The electro-optic modulator used was a Lasermetrics OEM-813 which employs a longitudally activated potassium dideuterium phosphate 2.54 cm (KD*P) crystal. Pockels cells using longitudinal activation apply the electric field parallel to the crystal's optic axis. When the electric field induces birefringence, the phase retardation of the light wave caused by propagation along an axis with two different indices or refraction can be expressed as

$$\delta = n_0^3 \, r_{63} \, V_z \, 2\pi \, \lambda^{-1} \quad , \qquad (2.1)$$

where δ is the number of wavelengths retarded in microns, n_0 is the ordinary index of retraction, r_{63} is the electro-optic constant for the specific crystal used, V_z is the voltage impressed along the optic axis (z axis), and λ is the wavelength of the propagating light. Note that the retardation is independent of length of the crystal and is linear in voltage.

KD*P has an electro-optic constant of 26.4×10^{-6} microns volt^{-1}; this is a factor of 2-3 larger than the constants of potassium dihydrogen phosphate (KDP) and ammonium dihydrogen phosphate (ADP), two other common electro-optic crystals. Because of this difference, KD*P can be operated at lower voltages than either KDP or ADP to induce a given plane retardation. Furthermore, KD*P absorbs less at 1.06 μm than the two other crystals, reducing the effects of heat on the optical properties of the crystal (127, 128). To change one linear polarization to the perpendicular polarization, a phase retardation of π is required, and the OEM813 requires approximately 9.5 kilovolts to provide this (129). To obtain the short duration high voltage pulses necessary to modulate the light, a laser-triggered spark gap was used (130-133). The overall pulse extraction technique is illustrated in Figure 2-3. The pulse train is first passed through a Glan-Thompson polarizer which horizontally polarizes the light. The train of pulses passes through the static Pockels cell into a second Glan-Thompson polarizer crossed with respect to the first one. All the horizontally polarized pulses are diverted

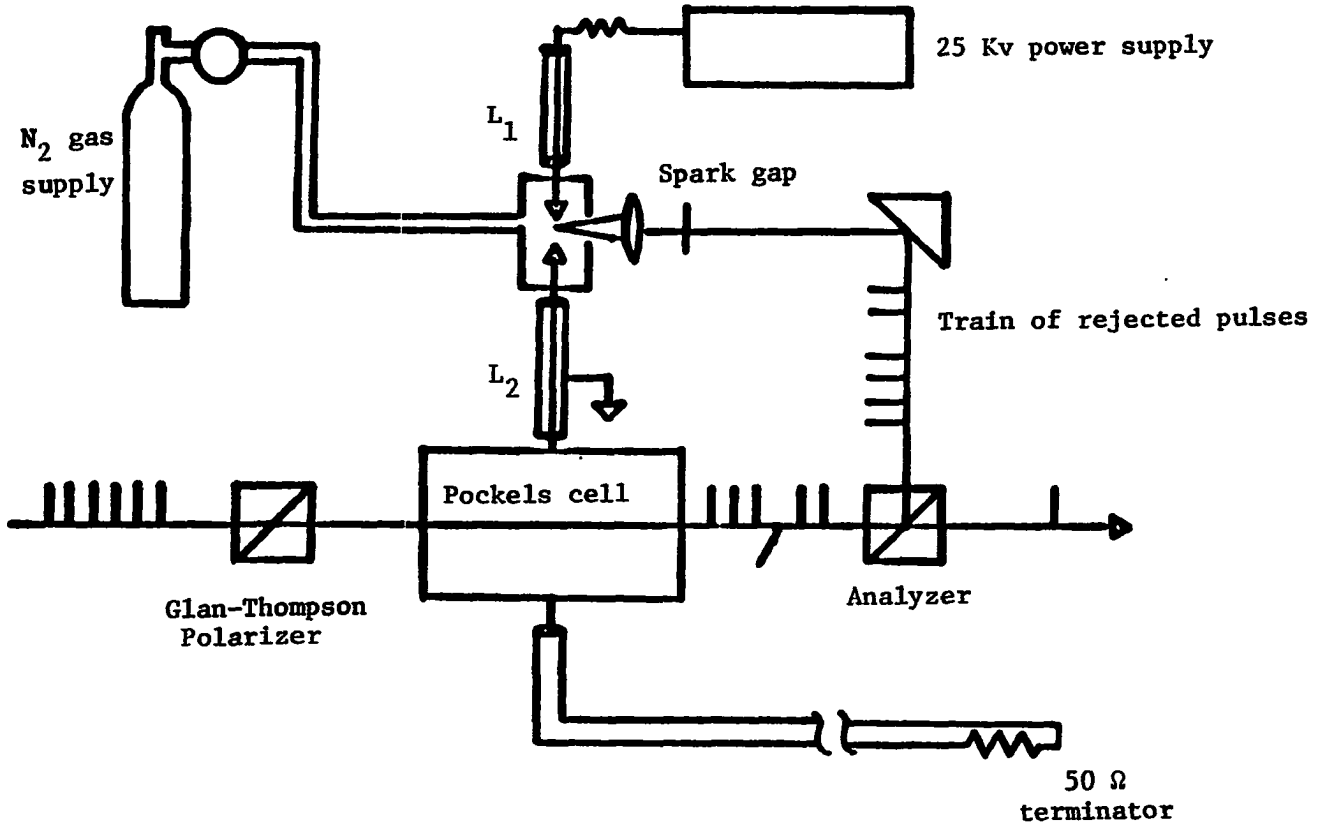

Figure 2-3. Pulse extraction apparatus employing laser-triggered spark gap and a Pockels cell

out of the beam path and focussed into the gap between the two electrodes of the spark gap. One of the electrodes is held at a variable potential of up to 25 kilovolts. The intense electric fields of the focussed laser pulses ionizes the nitrogen gas dielectric, causing it to break down and conduct. This results in the propagation of a voltage pulse one-half of the positive electrode potential through the coaxial cable labelled L_2 in Figure 2-3. The length of cable L_1 determines the time duration of the pulse and the length of cable L_2 determines the time interval between breakdown of the spark gap and application of the voltage pulse to the Pockel cell (120, 128). The RG214/U cables in our system were cut to produce a 3 ns high voltage pulse at the shutter at approximately 6 nanoseconds after breakdown of the spark gap. The breakdown of the dielectric gas is controlled by 3 factors: the pressure of the N_2 gas, the intensity of the laser pulses, and the voltage potential across the gap. The pressure of the N_2 atmosphere was approximately constant at 3.5 atmospheres; the voltage across the gap was controlled by variable transformer. During the initial setup portion of a run and, if necessary, during the experiment, the voltage across the gap was empirically adjusted so that dielectric breakdown occurred and extraction was accomplished within the first third of the pulse train. If varying the voltage didn't produce satisfactory results, one could vary the intensity of the ionizing laser pulses by optical density filters. The whole process of generating and propagating the high voltage pulse into a Pockels cell generates a significant amount of electromagnetic noise, especially in the microwave region. Since the duration of the

source electromagnetic wave is on the order of nanoseconds. This noise is detrimental to reliable operation of several of the data acquisition instruments in our laboratory, specifically the microcomputer and vidicon detection system. To mute this noise, both the spark gap and the Pockels cell were surrounded by plexiglas-copper mesh Faraday cages.

To monitor the modelocking and the position in the pulse train from which the extraction had taken place, a small amount of the rejected pulse train was deflected into a light shielded ITT F4502 biplanar phototube. The photocathode of this tube was made from cesium-silver oxide, giving it S1 spectral response (Electronics Industries Association Standards). This type of photocathode has a maximum sensitivity at 800 nm, but has sufficient sensitivity to allow detection of near infrared signals out to 1.1 microns. A Fluke high voltage power supply provided +2000 volts to the phototube anode, and the coaxial output was directed into a Tektronix 7704A oscilloscope equipped with 7A26 dual trace amplifier and 7B92A dual time base plug-in units.

After a picosecond pulse had been successfully extracted from the train, it was amplified by a factor of 80-100 by two Nd:glass amplifiers. The first amplifier offered approximately 15 cm of pumped gain and was part of the Apollo Model 35 laser system; the second amplifier provided 20 cm of pumped gain and was powered by a Holobeam 10 kv power supply. Both amplifiers employed helical flashlamps, water cooling and ED2 laser glass rods. The voltages applied to either amplifier lamp could be varied from 0-10 kV, and both amplifiers could be fired independently.

Synchronization of the flashlamp firing to obtain maximum gain was controlled by the vidicon Biomation interface electronics (vide infra).

To shift the infrared wavelength into the visible or ultraviolet region where the majority of reactions of photochemical interest occur, second harmonic, third harmonic, and continuum generation were used. These processes depend on the nonlinear properties of the medium in which they occur. Because of the crucial role of the continuum in these experiments, its generation and characteristics will be treated in Chapter 3. A qualitative treatment of optical harmonic generation is given in Appendix B, and detailed treatments can be found in a number of references (113, 134, 135).

After amplification, the 1.06 micron pulse was frequency doubled and tripled by angle index matched 2.54 cm KD*P crystals to generate picosecond pulses of 532 nm and 354 nm.

In Figure 2-4, the overall experimental setup is shown for the generation of ultrashort pulses in the visible and ultraviolet. This arrangement is typical for Nd:glass systems, whether one is doing fluorescence or absorption studies; the rest of the apparatus discussed is specific to picosecond transient absorption experiments. After the pulses were generated, they were characterized to estimate energy content and time duration.

Characterization of the Picosecond Pulses

The energy in a picosecond pulse produced by a Nd:glass laser can vary significantly from pulse to pulse in marked contrast to the relatively stable and consistent pulse energies one obtains from

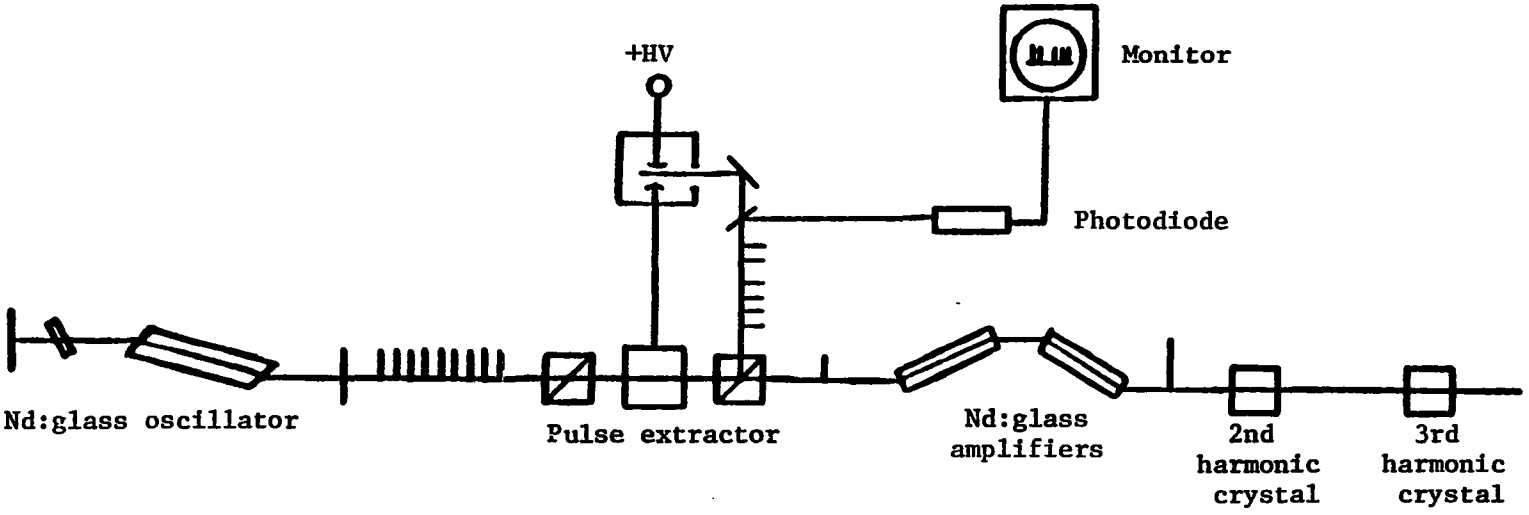

Figure 2-4. Generation of a single picosecond pulse

synchronously-pumped dye lasers. Variable factors such as pumping energy of the lamps in both the oscillator and amplifiers, position of the pulse at time of extraction, quality of the extraction, conversion efficiency of the harmonic generation processes, and the inherent randomness of the pulse evolution within the oscillator all contribute to this lack of pulse reproducibility. In every experiment, to compensate for this variation among the pulses, each laser pulse used to obtain data had a small portion of its energy reflected into a monitor photodiode. The photodiode was a Hewlett Packard HP4220 PIN photodiode. The spectral responsitivity of the diode was increased by removing the window glass plate, allowing detection into the U.V. Furthermore, the diode was mounted in a reverse biased configuration to increase its risetime response (~1 ns) and a diffuser was used to uniformly illuminate the active area of the diode with the incident light. The generated signal was stored in a Biomation 805 transient recorder and monitored on a Tektronix 555 scope. Each optical density transient datum point was normalized to this captured intensity signal before being used to interpret the results of an experiment.

Pulse energies were measured using a Hadron 100 Ballistic thermopile and a Kiethley model 177 Digital Voltmeter. The entire pulse or whole pulse train was directed into the aperture of the thermopile. A single IR picosecond pulse after amplification contained about 80-100 millijoules of energy. Single pulse energies of the second harmonic at 532 nm were on the order of 9-11 millijoules.

There are several methods to measure the duration of picosecond

phenomena (76, 121, 136). Because to the time scale involved, the only type of electronic device that possesses the time resolution necessary to measure picosecond pulses is a streak camera (137, 138). These devices, which are constructed in several different designs, transduce an incident light pulse via a photocathode into a burst of photoelectrons which are accelerated through a potential field and are streaked across the surface of a detector by a carefully calibrated high voltage ramp. From the length of the image on the detector and a knowledge of certain crucial parameters such as the photoelectron spread with transit time and the spatial and temporal properties of the potential fields inside the camera, one can establish the duration of the incident light pulse. Although these cameras have achieved a time resolution of less than 2 picoseconds, reliable and accurate streak cameras are extremely expensive.

Optical techniques, used since the early experiments of picosecond spectroscopy, still enjoy considerable use among picosecond spectroscopists to ascertain pulse durations and to synchronize the occurrence of two picosecond pulses at the same spatial point (76, 136). Besides being inexpensive, many of the optical techniques have a time resolution governed by the duration of the shortest optical pulse used and therefore can be used to measure femtosecond durations. A typical approach to measuring a pulsewidth is to utilize an autocorrelation technique. In an arrangement similar in concept to a Michelson interferometer, the pulse to be measured is split into two pulses by a beamsplitter; one of the pulses is sent through a variable optical path which introduces a

time differential between it and the other pulse and is then recombined with the other pulse in an optically nonlinear media. The nonlinear media exhibit an intensity-dependent effect such as second harmonic generation, two-photon fluorescence or three-photon fluorescence that is significantly (how significantly depends on the specific nonlinear phenomena) enhanced when two radiation fields are present simultaneously over that exhibited when either one of the two pulses are in the media alone. Technques involving autocorrelation measurements have been treated in detail by Ippen and Shank (136).

Another similar correlation technique using an optical Kerr shutter was introduced by Duguay and Hansen (139) and was used in our experiment to estimate the durations of our pulses and to establish the optical path lengths of the pump and probe pulse necessary so that both pulses simultaneously arrived at the sample cell. After those paths had been established, we could vary the optical path length of one of the pulses so that the probe pulse interrogated the sample at a reproducible known time after excitation.

The Kerr effect, or quadratic electro-optic effect, is the manifestation or birefringence in a substance when it is subjected to an external electric field. First discovered by John Kerr in 1875 (140), the effect has been generally accomplished by a DC electric field; however, Buckingham in 1956 (141) predicted that the Kerr phenomena could be produced by the oscillating electric field of a polarized light wave, and this was experimentally verified by Mayer and Gires in 1964 (142). Ordinarily, a dielectric material will have only one index of refraction

for any given wavelength of light, and this index is independent of polarization or propagation direction. However, when a sufficiently intense external electric field, AC or DC, is impressed on some materials, several mechanisms within the media can induce a state of time-dependent birefringence. Molecular reorientation, molecular libration, electron cloud distortion and molecular redistribution have been cited as origins of the phenomenon (138, 143-146). With the exception of molecular reorientation, the response and decay times of these mechanisms, although different, are generally faster than the duration of a picosecond pulse, especially in liquid or gaseous media.

The induced birefringence behaves optically as though it were an uniaxial crystal, usually a positive uniaxial crystal, with its optic axis aligned in the direction of the electric field. This birefringence results in two polarization-dependent indices of refraction--one, n_{11}, for light with its polarization aligned parallel with the induced optic axis; the second, $n_{\perp}$, for light with its polarization orthogonal to the optic axis. After initial experiments by Mayer and Gires, Duguay and Hansen used the intense electric fields of picosecond Nd:glass pulses to induce the optical Kerr effect in two common Kerr liquids, CS_2 and nitrobenzene, to develop an ultra-fast optical shutter to gate picosecond phenomena into a detector (139). A diagram of an optical Kerr shutter is shown in Figure 2-5. In this ultrafast shutter, an intense horizontally polarized 1.06 μm picosecond pulse acted as trigger pulse which induced the liquid in the cell to become birefringent; its optic axis aligned horizontally with the trigger pulse.

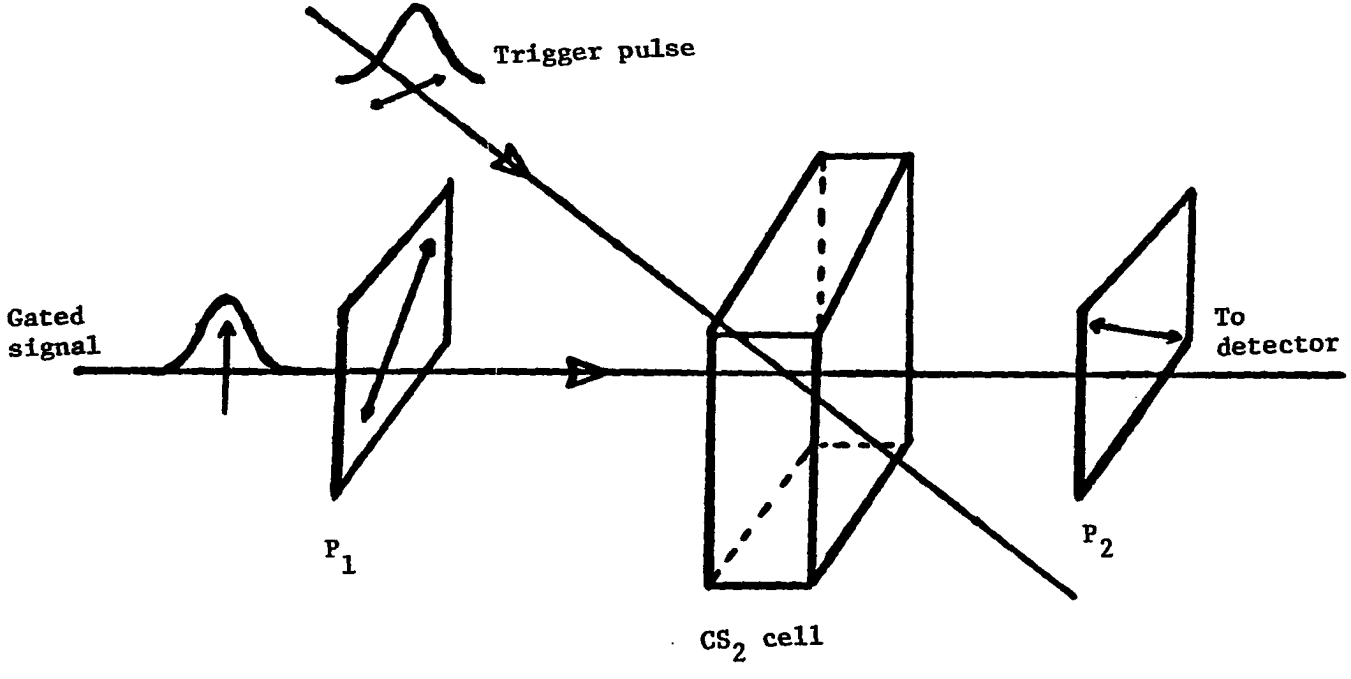

Figure 2-5. Carbon disulfide optical Kerr cell

The signal that was to be gated through the shutter first passed through a polarizer (P_1, Figure 2-5) with its axis positioned at 45° to the horizontal. If the Kerr shutter was birefringent when the polarized signal passed through, the signal experienced a phase retardation, or change in polarization. However, if the cell was nonbirefringent due to arrival of the signal at the cell before the trigger pulse had activated the Kerr effect or if the time-dependent birefringence had decayed, the signal passed through with its polarization unchanged. A final polarizer, P_2, was oriented with its axis orthogonal to the initial polarizer P_1 and positioned in front of a detector. Signal light that underwent a change in polarization from the initial state created by P_1 passed through P_2 and a signal was detected in proportion to the birefringence it experienced; but signal light that experienced no change in polarization was extinguished by P_2 and no signal light was recorded. Obviously, if the shutter can be opened or made birefringent for only a few picoseconds and can be varied over the duration of a signal pulse, one can gate selected portions of the signal. This, in fact, has been done to measure the passage of a picosecond 532 nm pulse through the Kerr cell (139) and to gate picosecond fluorescence signals (147-151). The "open" time of the optical Kerr cell or the period in which the cell is birefringent is a function of the duration of the trigger pulse, the mechanisms responsible for the birefringence, geometrical considerations of the cell, group velocity dispersion between the trigger and signal wavelengths, and the medium used. The time-dependent birefringence induced by the trigger pulse can be expressed as

$$\delta n_{11} - \delta n_1 = \frac{\eta_{2B}}{\tau} \int_{-\infty}^{t} \overline{E^2(t')} \exp[(t'-t)/\tau] dt' \quad , \quad (2.2)$$

where η_{2B} in the nonlinear Kerr index (2×10^{-11} cm^2 V^{-2}, (152)), $\overline{E^2(t')}$ is the squared optical field averaged over one optical cycle, t and t' are time variables, τ is the birefringent relaxation time for the medium (125, 153). In Kerr cell shutter applications for nanosecond and longer times, nitrobenzene has been extensively used because it has a substantial nonlinear Kerr index (2.5×10^{-11} esu (152)); however, the molecular reorientation decay time is ~32 ps (139) which significantly extends the lifetime of the induced birefringence and degrades the picosecond time resolution of the shutter. A better molecule is carbon disulfide, CS_2, which has a slightly lower nonlinear Kerr index (2×10^{-11} esu) but a molecular reorientation time of 2 ps (139, 143, 154). The other mechanisms that contribute to the induced birefringence (vide supra) have relaxation times in liquids in the femtosecond regime and follow the time profile of the trigger pulse; therefore, in liquids, usually only the molecular reorientation time will substantially contribute to the persistence of the induced birefringence and the magnitude of that contribution depends on the molecule used.

In the case when CS_2 is used as the Kerr medium, the 2 ps response time of the CS_2 adds a negligible contribution to the "open" time if the trigger pulses are on the order of 8-10 ps (152, 153, 155), the typical duration of Nd:glass lasers. If one neglects the 2 ps response time, equation 2.2 can be expressed:

$$\delta n_{11} - \delta n_{1} = \eta_{2B} \overline{E^2(t)} \qquad (2.3)$$

which is the expression one obtains for the quadratic electro-optic effect (136). Another factor that contributes to the "open" time of the Kerr shutter is the group velocity dispersion (155, 156). This contribution becomes more pronounced as the optical path length through the cell increases. Topp and Rentzepis (157), using Nd:glass laser pulses, found only a slight broadening in a 1 cm CS_2 Kerr cell due to group velocity dispersion between 1.06 μm and 532 nm pulses; however, in longer cells, the dispersion contribution significantly broadened the open time of the shutter.

Struve (155) extended the discussion on the effects of group velocity dispersion and beam geometry and demonstrated, under certain conditions, one can achieve maximum time resolution even for long cells. Other factors such as concentration and temperature effects on the nonlinear Kerr index have been discussed by Ho and Alfano (152).

To minimize the effect of dispersion, one might be tempted to go to very short optical pathlengths; unfortunately, the shorter path reduces the magnitude of the birefringence induced in the signal which, consequently, reduces the amount of signal transmitted. As a compromise between dispersion broadening and intensity of signal transmitted, we used a CS_2 shutter with a 1 cm pathlength. Under these conditions, one could expect that the "open" time of the CS_2 shutter would follow the time profile of the trigger pulse if it is on the order of $\gtrsim$7-12 ps (152).

As mentioned earlier, establishing the zero time or coincident arrival of both the pump and probe pulses at the sample cell is crucial to being able to reproducibly delay the probe continuum with respect to excitation. To find the zero time path lengths using an optical Kerr shutter, we set up the optics in the configuration that would be used to do the actual pump probe optical density transient experiments (Figures 2-6 and 2-8) with the addition of the polarizers and Kerr cell. The CS_2 Kerr cell was positioned, stain-free to avoid stress birefringence, in the holder that the sample would occupy during an experiment; the 1.06 μm trigger pulse followed the path that the 354 nm excitation pulse would follow in a transient absorption experiment and the 532 nm pulse, the signal pulse in this arrangement, traced the identical trajectory that the continuum probe would follow. The same detector was used for both the establishment of the timing and the pump and probe experiments. The optical path of the trigger pulses included a variable optical delay line that consisted of two mirrors joined orthogonal to each other and mounted on a micrometer-driven translation stage capable of 2 inches of translation. Since the optical layout allowed the pulse to transverse the variable delay line twice (Figure 2-6), the total variation in time was $(2)(5cm)(3 \times 10^{10}\ cm\ s^{-1}) \approx 340$ picoseconds. Filters (F_1, F_2) were used to attenuate the pulses and to remove residual radiation. A series of shots was taken at various delays and the transmission through the Kerr cell monitored. Figure 2-7 shows the transmission of the 532 nm pulse through the cell as a function of delay. The micrometer setting which corresponded to the maximum

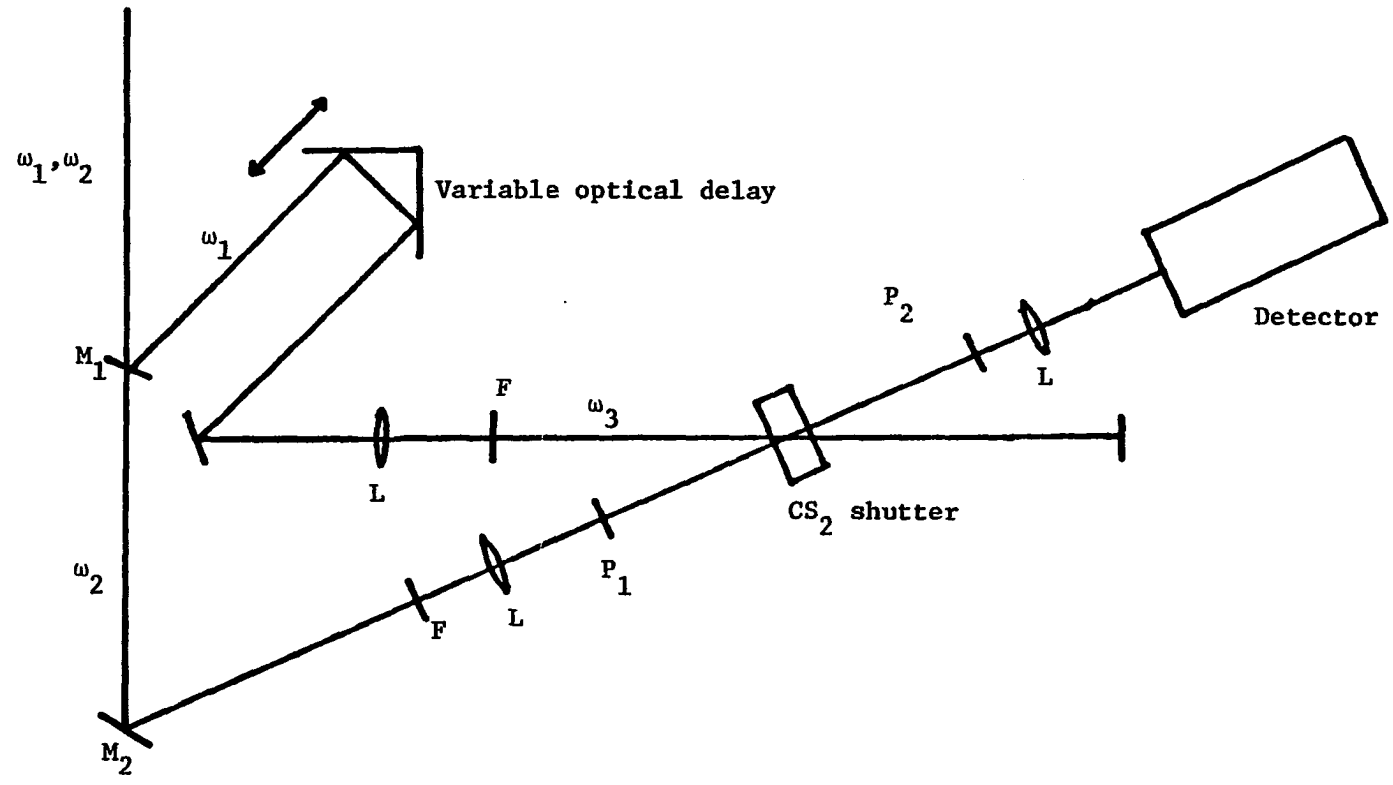

Figure 2-6. Optical setup to establish equal optical path lengths for simultaneous arrival at the sample cell by the pump and probe pulses. L = lens, F = filters, M_1 = dichroic reflector, M_2 = mirror, P_1 and P_2 are crossed polarizers, ω_1 = 1.06 μm, and ω_2 = 532 nm

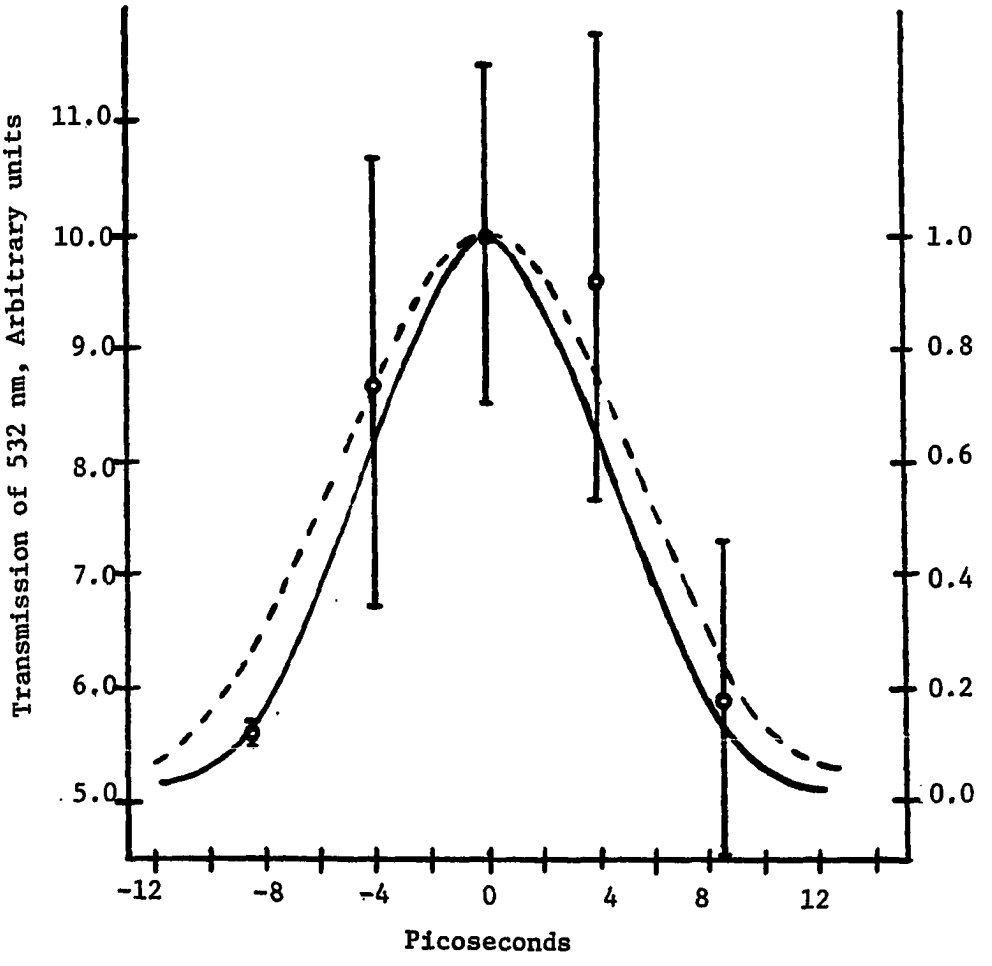

Figure 2-7. Experimental data for transmission of the 532 nm signal pulse through the CS_2 Kerr cell. The solid curve is the predicted transmission through the cell for a 8 ps fwhm 1.06 μm trigger pulse and a 6 ps fwhm 532 nm pulse if both are assumed to be Gaussian. The dashed curve is the predicted transmission for a 10 ps fwhm 1.06 μm Gaussian trigger pulse and 7 ps fwhm 532 nm Gaussian signal pulse

transmission of 532 nm was used as the zero time position since the maximum transmission in a picosecond Kerr cell will occur when both the signal and trigger pulses are in the cell simultaneously.

To estimate the pulse widths of the trigger pulse and signal pulse, a simple convolution of two Gaussian functions was performed. Two cases which bracket the experimental points are shown in Figure 2-7: case 1, in which the trigger at 1.06 μm had a pulsewidth of 10 ps fwhm and the 532 nm signal pulse had a 7 ps fwhm; case 2, in which the 1.06 μm had a width of 8 ps fwhm and the 532 nm had a width of 6 ps fwhm. The full width half maximum of the experimentally derived function above background is approximately 10 ps; the fwhm for the convolution curves of case 1 and 2 is 12 ps and 10 ps, respectively. The pulsewidths used in either case are typical of those commonly generated by Nd:glass pulses. The zero time varies for different wavelengths due to time dispersion caused by the optical elements in the system, especially the 20 cm continuum cell. For the transient absorption experiments, the zero time was specified for the wavelength of maximum absorption (see Chapter 4).

Optical Layout

After the second and third harmonics had been generated, the pulses were directed into the optical setup shown in Figure 2-8. Prior to optical harmonic generation, the amplified 1.06 μm pulses were filtered by a Schott RG780 filter (F_1), removing the background radiation from the flashlamps. After frequency doubling and tripling, a dichroic mirror M_1

Figure 2-8. Optical arrangement for transient absorption experiment. SHG = second harmonic crystal, THG = third harmonic crystal, C = CCl_4 continuum cell, and B.S. = beam splitter. The side view depicts the creation of the I and I_0 beams which are co-linear and lie in the vertical plane of the apparatus. See text for further discussion

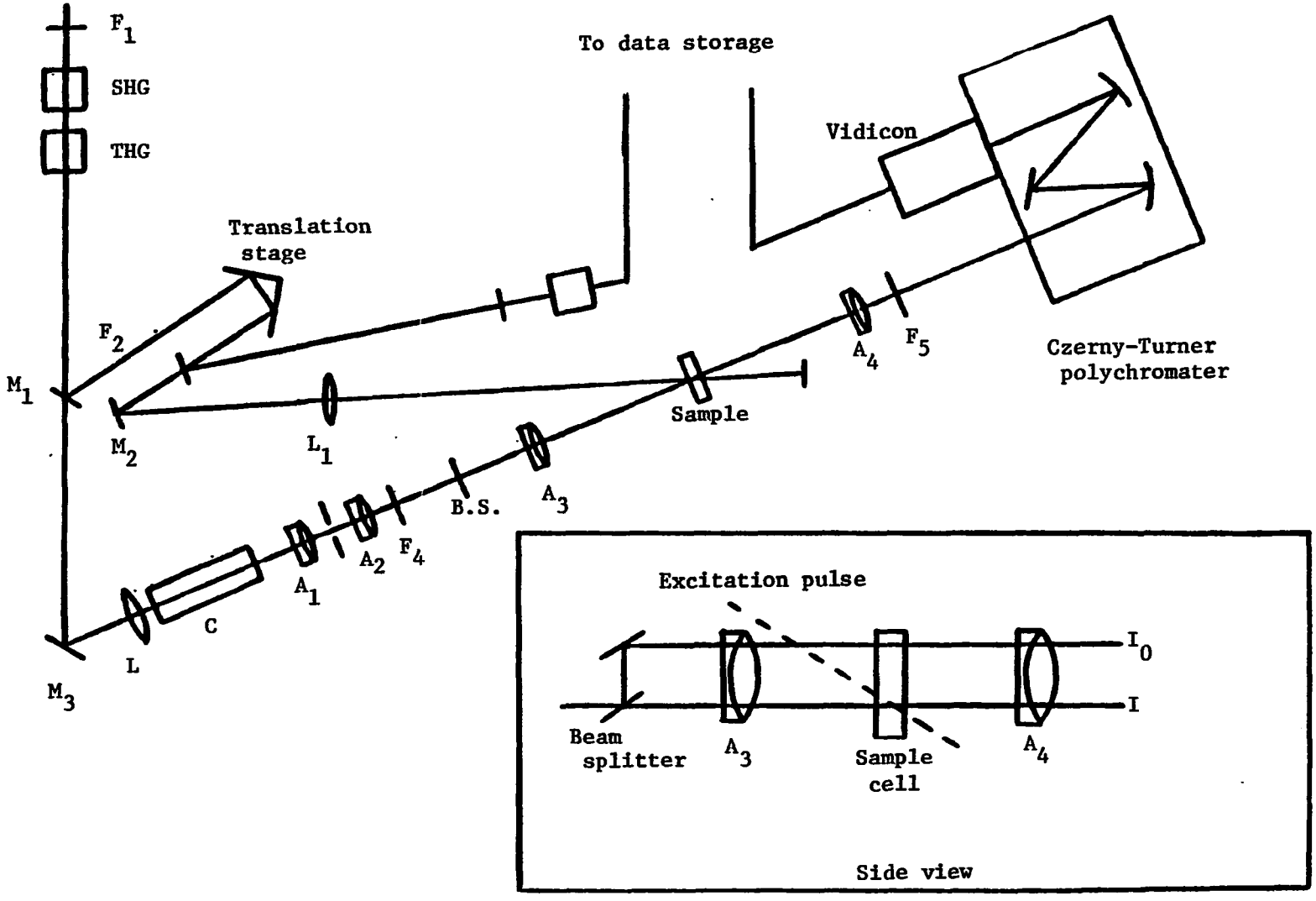
F1
SHG
THG
To data storage
Vidicon
Translation stage
F2
M1
M2
L1
Sample
A4
F5
Czerny-Turner polychromater
B.S.
A3
A2
F4
A1
C
L
M3
Excitation pulse
I0
I
Beam splitter
A3
Sample cell
A4
Side view

selectively passed 532 nm and reflected 1.06 μm and 354 nm. Undesired 1.06 μm radiation was filtered by two 3 mm thick Corning 7-51 filters (F_2) from the 354 nm pulse. In cases when 1.06 μm pulses were needed, such as establishing the timing or estimating the pulse width estimation, the third harmonic crystal was detuned. The 354 nm light was passed through the variable delay and directed by mirror M_2 into the sample cell. A 15 cm focal length lens (L_1) focussed the excitation pulse into the sample. The lens, which was mounted on a translation stage, and the mirror, which allowed arbitrary horizontal and vertical positioning of beam at the sample cell surface, permitted one to optimize the excitation beam overlap with the probe beam. The excitation beam diameter was approximately 3 mm in diameter at the surface of the sample cell. A small portion (≤4%) of the third harmonic was deflected into a HP4220 pin photodiode for normalization of the laser shot. A Hoya U330 filter (F_3) was used to screen any extraneous light from the monitor. Aside from normalization of excitation pulse intensities, monitoring the third harmonic allows one to obtain a qualitative judgment on how the various components of the pulse generation-pulse extraction, amplification, SHG- are behaving. Well-formed, short duration fundamental pulses extracted from the early part of the train yield intensities for the third harmonic that are fairly reproducible from shot to shot (±10%).

The 532 nm pulse is used to generate the white light continuum that is used as a probe of the transient excited state. The generation of the continuum can involve a number of nonlinear processes-four-wave

mixing, stimulated Raman scattering, self-phase modulation and parametric processes--which depend on such factors as power density of the initiating beam, time duration of the pulse, length of the cell and nature of the continuum medium. The effects of these nonlinear processes on the spectral content and behavior of the continuum is treated in Chapter 3. Phosphoric acid (H_3PO_4), carbon tetrachloride (CCl_4) and 1-octanol ($C_8H_{17}O$) were tested as continuum sources; carbon tetrachloride exhibited the strongest continuum in the region of interest, 400 nm-500 nm, and was used in the experiment.

The 532 nm light was focussed approximately 1 cm behind the incident surface of the continuum cell (c in Figure 2-8). Depending on the experiment, the continuum cell was 5 or 20 cm long. After the continuum was generated, all the lenses used in the probe's optical path were achromats to minimize the focussing errors due to chromatic aberrations. The continuum was gathered, spatially modulated, and collimated immediately after passing through the continuum cell by two 15 cm focal length achromats separated by an iris (A_1, A_2). Residual 532 nm and stokes continuum were attenuated by a Corning 1-64 filter (F_4). The continuum was split into a probe beam (I) and a reference beam (I_0) by a linearly variable optical density slide coated with an inconel surface. Both beams were then passed symmetrically through a 27 cm focal length achromat (A_3) which focussed the beams down to a diameter ~1 mm on the front surface of the sample cell separated by approximately 3-4 mm. After passage through the sample cell, both beams were focussed by a final achromat (A_4) into the slit or the Czerny-Turner polychromater

and vidicon detection system. The sample cell had a 2 mm optical path length, and the optical density of the sample solution at the excitation wavelength was 1.7-2.0.

Detection Apparatus and Data Acquisition

The 30 cm focal length Czerny-Turner polychromator was equipped with a 300 lines/mm grating which horizontally dispersed the two continuum signals across the exit slit. The resolution of the polychromator was 2 nm and the linear dispersion was 7.9 nm mm^{-1}.

The detector system we used was similar in principle to an optical multichannel analyzer. One of the requirements for the detector in these experiments was that the device had to be able to record the spatially dispersed spectral information of the two signal beams, I and I_0, and store that information until the data handling system was able to retrieve it. Photographic techniques are able to do this and have been used in the past (32, 48). Despite the low cost and high resolution, photographic techniques require accurate calibration for reliable light intensity measurements, have a long access time before one can view the data, and respond in a nonlinear fashion to incident light. There are a number of electronic devices that have the capability to perform multichannel analyses and these have been reviewed by Talmi (158). One such detector is a silicon diode array vidicon which was utilized in our experiments. The silicon diode array has several desirable characteristics which qualify it for use in low light level transient absorption experiments: the spectral response of the diode array extends throughout

the ultraviolet, visible and near IR; it has a sensitivity comparable to ASA 3000 film (energy density required to cause an image for silver halide film is $\sim 5 \times 10^{-3}$ ergs cm^{-2} compared to 1×10^{-4} ergs cm^{-2} for a Si vidicon (159)) (160); due to its electronic nature, the image stored on the array can be accessed rapidly and is easily converted into digital information; and it is extremely resistant to damage by exposure to intense light (161, 162). The Si vidicon array has a gamma of unity implying a linear output to the intensity of input signal; however, vidicon nonlinearity and saturation effects do become important when exposed to intense light (26, 27). Throughout the transient absorption experiments, the recorded signals fell well within the linear range.

We used a RCA 4532A vidicon tube which has an active array area of 115 mm^2 (12.8 mm x 9.6 mm) with a density of approximately 620,000 diodes cm^{-2}. Each silicon diode is a reverse-biased pn junction and is separated from adjacent diodes by ~8 microns. The discrete nature of the diode array can cause moire effects in the infrared, but are negligible in the visible region where the detector was used (163). Blooming or cross talk among the diodes induced by intense light limits the dynamic range to approximately 1000 (158).

Figure 2-9 shows schematically the detection process that occurs within the reverse-biased diode. The p-doped region acts as an island storing the electrons deposited by a scanning electron gun which rasters the surface exposed to it. When an incident photon impinges on the diode, it generates charge carriers. Holes (vacancies in the lattice that can accommodate electrons) migrate through the depletion layer to

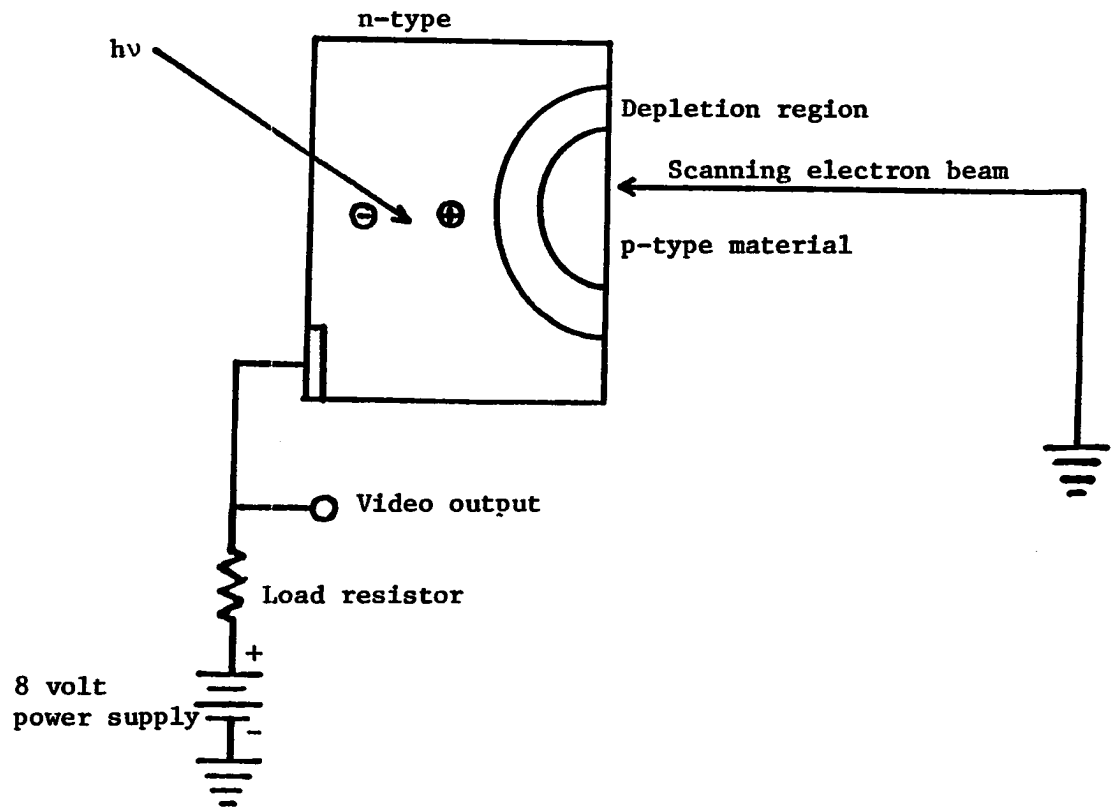

Figure 2-9. Schematic of a typical silicon photodiode used in the array of diode in a S_1-diode vidicon

the p region, where they combine with free electrons, depleting the negative charge there. The number of holes generated, and hence the magnitude of charge depletion, is proportional to the number of incident photons. The depletion region acts as a capacitor, storing the image charge in the p region, until the electron beam rescans and replenishes the depleted charge. When the electron beam contacts the depleted diode, the circuit is closed and current flows through the load resistor generating an output video signal.

The Si vidicon tube is housed in a Cohu 4350 closed-circuit television camera assembly, and the video output is generated in the same manner as in a conventional television system. The electron beam's raster pattern is controlled by the simultaneous manipulation of both the horizontal and vertical deflection circuits. Figure 2-10 depicts the general concept of odd line interlaced scanning of the type used in this experiment as well as in the U.S. commercial television industry (EIA RS-170 (164)). The horizontal deflection sawtooth waveform is a 15.75 KHz signal; the vertical deflection sawtooth waveform is a 60 Hz signal tied to the power supply voltage, which is also the standard 60 Hz line frequency. One complete raster of the array surface consists of 525 horizontal scans or lines divided into two fields--an odd field and an even one--ideally consisting of 262.5 lines each. Each horizontal sweep takes $(15.75\ \text{KHz})^{-1}$ or approximately 63.5 μs to complete: 10 μs of which is allotted to returning the electron beam to the starting side of the scan (left side of Figure 2-10), during which time the video signal is blanked out by a horizontal blanking pulse with a

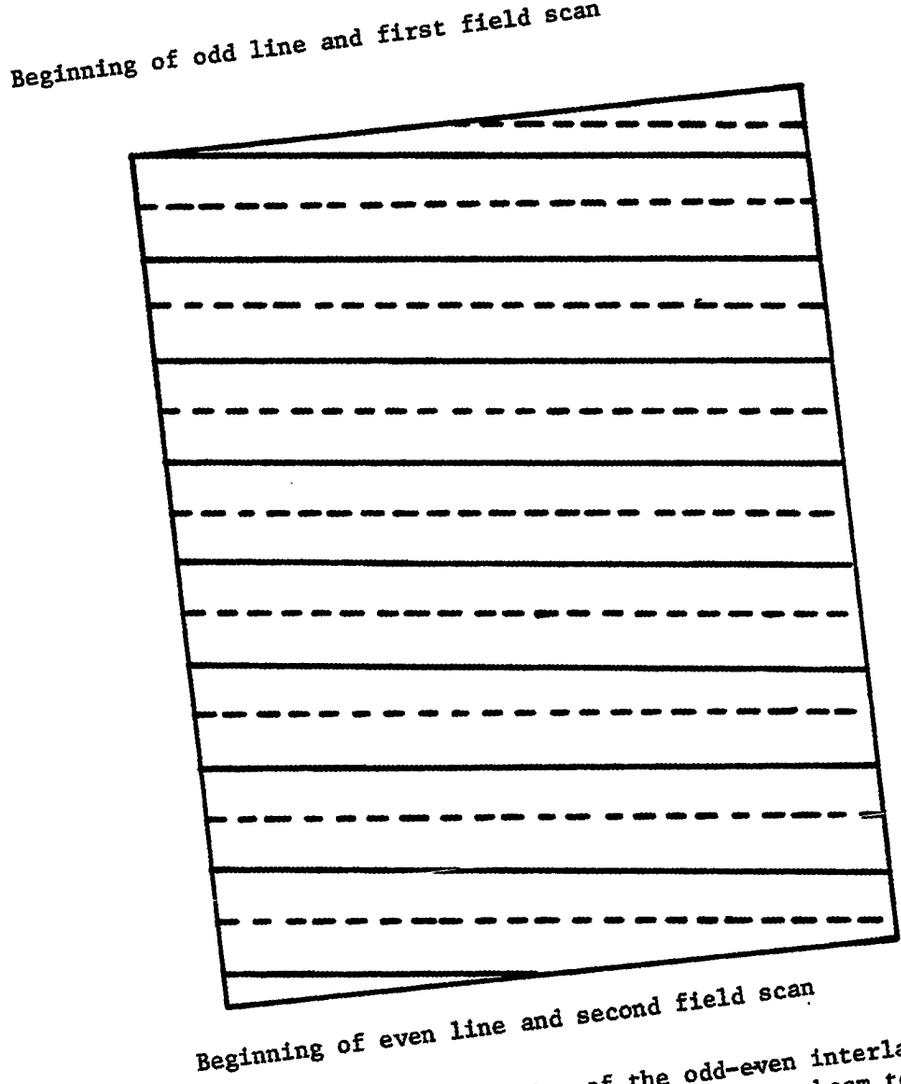

Figure 2-10. Simplified illustration of the odd-even interlaced scanning employed by the vidicon's electron beam to retrieve video signals from the photodiode array. The odd (solid) lines are timed via synchronization pulses to start at the left side of the array; the even (dashed) lines begin in the center of the array. Both the even and odd fields ideally consist of 262.5 lines

15.7 KHz repetition rate. During the remaining 53 μs, the beam is scanning across the surface of the array and video signal is being produced. Concurrent to the horizontal scan, the vertical deflection waveform is driving the electron beam downward toward the bottom of the array; this manifests itself by the negative slope exhibited by the horizontal scans in Figure 2-10. After 1/60 sec, the vertical deflection waveform returns the electron beam to the top of the array, completing the first field. In the time it takes to complete one vertical scan, 16.67 ms, there have been 16.67 ms/63.5 μs = 262.5 horizontal scans; hence, the end of the odd-line scan and the end of first field coincide. The terminus of the odd-line scan is usually halfway across the array and even-line scan begins in that approximate position at the top of the array.

The vidicon camera assembly was mounted sideways onto the exit slit of the Czerny-Turner polychromator. This permitted the horizontally dispersed continuum signals to form two images approximately perpendicular to the horizontal sweeps across the vidicon; each horizontal line of a field sampled a different wavelength region of the dispersed spectra (Figure 2-11). Since the vertical dimension in a RCA 4532A Si diode array is 12.8 mm and the polychromator had a linear dispersion of 7.9 nm/mm, approximately 100 nm of spectral information could be viewed or recorded at any one time. A micrometer dial allowed angular positioning of the polychromator grating so that wavelengths throughout the near infrared, visible and ultraviolet could be observed.

The images of the two continua were approximately 2-2.5 mm apart on

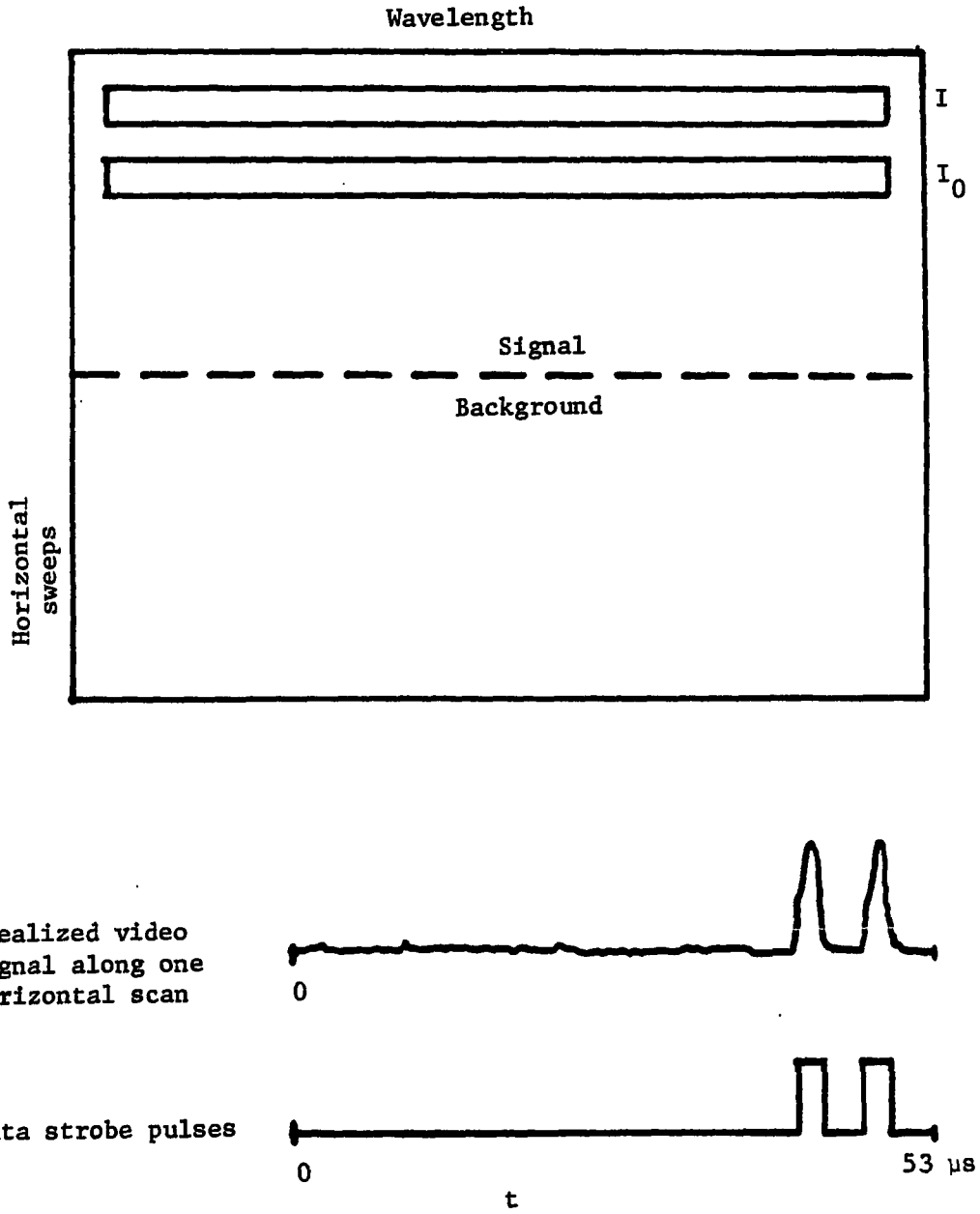

Figure 2-11. Position of the I and I_0 continuum spectra on the Si vidicon array. The lower half of the array was reserved for acquisition of background signal

the latter third of the array's horizontal dimension. The Si array wavelength dispersion was calibrated with Oriel standard mercury, argon, and krypton lamps. A least squares fit to the calibration points revealed a high degree of linearity between wavelength and spatial position on the vidicon (Figure 2-12). Since the polychromator was custom built in-house, designed using the constraints on the optics established by Reader (165), the calibration was essential to insure that the desired linear dispersion was produced by the instrument. Because there is only light intensity in two positions, corresponding to I and I_0, along the horizontal sweep, the video signal produced by a horizontal sweep is similar to the one shown in Figure 2-11. To recover these data, an electronic interface system was developed to recover the proper portion of the video signal and to store this analog signal in digital form. This interface generated two strobe pulses that coincided temporally with the desired video signal; these pulses were used to gate the video signal into a Biomation 805 transient recorder for data storage.

The electronic interface system formed the nexus for almost all the electronic components of the transient absorption experiment. Figure 2-13 is a schematic of vidicon-Biomation interface system and its relationship to the other elements of the system. The interface had two primary functions: to issue a fire pulse to the laser oscillator and amplifiers at a preset time after laser flashbank charging, and to receive, process and send the desired video signal to the Biomation 805 transient recorder. The processing of the video signal required a

Figure 2-12. Graph of spatial position on the vidicon array versus the wavelength. Open circles are the positions of standard calibration wavelengths generated from mercury, argon, and krypton arcs

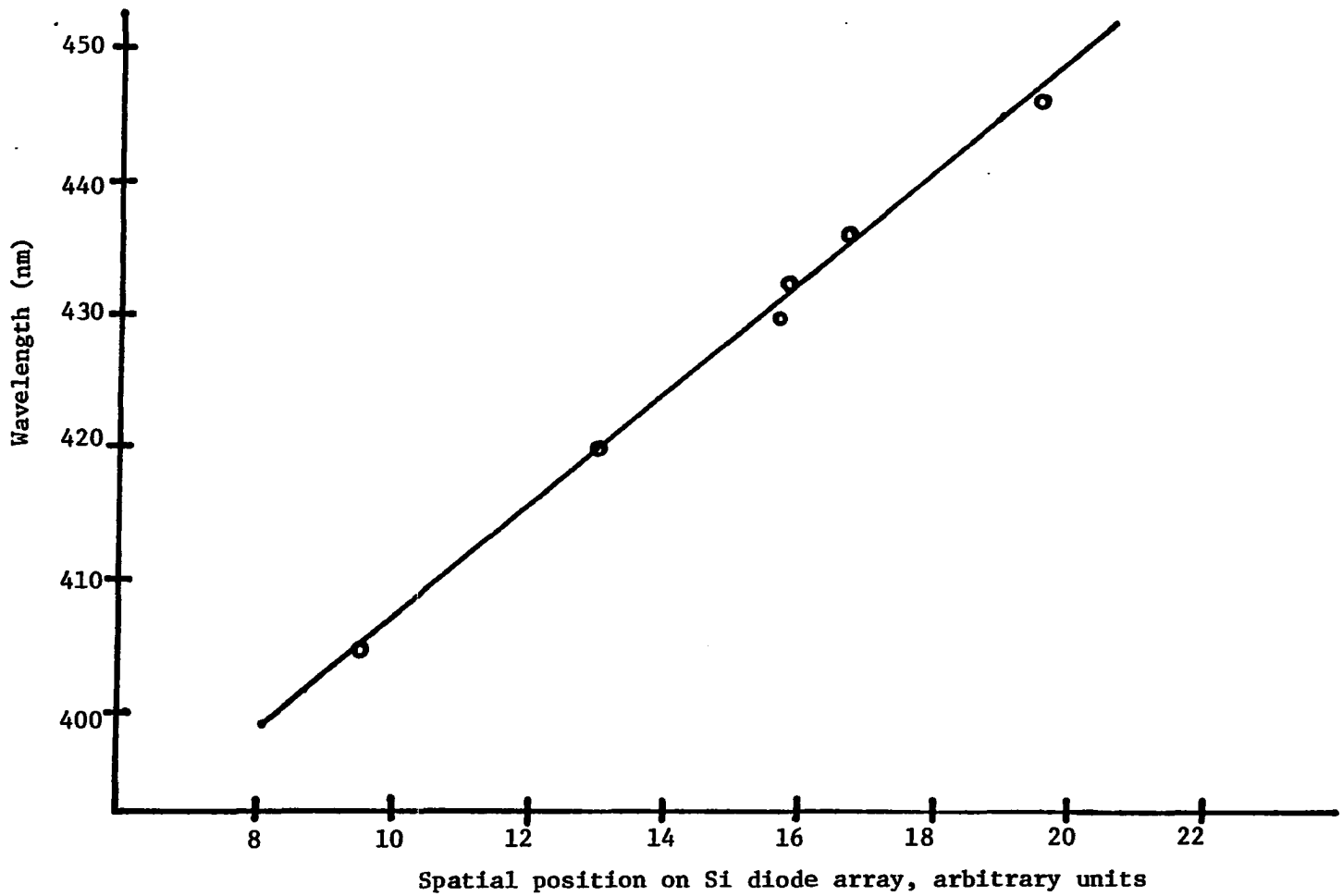
450
440
430
420
410
400
Wavelength (nm)
8
10
12
14
16
18
20
22
Spatial position on Si diode array, arbitrary units

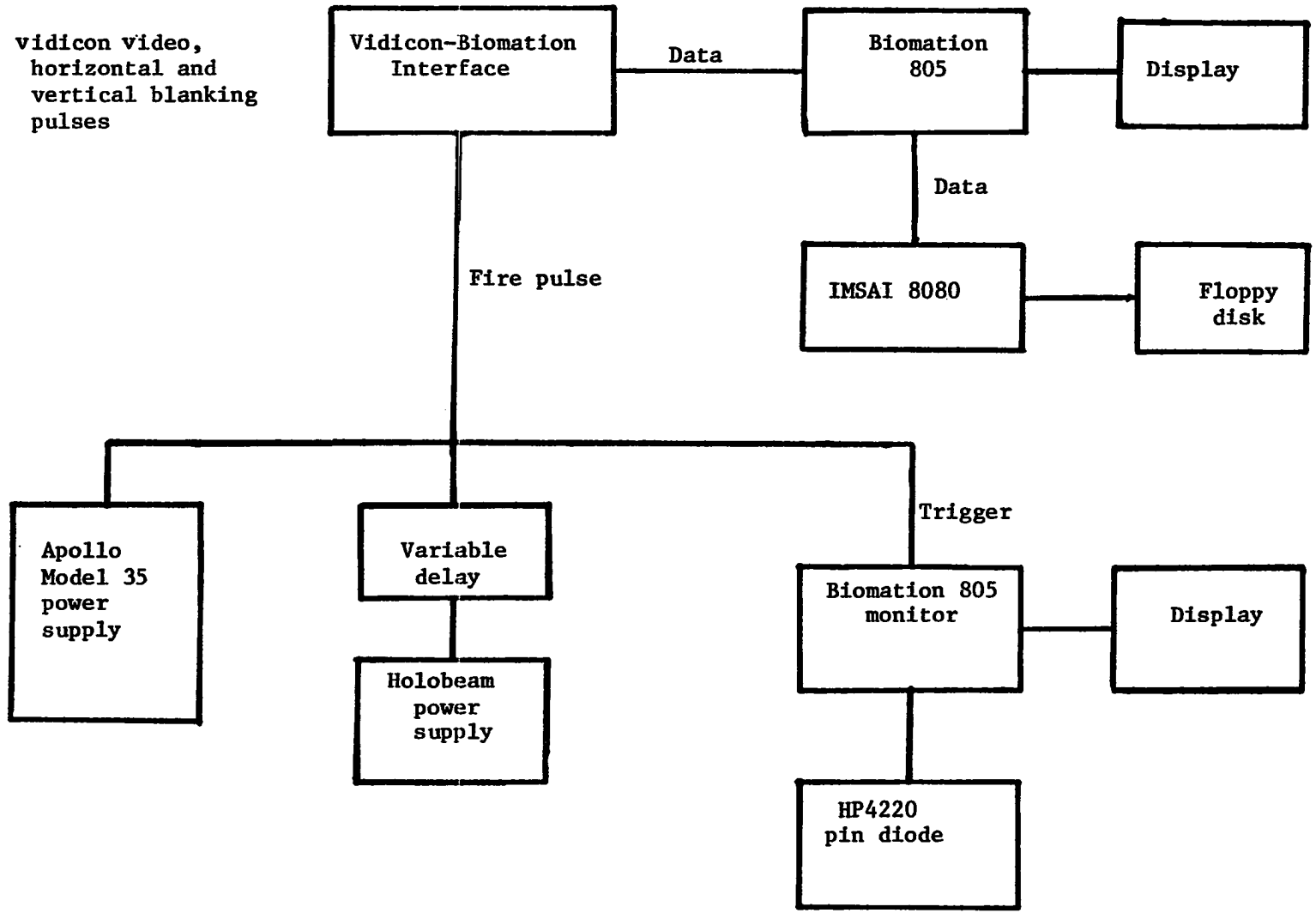

Figure 2-13. Signal processing matrix for the vidicon-interface system

background subtraction of the dark current that is always present in a silicon diode vidicon at room temperature. After the background signal was removed, the video signal was channeled into the input of a Biomation 805. The analog video signal was not stored unless there was a concurrent data strobe pulse on the external time base input of the Biomation. This prerequisite strobe pulse was produced by the timing generator of the interface, which generates the strobe pulses at preset times coincident with the time during which the electron beam is traversing the particular diodes activated by the continuum probe signals. The laser fire signal was sent to the flashbanks at a preset time delay. A detailed explanation of the background suppression circuit, the timing generator circuit and the generation of the variable delay strobe pulses in the vidicon-Biomation interface is given in Appendix C.

The Biomation 805 transient recorder can store 2.048 kilobytes of data in its RAM memory. Each byte or word consisted of 8 bits allowing a resolution of 1 part in 256. After 2.048 kilobytes of video signal were stored into the Biomation, the data points were transferred onto a floppy disk of a IMSAI 8080 microcomputer/floppy disk system by an assembler software routine. Routinely, 30-40 data files, each corresponding to an individual laser shot, would be generated in a single laser run. Four or five of these files would be background shots obtained by firing the system with a spoiled laser oscillator cavity. These data files were used for background subtraction. After a laser run was completed, the data files, which were stored in CP/M compatible

format, were reformatted from the 8080 single byte hexadecimal data into IBM 4-byte integer data by 8080 assembler software. These raw data were analyzed on an Itel AS/6 mainframe computer in the ISU Computation Center after being transferred into the system by a PDP RX11 Floppy Disk system interface.

The 2 kilobytes of data obtained for each laser shot did not consist exclusively of usable data; the vertical blanking pulses, which occurred after each field was completed, generated a series of low bytes devoid of spectral information. Each horizontal sweep recorded two bytes of data; one byte from the video signal generated by the probe continuum and one from the video signal of the reference continuum. Since there are approximately 262 scans per field, each odd field produces 524 bytes of data. The storage capacity of the Biomation, 2048 bytes, is slightly less than the 2100 bytes required to store 4 fields--two even and two odd--of data. Figure 2-14 is a representation of the distribution of useful data in a typical data file. Each data file followed a reproducible sequence: the fields consisted of 524 bytes (odd field) or 526 bytes (even field), including bytes generated by the vertical blanking pulse. In the odd fields, the vertical blanking pulse produced 12 bytes of unusable data at the beginning of the field and 2 bytes of unusable data at the end of the field; this resulted in 510 bytes of contiguous valid data points out of a possible 524 bytes. In the even fields, 14 bytes of invalid data were generated in the initial part of the scan and 2 more in the end of the field; this also resulted in 510 contiguous valid points. A Fortran program established

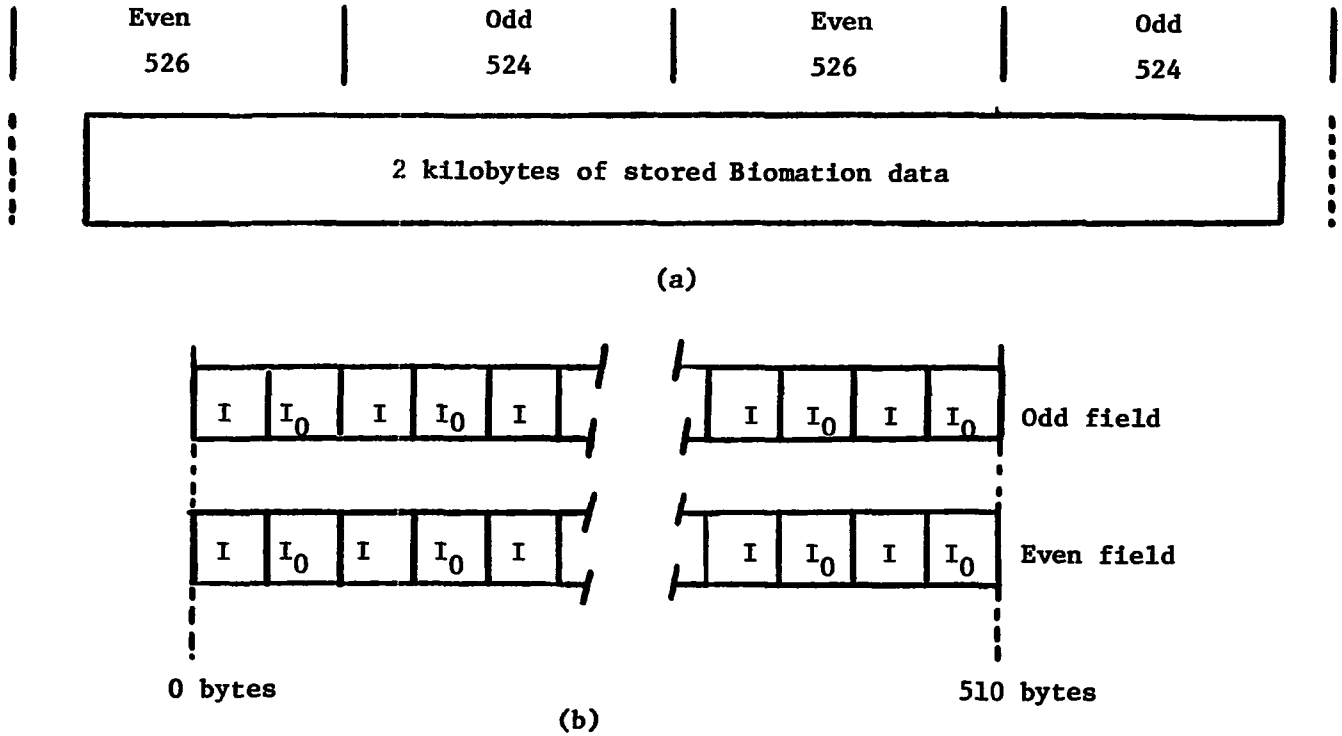

Figure 2-14. The partition of spectral data in Biomation memory
(a) The overlap of the Biomation 805 storage capability (2 kilobytes) and the 2100 bytes of data generated by 2 odd and even fields of video data
(b) Illustration of the alignment of an even and odd file of data so that a pointwise summation for each of the 510 points could be facilitated. For an actual data file, four such fields were summed

the even-odd sequence by locating the low bytes characteristic of the vertical blanking pulse and counting the number of bytes in each field, subtracted the invalid data out, and accounted for the missing bytes not recorded due to memory space limtations in the first and last fields (Figure 2-14). The four fields of 510 data points, 255 I data points and 255 I_0 data points in an alternating series, were aligned so that the intensity signals corresponding to identical spatial positions on the vidicon grid could be averaged. The resultant data file consisted of 255 averaged I data points and 255 averaged I_0 data points. The data files representing the background shots were averaged together and subtracted from the data files with spectral information. The optical densities log (I_0/I) for each of the 255 data points in the background adjusted files were calculated. Each of these 255 optical density data points was approximately 0.4 nm apart throughout the 380-480 nm region monitored in these experiments. Optical density plots were generated on a Calcomp plotter using a Simplotter routine. Figure 2-15 summarizes the data flow for these experiments.

The vidicon-Biomation apparatus described above is comparable to a commercial optical multichannel analyzer (OMA) utilized by several research groups performing similar studies (26, 27, 51, 52). Although the OMA offers a wide latitude of choices in mode of operation and data processing, none present a significant advantage over the system used in our experiments. In our system, the spectral information and the dark current are analog signals and the valid data are digitized by the Biomation after the dark signal has been subtracted; in the OMA, the

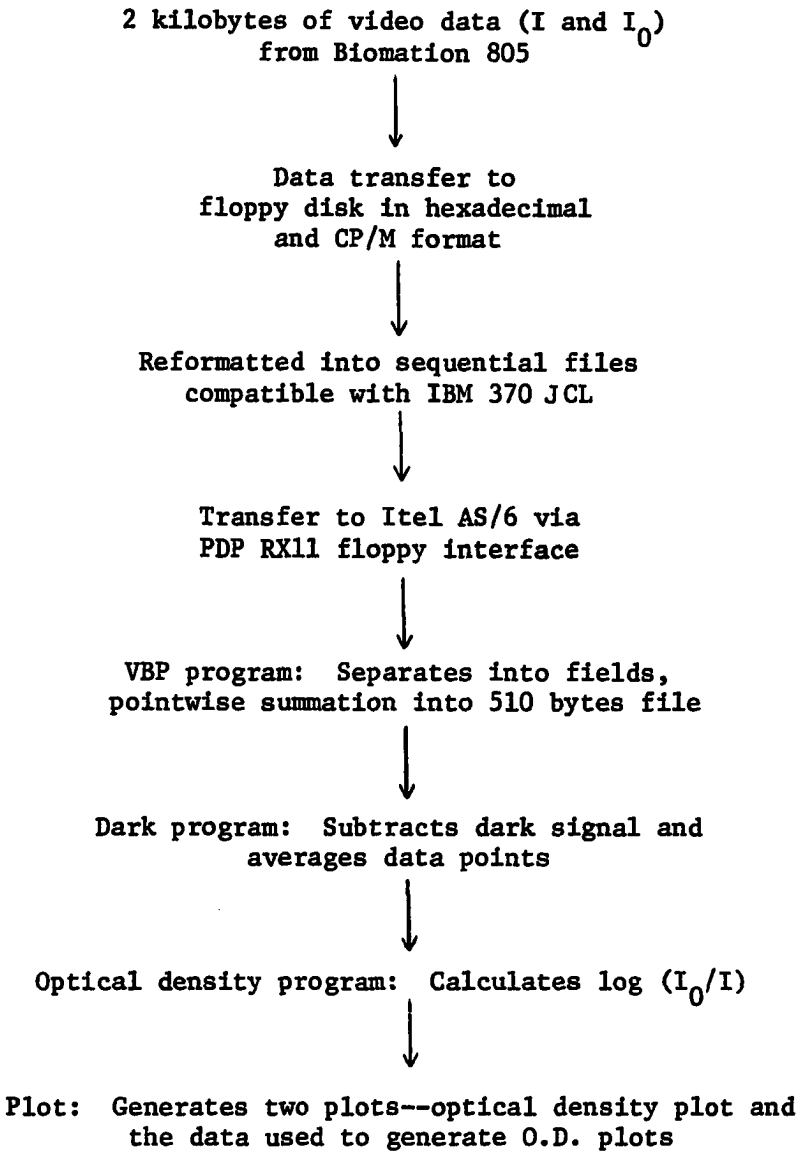

Figure 2-15. Flow diagram for software processing of video data to generate optical density plots

spectral signal and dark current signal are both digitized first and then subtracted. There seems to be no substantial differences in the quality of background signals acquired by either method (Figure 2-16c and References 27 and 51). Since the OMA's scanning mode is controlled by software routines supplied by a LSI-11 microprocessor, the scan rates can be slower than our invariant electronically controlled scan rate. Slow scan rates allow the dark noise content of a spectral signal to increase since the dark current signal increases with time. OMA scan routines must be chosen to minimize this effect. The 16 bit resolution offered by the OMA doesn't provide any significant advantage over the 8 bit resolution of the Biomation since the two continuum spectra do not differ in intensity substantially and the information about the dynamic spectral changes is derived from the log of the ratio of the two signals.

A number of experimental runs were made to determine the proper conditions to obtain data free from experimental artifacts such as poor overlap of the excitation pulse and probe pulse, saturation effects due to excessive amounts of pump energy, and satellite pulses. Vidicon nonlinearity and saturation artifacts could be detected visually by the data Biomation monitor or by examining the raw data values in the digital output for an extended series of maximum values. Experiments characterizing the continuum demonstrated that the transverse spectral distribution of the continuum (27, 166, 167) could cause nonuniform focussing of the different wavelengths present in the continuum in the sample cell. Furthermore, the angular dispersion of the continuum could cause variable

overlapping of the excitation beam and the continuum pulses. The origin of the angular dispersion, its effects on continuum probing or transients, and how one can eliminate or minimize continuum-induced artifacts on the data is treated in Chapter 3.

Typical spectra generated in these experiments are shown in Figure 2-16. Two iodoanthracenes were studied in this experiment. The 9-iodo anthracene was synthesized by catalytic reaction between iodine and anthracene with cupric fluoride as the catalyst (168). The sample was purified by column chromatography using Fluorosil, vacuum sublimation, and preparative thin layer chromatography. The 2-iodoanthracene was prepared from 2-aminoanthracene by a Grignard synthesis. It was purified by column chromatography and recrystallization. The absorption spectra of the $S_1 \leftarrow S_0$ absorption of anthracene, 2-iodoanthracene, and 9-iodoanthracene in cyclohexane is shown in Figure 2-17. Both of the halogenated anthracenes experience a bathochromic shift relative to anthracene; the 9-iodoanthracene having the larger red shift due to extension of the conjugation along the short axis by the halogen in the 9 position (169).

Summary

The neodymium-glass system described in this chapter has proven to be reasonably reliable and a valuable tool to investigate both picosecond transient absorption (170) and fluorescence phenomena (147-151, 155). During the use of this transient absorption apparatus for approximately 2 years, we have found several limitations which if eliminated

Figure 2-16. Transient absorption spectra
(a) Single-shot probe and reference continuum praise spectra transmitted by 2-iodoanthracene in cyclohexane 122 ps after 354 nm excitation;
(b) nominal optical density spectrum log (I_0/I);
(c) optical density baseline in the absence of the 354 nm excitation pulse

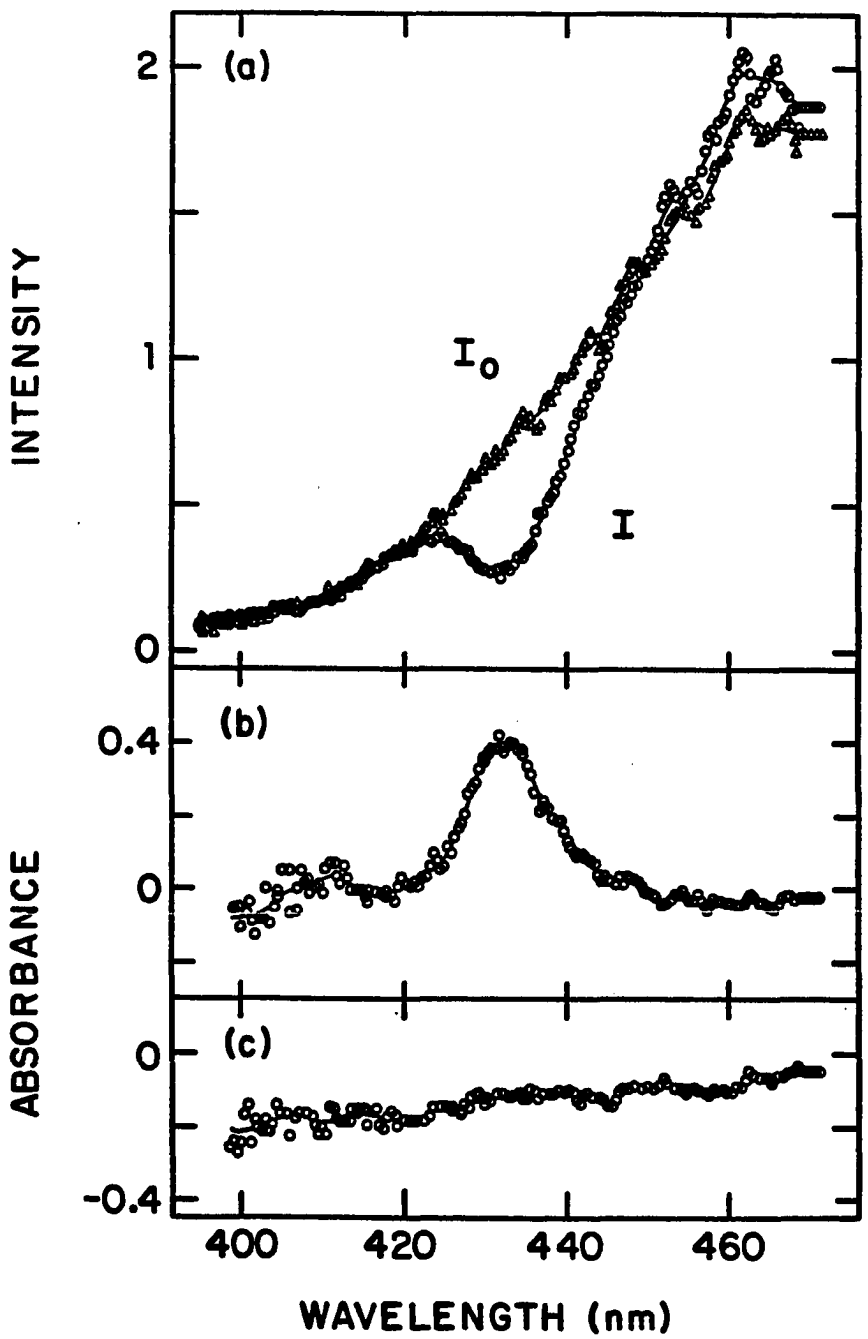
(a)
(b)
(c)
I_o
I
INTENSITY
ABSORBANCE
2
1
0
0.4
0
0
-0.4
400
420
440
460
WAVELENGTH (nm)

Figure 2-17. $S_1 \leftarrow S_0$ absorption spectra of anthracene (---), 2-iodoanthracene (-·-) and 9-iodoanthracene (——) in cyclohexane. The absorbances are not mutually normalized

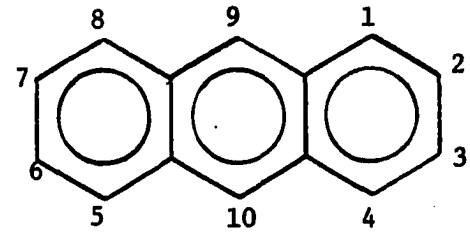
8
9
1
7
2
6
3
5
10
4

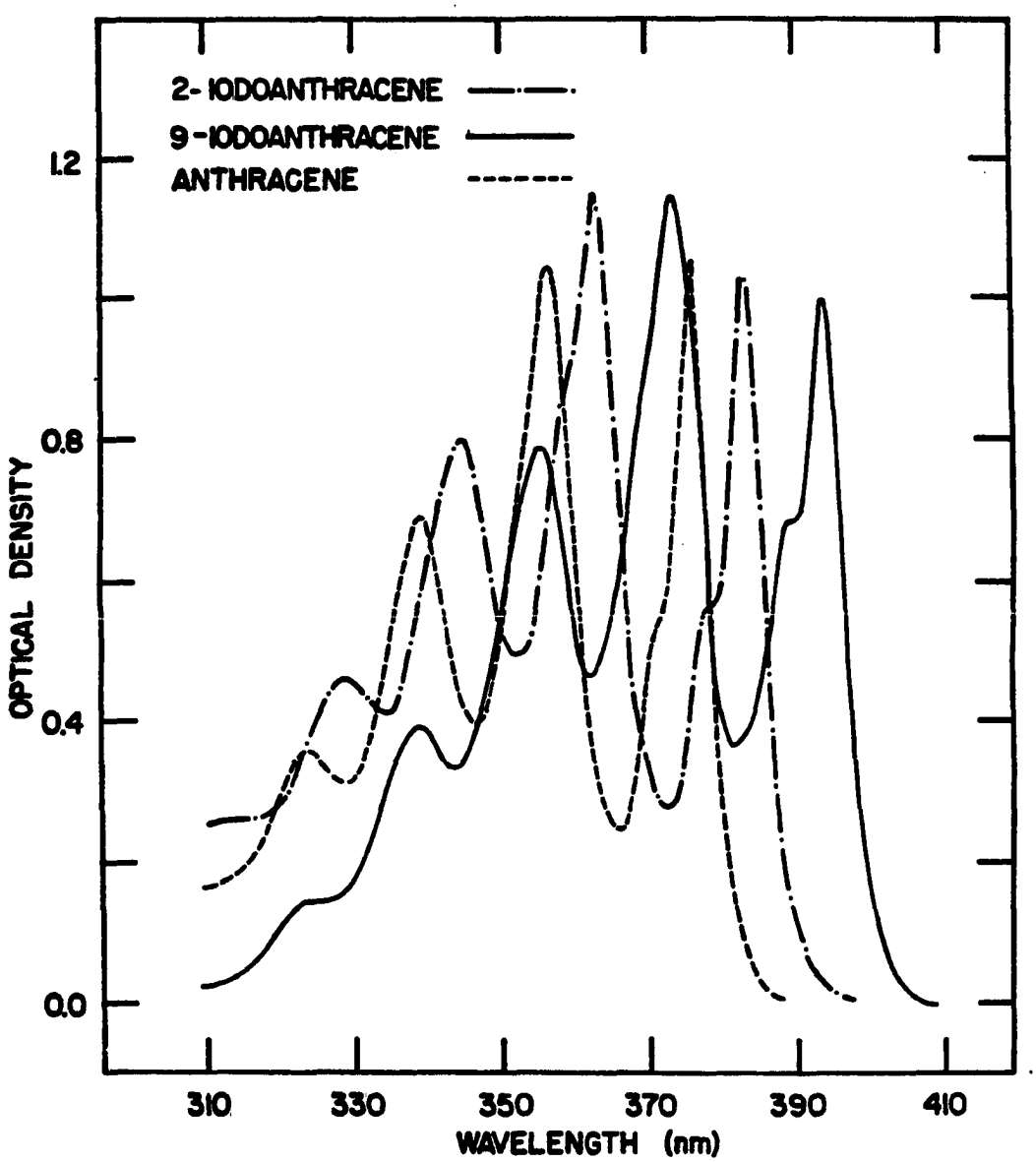
2-IODOANTHRACENE
9-IODOANTHRACENE
ANTHRACENE
OPTICAL DENSITY
1.2
0.8
0.4
0.0
310
330
350
370
390
410
WAVELENGTH (nm)

could significantly extend the capabilities of the system.

One of the less endearing characteristics of a Nd:glass oscillator is its very low repetition rate of 1 shot per minute; this translates into tedious alignment procedures, long experimental runs and little recourse to signal averaging techniques. To avoid this problem, a number of researchers have employed Nd:YAG lasers, compromising time resolution for repetition rate. Recently introduced Nd:phosphate glasses with improved thermal conductivities offer the possibility of pulses with of 5 ps fwhm at 5 Hz (55). Replacing the Nd:glass rods with phosphate glass rods is a possible solution to the low repetition rate handicap. Satellite pulses, which occur when a weak intensity pulse is allowed to propagate through a dye cell because it is coincident with a stronger counterpropagating pulse, can be eliminated by incorporating a thin dye cell (~400 μm) in optical contact with one of the mirrors of the oscillators (9, 118). Pulse widths could be reduced by ~1.5 times by placing an external saturable absorber cell prior to the amplifier chain (119). The mechanical and thermal stability of the oscillator is extremely important to the production of reliable short pulses. Our system (Figure 2-2) has shown an impressive degree of stability on a day-to-day basis; however, construction of the mount out of Invar, which has a thermal expansion coefficient ~7 times less than the carbon steel (171), utilized in our mount might improve the thermal stability of the system. The extraction of single pulses could be upgraded by replacing the inherently noisy spark gap with an all-electronic circuit to generate the high voltages necessary to activate the Pockels

cell (172).

As mentioned earlier, the transverse spectral distribution of the continuum can cause artifacts in the data if disregarded. The spatial inhomogeneities of the continuum can be eliminated by inserting a diffuser plate immediately after the continuum cell (52). Unfortunately, the diffuser also reduces the intensity of the continuum by two or three orders of magnitude. To compensate for this loss, one can employ a silicon intensified target (SIT) tube which operates in the same manner as a vidicon tube but is 100-1000 more sensitive than a silicon diode array. Implementing this detector would require a different, more expensive camera assembly designed to accommodate a SIT tube.

An extremely desirable addition to the transient absorption apparatus would be the addition of a transient recorder with substantially more memory. Currently, the data are derived from 4 fields of video information; due to the capacitance effects of the Si diode, some signal ($\lesssim$5%) still resides on the vidicon surface after 4 sweeps have been completed. An additional 2-4 kilobytes of memory would allow the acquisition of 6-8 fields of video signal which would recover all of the spectral information on the vidicon. Since the research group has recently acquired a PDP11/23 minicomputer with a Fortran compiler, it would be cost and time efficient to transfer the data analysis routines to this system from the ISU Computation Center if a hard copy graphics capability was added to the system in the near future.

CHAPTER 3

Introduction

The ability to generate picosecond continua has facilitated many picosecond experiments which would otherwise be difficult to do with the limited range of wavelengths directly available from a Nd:glass laser. In the iodoanthracenes, for example, the $T_1 \rightarrow T_n$ transient absorption maximum occurs in the vicinity of 430 nm, a wavelength region which is not near any optical harmonic of the Nd:glass laser or of picosecond dye lasers. Spectral broadening of Rayleigh and Raman lines scattered from a laser beam was observed soon after the development of the first laser (173-176), but the resulting linewidths extended only over several nanometers and were not suited for use as a spectroscopic tool (176, 177). In 1970, Alfano and Shapiro (178) reported the generation of a picosecond continuum extending over several thousand wavenumbers. In their experiment, a 532 nm picosecond pulse with an intensity of ~1 $GW \cdot cm^{-2}$ was focused into a length of BK-7 borosilicate glass, which gave a broad emission extending from 4000 Å to 7000 Å dispersed over a range of emission angles. Moreover, the continuum had a duration approximately equal to that of the picosecond excitation pulse. Further studies by these investigators showed that similar frequency broadening could be produced in both liquids and solids (179, 180). Shortly thereafter, Alfano and Shapiro utilized the continuum as a picosecond "white light" probe in an inverse Raman experiment (25). Other laser groups soon reported similar findings. Using 694 nm mode-locked ruby pulse 40

ps wide, Werneke et al. (181) observed extensive spectral broadening in H_2O, particularly in the anti-Stokes region where the continuum spanned the visible region between 694 nm and 320 nm. Rentzepis and co-workers employed D_2O and H_2O to produce continua for picosecond spectroscopic measurements (47, 182, 183). The use of liquids as the continuum generating medium avoided the optical damage that usually resulted from continuum production in glasses.

Since the laser-generated continuum provides the needed "white light" extension to the quasi-monochromatic laser wavelengths with the added bonus of picosecond time resolution, this technique has become standard in almost all picosecond laboratories working with solid state lasers (3, 110, 184). Unfortunately, complete understanding and agreement on the relative importance of the processes believed to be responsible for the conversion of an intense quasi-monochromatic picosecond laser pulse into a broadband continuum has not yet materialized, despite the efforts of a number of competent research groups (178-183, 185-189). Continuum emission is generally polarized parallel to, and is of roughly the same duration as, the excitation pulse. Furthermore, the continuum intensity is a nonlinear function of incident excitation pulse power. The onset of the continuum occurs over a relatively narrow range of exciting pulse intensities, and quickly saturates (185, 189). This behavior can be a consequence of several different nonlinear processes (vide infra) occurring separately or simultaneously, and depends on the experimental conditions and nonlinear medium used to generate the white light.

Nonlinear Mechanisms for Continuum Generation

The understanding of the possible mechanisms of production of picosecond continuum light requires familiarity with nonlinear optics. Excellent reviews and texts on nonlinear optics are available in the general area of nonlinear optics (134, 190-192) and in the specific area of spectral broadening (135, 189, 193); below, we present a general introduction to the important phenomena for continuum generation. As with many young fields of research, much of the literature of nonlinear optics is presented with different notations and conventions. In the discussions presented within, we will utilize the conventions established by Terhune and Maker (191). Electrostatic units (esu) and MKS units are both used.

When an electromagnetic field interacts with a medium, a polarization field is induced due to the response of free and bound charges to the initial $\underset{\sim}{E}$ field. This resultant polarization field is usually expressed as an expansion in terms of the total electric field present,

$$\underset{\sim}{P} = \chi^{(1)} \cdot \underset{\sim}{E} + \chi^{(2)} : \underset{\sim}{E}\underset{\sim}{E} + \chi^{(3)} \vdots \underset{\sim}{E}\underset{\sim}{E}\underset{\sim}{E} + \ldots \qquad (3.1)$$

The χs are susceptibility tensors which depend on the spatial coordinates of the medium, the frequency and polarization of the electromagnetic fields, and the physical properties of the medium. These susceptibilities couple the electromagnetic fields to the polarization wave within the medium. $\chi^{(1)}$ is the complex first-order susceptibility, the dominant term in the series when the electric fields are not large; the real part determines the magnitude for the linear dispersion and

the imaginary portion determines the value for the one-photon absorption cross section for the medium. Typical absolute values for χ are on the order of 10^{-1} esu (1 esu = 300 V/cm). In comparison, $\chi^{(2)}$ and $\chi^{(3)}$ values range from approximately 10^{-7}-10^{-9} esu and 10^{-11}-10^{-13} esu, respectively. Unless the magnitudes of electromagnetic fields present are large, the optical phenomena mediated by these weak higher order susceptibilities are negligible. The $\chi^{(2)}$ term couples two electric fields together to generate phenomena such as second harmonic generation and optical rectification; $\chi^{(3)}$ couples three fields to create coherent Raman effects, third harmonic generation, self-action phenomena, and the optical Kerr effect.

In isotropic media including liquids, $\chi^{(2)}$ is zero by symmetry, and $\chi^{(3)}$ becomes the dominant nonlinear term. All of the nonlinear phenomena cited as being responsible for continuum generation--self-action effects, Stokes and anti-Stokes scattering, parametric generation and avalanche ionization--are third order effects, and therefore are determined by the $\chi^{(3)}$ susceptibility. Because the thresholds in intensity for the observation of these effects lie very close to each other, discrimination between the various phenomena and selective activation of a phenomena can be very difficult to achieve (194).

If one expands the polarization density in terms of the incident electric fields, the third order term at time t can be expressed (195),

$$P_i(t) = \sum_{jk\ell} \chi^{(3)}_{ijk\ell} E_j(t)E_k(t)E_\ell(t) \qquad (3.2)$$

where the subscripts designate the Cartesian coordinates of the tensor

quantity. It is convenient to expand the polarization and the electric fields in terms of their Fourier expansions and deal with the individual frequency components. The third order contribution at a given frequency, say ω_δ, to the total polarization density can be written, using equation 3.2,

$$P_i(\omega_\delta) = \sum_{jk\ell} \chi^{(3)}_{ijk\ell}(\omega_\delta;\omega_\alpha,\omega_\beta,\omega_\gamma)E_j(\omega_\alpha)E_k(\omega_\beta)E\ (\omega_\gamma) \qquad (3.3)$$

where $\omega_\delta = \omega_\alpha + \omega_\beta + \omega_\gamma$, and the summation is performed over all possible spatial components of the incident fields. The third order susceptibility tensor is written in Maker-Terhune notation (191). Since we are using linearly polarized light, the third order nonlinear susceptibility pertinent to continuum generation is $\chi^{(3)}_{iiii}$, where all three of the initial electromagnetic waves, regardless of frequency, and the polarization wave have the same polarization.

Self-action phenomena

The term self-action refers to a process that is induced by the electromagnetic field of the laser alone, and not due to some other electric field present. It is thus governed by the susceptibility term $\chi^{(3)}(-\omega_L;\omega_L,\omega_L,-\omega_L)$.

Self-action processes have been studied extensively by researchers attempting to avoid optical damage to laser components caused by the intense electric fields that are produced by self-action (196). When a laser pulse propagates through a medium, the intense electric field of the laser induces a change in the refractive index proportional to

the square of the electric field,

$$\Delta n = \eta_2 \langle E^2(t,z)\rangle = \eta_2 \frac{E_0^2}{2}(t,z) \quad , \tag{3.4}$$

where η_2 is the nonlinear index of refraction and $\langle E^2(t,z)\rangle$ is the time-averaged field. The magnitude of nonlinear index of refraction depends on the physical mechanism responsible for it. In liquids, typical values range from 10^{-11} to 10^{-13} esu. CS_2, an anisotropic Kerr molecule, has a value of $\sim 200 \times 10^{-13}$ esu, derived primarily from the orientational Kerr effect. In contrast, in CCl_4, a liquid composed of nonpolar molecules, or in rigid media such as a glass, the dominant effect is electronic hyperpolarizability, which is weaker by approximately 2 orders of magnitude ($\sim 1 \times 10^{-13}$ esu) (197). Electrostriction, molecular clustering, and thermal index changes are other possible contributing mechanisms to the magnitude of η_2; however, the response times of electrostriction and thermal index changes are on the order of nanoseconds and, unless trains of picosecond pulses are used, are not significantly activated by picosecond pulses. However, reorientational Kerr processes, with response times on the order of or less than tens of picoseconds, and electronic distortion with femtosecond response times are easily activated by picosecond pulses, and can contribute strongly to the magnitude of the nonlinear refractive index.

The relationship between the susceptibility and the nonlinear index can be derived from the familiar equation used in linear optics:

$$n^2 = 1 + 4\pi\chi = \varepsilon\mu \tag{3.5}$$

$$D = \varepsilon \underline{E} = \underline{E} + 4\pi \underline{P} \tag{3.6}$$

where n is the index of refraction, ε is the dielectric constant, D is the electric displacement vector, and μ is the magnetic permeability (approximately equal to 1 in CCl_4). In an isotropic medium,

$$P(z,t) = \chi_0^{(1)} E(z,t) + \chi_0^{(3)} E^3(z,t) \tag{3.7}$$

so that

$$\begin{aligned} D(z,t) &= E(z,t) + 4\pi\, P(z,t) \\ &= E(z,t) + 4\pi\{\chi_0^{(1)} E(z,t) + \chi_0^{(3)} E^3(z,t)\} \quad . \end{aligned} \tag{3.8}$$

Expressing $E(z,t) = E_0(z,t) \cos(\omega_L t)$ and substituting into equation 3.8,

$$\begin{aligned} D(z,t) &= E(z,t) + 4\pi\{\chi_0^{(1)} E(z,t) + 0.25\, \chi_0^{(3)} E_0^3(z,t)[3\cos(\omega_L t) \\ &\qquad + \cos(3\omega_L t)]\} \\ &\cong E(z,t) + 4\pi\, \chi_0^{(1)} E(z,t) + 3\pi\, \chi_0^{(3)} E_0^3(z,t) \cos(\omega_L t) \\ &\cong [1 + 4\, \chi_0^{(1)} + 3\pi\, \chi_0^{(3)} E_0^2(z,t)]\, E(z,t) \quad , \end{aligned} \tag{3.9}$$

where the $\cos(3\omega_L t)$ has been suppressed because it doesn't contribute to the polarization at ω_L. Using $n = n_0 + \Delta n$ and equations 3.4-3.6,

$$\begin{aligned} D(z,t) = n^2 E(z,t) &\cong (n_0^2 + 2n_0 \Delta n)\, E(z,t) \\ &\cong [n_0^2 + n_0 \eta_2\, E_0^2(z,t)]\, E(z,t) \quad , \end{aligned} \tag{3.10}$$

where the fact that $\Delta n << 1$ has been used.

By definition (191),

$$n_0^2 = 1 + 4\pi\ \chi_0^{(1)}$$

$$\chi_0^{(3)} = \frac{4}{3}\,\chi^{(3)}(-\omega_L;\omega_L,\omega_L,-\omega_L)$$

so that comparing equation 3.9 and 3.10 yields

$$n_2 = \frac{3\pi}{n_0}\,\chi_0^{(3)} = \frac{4\pi}{n_0}\,\chi_{1111}^{(3)}(-\omega_L;\omega_L,\omega_L,-\omega_L)\ . \qquad (3.11)$$

The third order nonlinear susceptibility, $\chi^{(3)}$, has contributions from 3 different processes (189, 191) and can be expressed as

$$\chi^{(3)} = D\chi_{NR}^{(3)} + \chi_I^{(3)} + \chi_R^{(3)}\ . \qquad (3.12)$$

The χ_R term contains the contribution from Raman type resonances, χ_I contains single photon resonances, and χ_{NR} represents an almost frequency independent contribution from nonresonant processes. The D coefficient equals 1 when all three frequencies are the same, 3 when two frequencies are the same, and 6 when all three frequencies are different. In CCl_4 with ω_L = 532 nm, there are no one- or two-photon resonances; χ_I and χ_R are thus negligible and

$$\chi^{(3)}(-\omega_L;\omega_L,\omega_L,-\omega_L) = 3\ \chi_{NR}^{(3)}\ . \qquad (3.13)$$

The intensity-dependent index of refraction causes 3 types of self-action: self-steeping, self-phase modulation, and self-focusing. Self-steeping is a process in which the laser pulse shape is distorted as it propagates through the medium principally because the most intense portion of the pulse experiences a larger index of refraction than the less intense portion. DeMartini et al. (124) has discussed this phenomenon

and concluded that it causes spectral broadening only in the case where the optical path length through medium is very long (>30 cm for CS_2). Since we used a shorter cell (20 cm) and a liquid which has a nonlinear index of refraction 2 orders of magnitude less than that of CS_2, self-steeping does not contribute significantly to our continuum generation process.

Self-phase modulation is the result of a rapidly changing refractive index. When the refractive index changes, the k vector of the electromagnetic wave can be written,

$$k = \frac{\omega_L n}{c} = \frac{\omega_L}{c} (n_0 + \Delta n) \tag{3.14}$$

and then substituted into the associated electric field to yield

$$\begin{aligned} E(z,t) &= E_0 \cos (\omega_L t - kz) \\ &= E_0 \cos (\omega_L t - \frac{\omega_L n_0 z}{c} - \frac{\omega_L}{c} \Delta n\, z) \\ &= E_0 \cos (\omega_L t - k_0 z - \frac{\omega_L}{c} n_2 \overline{E^2(t)} \cdot z) , \end{aligned} \tag{3.15}$$

where equation 3.4 has been used.

The instantaneous frequency is

$$\begin{aligned} \omega &= \frac{\partial \phi}{\partial t} = \frac{\partial}{\partial t} (\omega_L t - \frac{\omega_L}{c} \Delta n \cdot z) \\ &= \omega_L - \frac{\omega_L z}{c} \frac{\partial}{\partial t} \Delta n \quad . \end{aligned} \tag{3.16}$$

One can now find the maximum frequency bandwidth due to self-phase modulation from

$$\Delta\omega = \frac{\omega_L}{c} z \left[\frac{\partial}{\partial t} \Delta n \Big|_{max} - \frac{\partial}{\partial t} \Delta n \Big|_{min} \right]$$

$$\cong 2 \frac{\omega_L}{c} z \frac{\Delta n}{\Delta t_p} \qquad (3.17)$$

where Δt_p is the pulse duration. For a pulse with rapidly rising and falling edges, there will be both positive and negative changes in index of refraction resulting in spectral broadening on both sides of the laser frequency.

The last of the self-action effects, self-focusing, is due to the transverse index of refraction variation of the propagating pulse (192, 198, 199). Considering the TEM_{00} mode of a laser (a Gaussian intensity distribution decaying radially from the center of the laser spot), the medium experiences a stronger electric field in the center of the beam than near the edges. The center portion acquires a phase delay with respect to the exterior portions and the medium behaves as though it were a converging lens (Figure 3-1a). Since the focusing serves to reduce the area of the beam, the local beam intensity rises, increasing the nonlinear effect. Self-focusing, in its early stages, is therefore synergistic.

The incident power in a pulse which is critical for the occurrence of self-focusing is (199)

$$P_{cr} = \frac{(1.22\ \lambda)^2\ c}{128\ \eta_2} \quad . \qquad (3.18)$$

As the beam diameter shrinks, the tendency to diffract increases, and the latter competes with self-focusing. If the two processes

Figure 3-1. Self-focusing phenomena

(a) Self-focusing of a colliminated Gaussian laser pulse; z_f is the focal point beyond which "filamentation" occurs

(b) Variation in z_f with the time-dependent Gaussian input pulse. When the power within the pulse exceeds that necessary for self-focusing, P_{cr}, z_f follows a trajectory that first moves toward the incident surface of the cell (a,b,c) and then moves away from it (d,e); d_c is the distance in arbitrary units within the cell

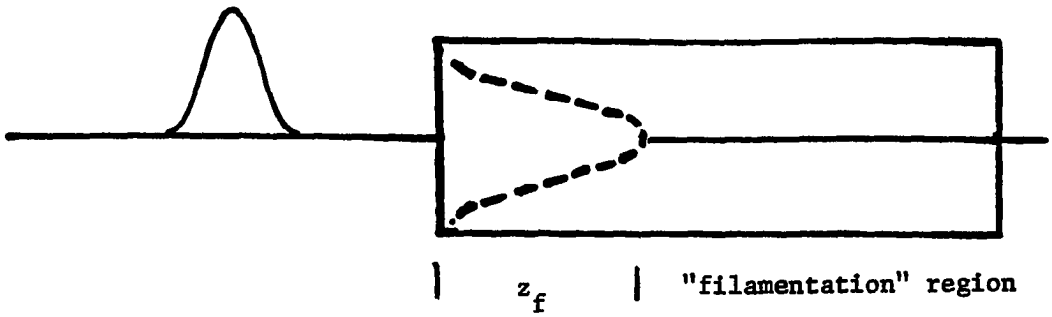
z_f
"filamentation" region

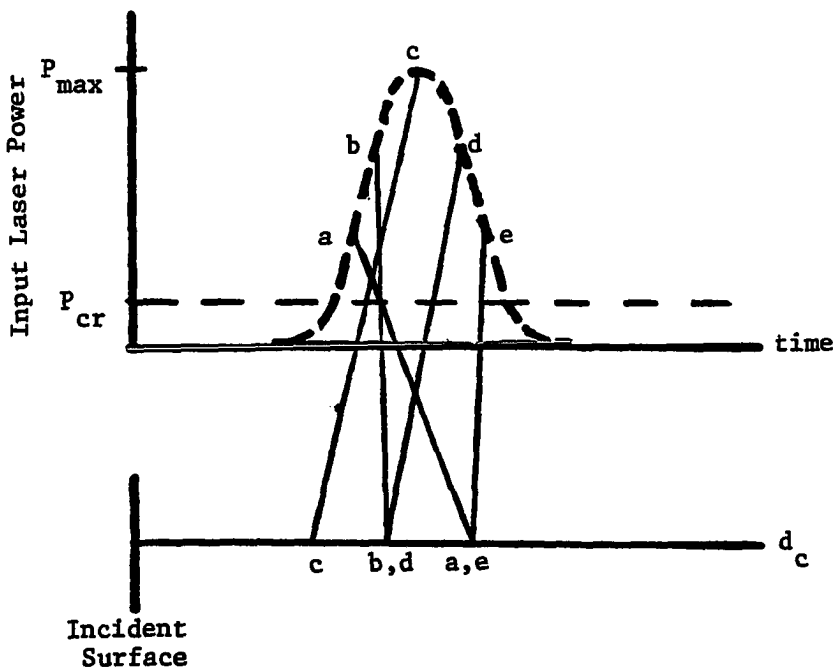
Input Laser Power
P_{max}
P_{cr}
a
b
c
d
e
time
c
b,d
a,e
d_c
Incident Surface

balance, the pulse propagates without change in profile, and is referred to as "self-trapping". In early stages of research on the self-focusing phenomena, this self-trapping was cited as the cause of "filamentation", the appearance of small streaks of light that could be photographed in the self-trapped region of the medium (200, 201). These "filaments" are actually the manifestation of the tracks of the power-dependent moving foci (202) (Figure 3-1b). The focal point, z_f, of the self-focusing phenomena depends on the power in the time-dependent laser pulse via (189)

$$z_f(t) = (0.135)^{\frac{1}{2}} k\, a^2 \{[P(t)/P_{cr})^{\frac{1}{2}} - 0.852]^2 - 0.0219\}^{-\frac{1}{2}} , \qquad (3.19)$$

where P(t) is the time-dependent incident power, k is the wave vector, and a is the incident beam diameter.

Both equations 3.18 and 3.19 were derived for single mode Gaussian pulses. Theoretical analyses of self-focusing phenomena using multimode pulses typical of Nd:glass picosecond pulses have proven difficult to accomplish satisfactorily by either analytical or numerical methods, so the foregoing equations are the best estimates currently available for our conditions. The interested reader may find thorough treatments on self-focusing processes in Shen's experimental review (198) and Marburger's theoretical review (199).

The relevance of self-focusing to spectral broadening is twofold; first, the rapidly changing index of refraction caused by the moving foci can generate self-phase modulation and second, it concentrates the laser power into regions 10-25 microns in diameter, triggering

other nonlinear processes that require large local light power densities, such as stimulated Raman scattering (203, 204), avalanche ionization (167), and parametric generation (189).

Stimulated Raman processes

Several research groups have reported that the generation of a continuum is often accompanied by easily detectable Stokes and anti-Stokes Raman lines. Alfano et al. (205), in a study on nonlinear effects in liquid lasers, reported up to 8 anti-Stokes and 5 Stokes Raman lines superimposed on a spectrally broad continuous background generated by focusing a picosecond 532 nm pulse into a 50 cm cell containing $POCl_3$. Both Varma and Rentzepis (183) using 532 nm pulses and Werneke et al. (181) using 1.06 μm pulses have reported anti-Stokes lines in continua generated in H_2O. Of particular concern to us are the processes which are responsible for the production of the anti-Stokes continuum, since this is the portion of the continuum we used in our iodoanthracene experiments.

When anti-Stokes light is generated after an intense laser pulse has been directed into a dispersive liquid, the emitted radiation, which forms concentric circles around the laser beam axis, is generally one of two types first distinguished by Garmire (206). The first type, Class I, is characterized by off-axis angles which conform to those required by the volume phase-matching conditions,

$$\bar{k}_n = \bar{k}_{n-1} + \bar{k}_L - \bar{k}_s \qquad (3.20)$$

represented schematically by the vector diagram

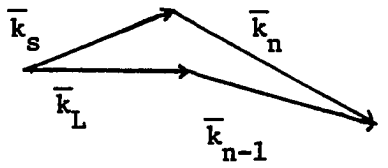

where $\bar{k}_n$ is the wave vector for the n^{th} order anti-Stokes line, $\bar{k}_{n-1}$ is the $n-1^{th}$ anti-Stokes wave vector, $\bar{k}_L$ is the laser wave vector, and $\bar{k}_{-1}$ is the first-order Stokes wave vector. Volume phase matching conditions were derived by several authors (207, 208) and were confirmed experimentally by Chiao and Stoicheff (209) for anti-Stokes emission in calcite. Class II emission is produced in liquids which are undergoing self-focusing. This type of emission is noticeably distinct from Class I: the emission angles for Class II are approximately 30% larger than Class I angles, the anti-Stokes lines are considerably more diffuse, especially under multimode laser excitation, and the emission is not affected by variations in the focusing properties of the laser pulse (206). Garmire's work demonstrated that the Class II emission emerged from the "filaments", or the perturbed region caused by the self-focusing of the laser, and that the substantial portion of the first-order Stokes stimulated Raman light was generated on-axis (210). Shimoda (211), in a theoretical study of Class II anti-Stokes emission, derived the equation,

$$\phi_n^2 = 2\,\frac{\Delta k_n}{|k_n|} + \frac{k_{n-1}}{|k_n|}\,\phi_{n-1}^2 \qquad (3.21)$$

where $\Delta k_n = |k_n| - |k_{n-1}| + |k_{-1}| - |k_0|$, which allows the calculation of the Class II emission angles. He further demonstrated the two

classes had different spectral angular distributions because the self-focusing phenomena confined the first-order Stokes to small angles with the beam axis.

In general, picosecond-excited stimulated Raman scattering has been shown by Colles (212) to be efficient in liquids with low dispersion. He reported achieving Stokes intensities of approximately 50% of the laser intensity.

Another possible mechanism that can give red- and blue-shifted light is four photon parametric generation, in which 2 laser photons scatter coherently into a Stokes and anti-Stokes photon, $2\ \omega_L \rightarrow \omega_A + \omega_S$ (213). This process can be initiated by quantum noise or by spontaneous Stokes emission.

As in the case of stimulated Raman scattering, four photon mixing has noncollinear phase matching conditions given by

$$\bar{k}_L + \bar{k}_L = \bar{k}_S + \bar{k}_{AS} \quad , \tag{3.22}$$

and schematically:

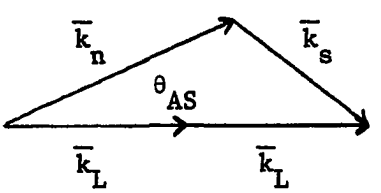

The off-axis anti-Stokes emission can be calculated from geometrical considerations by (135)

$$\cos \theta_{AS} = \frac{4k_L^2 + k_{AS}^2 - k_S^2}{4\, k_{AS} k_L} \quad . \tag{3.23}$$

Parametric generation can produce other wavelengths besides Raman lines based on vibrational frequencies of the medium, and are considered in the next section.

Parametric four wave mixing

Penzkofer et al. (185, 186, 189) has done extensive studies on the spectral broadening exhibited by H_2O when pumped by 1.06 micron pulses. From the results of his work, Penzkofer has suggested that at low input intensities and in the absence of self-focusing, the primary process responsible for continuum generation is parametric four wave mixing, in which 2 laser photons scatter into signal and idler photons, $\omega_L + \omega_L \rightarrow \omega_S + \omega_i$. The idler photon, ω_i, corresponds to an infrared resonance frequency initially present only as quantum noise (zero-point fluctuations). At low input intensities, the continuum is structured with prominent peaks at frequencies suggestive of the process $\omega_S = 2\omega_L - \omega_i$, where ω_i is an infrared resonance of the medium. As the input intensity is gradually increased, the continuum loses structure, presumably due to secondary parametric processes of the type $\omega_L + \omega_S \rightarrow \omega_S' + \omega_i'$. Similar experiments using CCl_4 instead of water showed the threshold for activating Raman processes to be lower than the threshold for four-wave parametric processes. The Raman gain factor for CCl_4 is approximately a factor of 10 greater than that for H_2O (213), and that could play a role in determining which processes occur first. Penzkofer

et al. have also performed nonresonant four wave experiments in H_2O using 532 nm photons as pump sources (214). In our experiments, we used 532 nm pulses to initiate spectral broadening; however, in contrast to the situation with H_2O, the energy content in 2 532 nm photons (~37.736 cm^{-1}) is resonant with the first UV absorption band of CCl_4 (215). In Penzkofer's treatment of parametric interactions in H_2O (189), such two-photon resonances were not incorporated into the resonant structure of $\chi^{(3)}$ because he only considered the case when one was using two infrared photons as pump sources, so it is not clear whether or not one can extend his results to systems which do have these resonances. Alfano and Shapiro (178) also suggested that nondegenerate four-photon parametric emission was responsible for their continuum produced in BK7 glass.

Avalanche ionization

Bloembergen (187) has suggested that the origin of the anti-Stokes broadening could be explained by self-phase modulation due to the very rapid change in refractive index that accompanies avalanche ionization. This mechanism has received a considerable amount of scrutiny by various researchers (185-187, 189, 216, 217). Smith et al. (167) performed a series of experiments using Nd:YAG pulses to activate spectral broadening in H_2O. Their results which indicated that power levels sufficient to cause catastrophic self-focusing and dielectric breakdown were required for spectral broadening seem to be at variance with Penzkofer's results for four-photon parametric interactions (185, 186, 189), which allow spectral broadening at power levels considerably below the avalanche ionization threshold.

Calculations by Brounlich and Kelley (217) seem to indicate that avalanche ionization thresholds need not be reached to achieve spectral broadening, and Yu et al. used Bloembergen's results to satisfactorily explain spectral broadening in NaCl, which has no infrared vibrational resonances to help mediate parametric processes (216). Although the role this mechanism plays in spectral broadening has not been completely determined, it is very likely dependent on the experimental conditions employed to generate the broadening. Smith et al. (167) and Yu et al. (216) both had self-focusing occurring during the experiments, whereas Penzkofer et al. (189) deliberately avoided self-focusing by using low-intensity collimated light and short continuum cells.

Continuum Generation (Experimental)

Each of the processes discussed in the foregoing section can generate continuum radiation. In an effort to elucidate the most probable ones that occur in CCl_4 using picosecond 532 nm pulses with our optical arrangement (Figure 2-8), we undertook a qualitative survey of the effects of input intensity variations on the spectral characteristics of the continuum. Carbon tetrachloride has been used extensively as a continuum medium in several experiments (32, 120, 110) and it was used here because it gave the strongest continuum in the region of interest, 400-500 nm, when tested under the same conditions of two other commonly used continuum liquids, phosphoric acid and 1-octanol. Typical pulses used to generate the continuum were single 532 nm picosecond pulses (~7 GW). These pulses were focused approximately 1 cm behind the

incident surface of the 20 cm continuum cell. The intensity of the 532 nm pulses could be varied by altering the input voltages to the laser amplifier flashlamp capacitor banks. On occasion, neutral optical density filters were used to attenuate either the continuum or the 532 nm pulses.

Using equation 3.18 with the relevant parameters, $\eta_2 = 2.5 \times 10^{-13}$ esu (40) and $\lambda = 532$ nm, the estimated critical power to initiate self-focusing in CCl_4 is 3.95×10^{12} esu (3.95×10^5 watts). For a typical incident 532 nm laser pulse with $P = 7.14 \times 10^{15}$ esu (7×10^8 watts) and a diameter of ~1 mm, the self-focusing distance, z_f, is ~15 cm (equation 3.19). This applies to an unfocused beam entering the cell; however, we deliberately focused our pump pulse, and therefore there is reason to believe that self-focusing intensities (10^{10}-10^{11} watts/cm^2) were present in the medium.

Spectra of the continua excited in CCl_4 obtained for different intensities of the second harmonic pulse are shown in Figure 3-2. Broadening of the 532 nm pulse was generally on the order of 200 cm^{-1}. At low input intensities ($\lesssim$ mj of 532 nm), Figures 3-2a and 3-2b display some Stokes structure on the shoulder of the 532 nm pulse. In both cases, ω_S indicates the approximate wavelengths of the 460 cm^{-1} Raman line of CCl_4. In CCl_4, the totally symmetric mode has the strongest Raman activity, and is the only mode which undergoes significant stimulated Raman emission (113).

Figure 3-2b was taken at a slightly higher intensity than Figure 3-2a, and shows significant Stokes Raman activity. There was no

Figure 3-2. Continuum spectra generated for different input intensities of 532 nm pulses. ω_L indicates position of the 532 nm pump pulse; ω_S indicates approximate positions of the Stokes and anti-Stokes Raman lines. See text for discussion

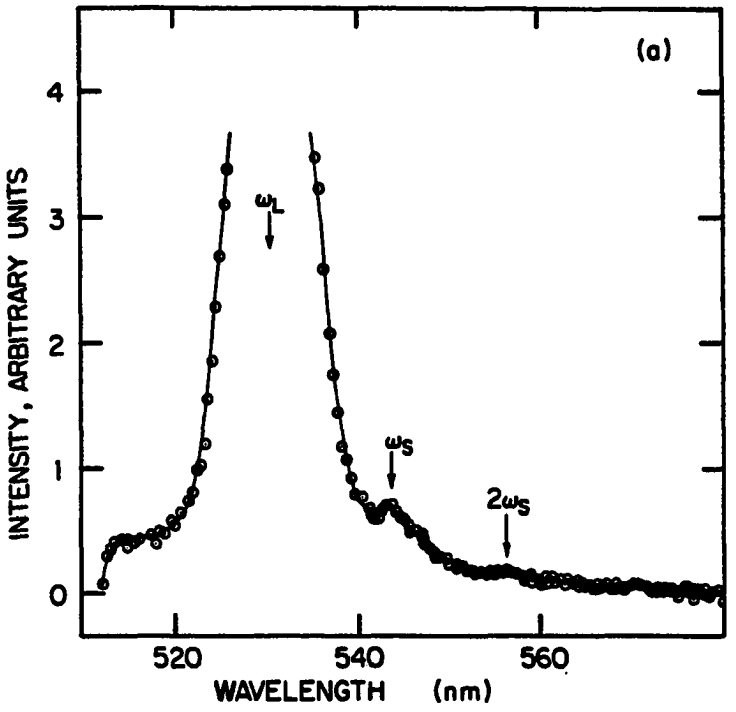
(a)
INTENSITY, ARBITRARY UNITS
0
1
2
3
4
ω_L
ω_S
$2\omega_S$
520
540
560
WAVELENGTH (nm)

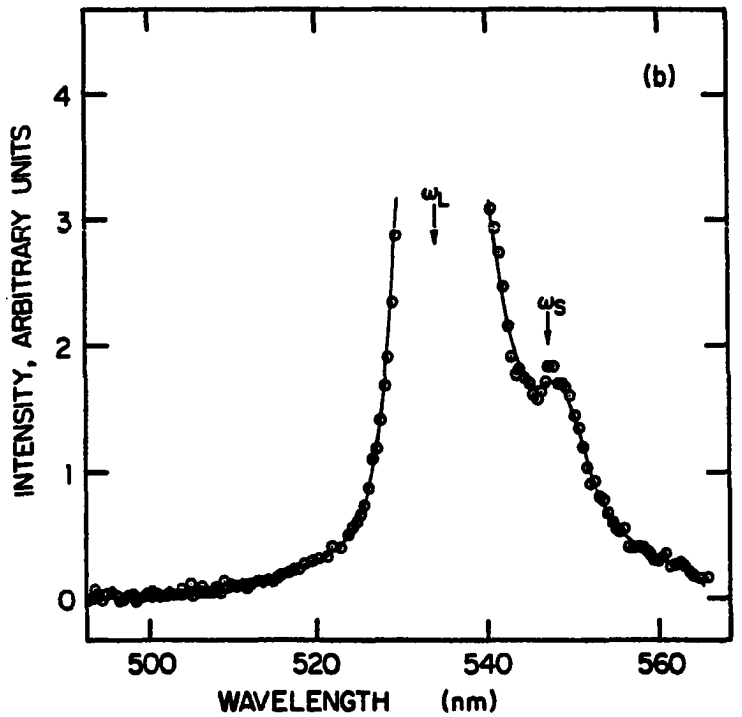
(b)
INTENSITY, ARBITRARY UNITS
0
1
2
3
4
ω_L
ω_S
500
520
540
560
WAVELENGTH (nm)

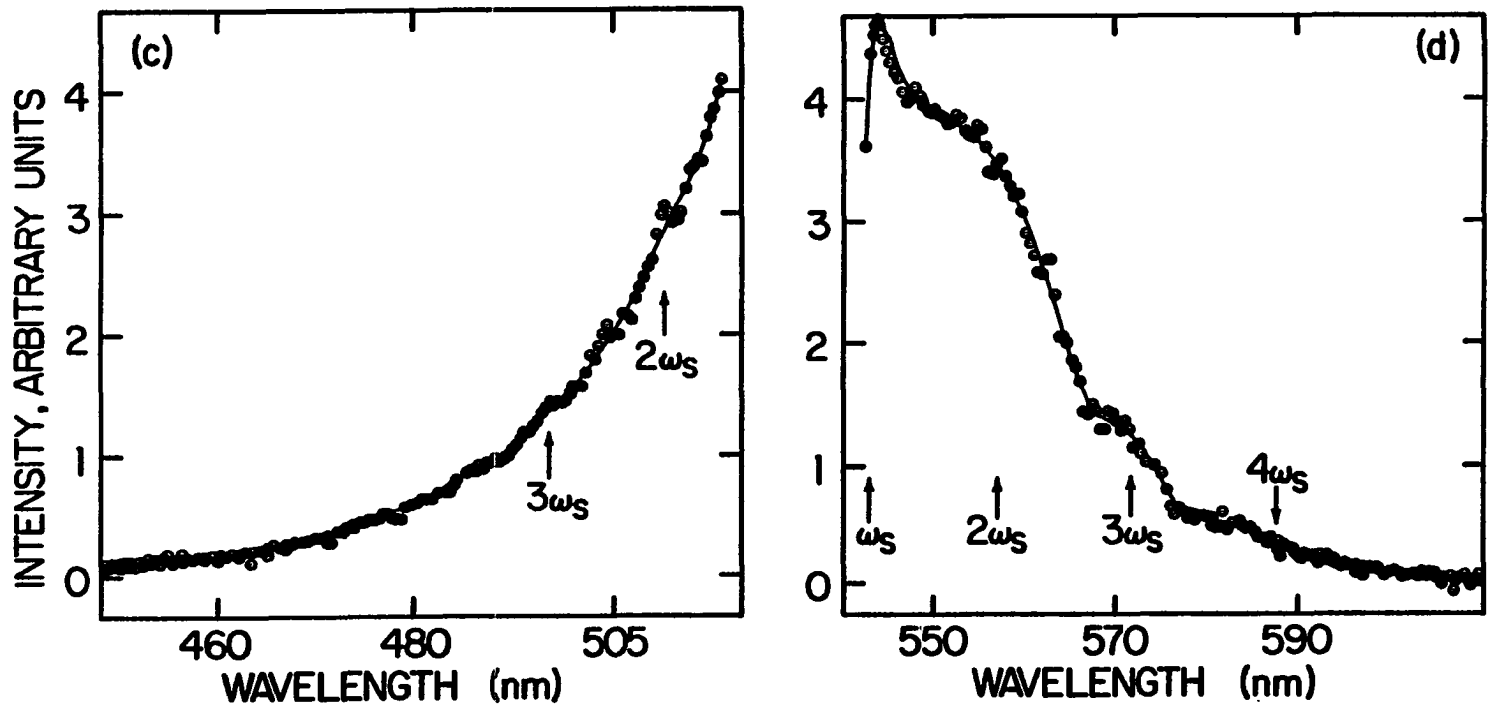

Figure 3-2. (Continued)

detectable anti-Stokes line at the expected first order anti-Stokes wavelength at 519 nm. Figures 3-2c and 3-2d show the anti-Stokes and Stokes side of the pump pulse at higher pump pulse intensities. Structure on the anti-Stokes side was less sharp than on the Stokes side. We never observed well-resolved anti-Stokes lines except for those laser shots when the photodiode monitors indicated either poor modelocking or poor pulse extraction in the electrooptic switch. In these atypical cases, a reasonably sharp first-order anti-Stokes line was detected at ~519 nm; higher order anti-Stokes lines were not observed. At the intensities used in our transient absorption experiments, the anti-Stokes continuum was structureless (see Figure 2-16).

These preliminary studies suggest that the primary broadening mechanisms in CCl_4 using 532 nm pulses are stimulated Raman scattering with self-phase modulation. Using equations 3.4 and 3.17 to estimate the contribution to broadening from self-phase modulation (SPM) for a 7 ps 532 nm pulse in a 20 cm cell, one finds $\Delta\omega \cong 2200\ cm^{-1}$ or broadening out to 476 nm on the anti-Stokes side. In addition to SPM broadening contribution to the 532 nm pulse, the Stokes and anti-Stokes lines can undergo similar SPM broadening (176) to fill out the continuum. This broadening can explain the lack of clearly resolvable structure on the anti-Stokes side of the spectrum by smearing out the lines causing an overlapping of intensities. Moreover, using a multimode laser and long cells, this broadening is enhanced significantly (218). With the strong focusing used in our apparatus, it is possible for the avalanche ionization mechanism to play a role. This also could explain

the lack of resolvable structure on the anti-Stokes side of the continuum since the avalanche ionization mechanism only contributes to the anti-Stokes side of the continuum (167, 187). The parametric four-wave mixing process believed to be operative for H_2O doesn't seem to be particularly relevant to our experimental conditions since Penzkofer's group (189) assiduously avoided self-focusing and used 1.06 μm pulses. Furthermore, under their conditions, using CCl_4 and other strong Raman scatters, they observed the onset of stimulated Raman activity prior to what they believed to be parametrically generated light (189).

Based on the literature concerning spectral broadening and the qualitative results from our laboratory, it is probable that the type of Raman emission observed from the continuum cell was Class II, since we were working with conditions encouraging self-focusing. One way to verify this would be to acquire a stigmatic spectrophotometer, record the spatial distribution of the emission lines across the surface of the cell, and calculate the off-angles as a function of wavelength. We do a calculation similar to this in a subsequent section of this chapter.

Considerations Involving the Continuum Optics

A cursory glance at the optical arrangement used in the transient absorption experiments (Figure 2-8, p. 58) reveals several lenses and other optical components. When one is using monochromatic light, the wavelength-dependent refractive index of the optical materials is not a major concern, but the introduction of continuum light into an arrangement using numerous optical components requires consideration

of the magnitude of the chromatic aberrations and the artifacts these aberrations can introduce into the experiment. These considerations acquire greater importance when one uses a continuum that has been generated via nonlinear techniques; these continua generally have an angular distribution of wavelengths (27, 167, 178, 189) due to the previously mentioned noncollinear phase-matching conditions.

To illustrate the effect of an angular distribution of light on a lens, consider a thin lens. A common way to study the effect of an optical element on a propagating ray of light is to use matrix algebra (219-221). For a thin lens and a single ray of light, we have in this formalism,

$$\begin{pmatrix} \alpha' \\ x' \end{pmatrix} = \begin{pmatrix} 1 & -1/f \\ 0 & 1 \end{pmatrix} \begin{pmatrix} \alpha \\ x \end{pmatrix} \tag{3.24a}$$

where f is the focal length of the lens (the reciprocal, 1/f, is defined as the power of the lens in units of diopters, m^{-1}), α and α' are the initial and final angles of the ray with respect to the optic axis, and x and x' are the heights above the optic axis. Immediately after passing through the lens,

$$\alpha' = \alpha - x/f \tag{3.24b}$$

$$x' = x \quad . \tag{3.24c}$$

Translation of the exciting ray is expressed via

$$\begin{pmatrix} \alpha'' \\ x'' \end{pmatrix} = \begin{pmatrix} 1 & 0 \\ t' & 1 \end{pmatrix} \begin{pmatrix} \alpha - x/f \\ x \end{pmatrix} , \tag{3.25}$$

where t' is the distance along the optic axis divided by the medium index of refraction. Then

$$\alpha'' = \alpha - x/f \tag{3.26a}$$

$$x'' = t'(\alpha - x/f) + x \quad . \tag{3.26b}$$

To determine the influence of α on the focal point of the lens, let $x'' = 0$ (ray crosses optic axis), so that

$$t' = \frac{-x}{\alpha - x/f} = \frac{xf}{x - \alpha f} \quad . \tag{3.27}$$

For a typical lens with a focal length of 15 cm and the incident light at ~1 cm above the optic axis, the variation of f with α is given in Table 3-1.

Table 3-1. Variation of focal point with incident angle (thin lens approximation)

α(mrad)	Focal point (cm)
0.00	15.00
1.00	15.22
5.00	16.22
10.00	17.65
20.00	21.43

The focal length of the thin lens thus shows a significant variation over relatively minor changes in the angle. Since the light emitted from a continuum is angularly dispersed, awareness of this property of the focusing lens and its effect on the overlap of the

pump and probe regions in the sample is prerequisite to proper evaluation of the spectra.

Prismatic effects

One common effect observed when polychromatic light is incident on an interface between two regions of different indices of refraction is the prism effect. Within our optical arrangement, the glass interface between the liquid CCl_4 and the air offers the possibility of prism-like dispersion of the continuum light. Using Snell's law and the tabulated refractive indices for CCl_4 (222), Table 3-2 gives the refraction of three wavelengths in the visible for a sequence of incident angles. From the table, one can see that the blue wavelengths are not dispersed substantially more than the red wavelengths at the CCl_4/air interface even at relatively large angles of incidence (200 milliradians). Several groups have reported distributions of 50-100 milliradians over the visible wavelengths for continuum generated light (167, 178, 189). For rays of continuum light collinear to the laser or even with a slight divergence from the axis, the prismatic effect of the continuum cell cannot disperse the wavelength components of the reported magnitude. To obtain such dispersion, it seems likely that the wavelengths of the continuum are generated with a preferred angular distribution. This is shown to be consistent with the requirement for noncollinear phase-matching in the stimulated Raman generated continuum (vide infra).

Table 3-2. Prismatic effect: Exit angles, θ_f, for three visible wavelengths at a CCl_4/air interface for various incident angles θ_i

θ_i(mrad)	434 nm θ_f(mrad)	486 nm θ_f(mrad)	656 nm θ_f(mrad)	$\theta_f^{434} - \theta_f^{656}$ (mrad)
5.00	7.365	7.338	7.290	.075
10.00	14.73	14.68	14.58	.150
20.00	29.46	29.35	29.16	.300
50.00	73.61	73.42	72.93	.680
100.00	147.60	146.50	145.50	2.100
200.00	297.00	291.60	289.60	7.400

Chromatic aberration

The principal aberration caused by the frequency-dependent refractive index is a color dependent focal length. Figure 3-3a shows a typical variation in focal length for a biconvex lens. In this example, the lens has an undercorrected longitudinal chromatic aberration, meaning that the blue wavelengths are focusing closer to the exit surface of the lens than the red ones. With a lens such as the one shown in the figure and a focal length of 50 cm, the difference between the focal lengths of a blue and red wavelength can be ~1 cm.

If one is using a sample cell 5 mm long, uniform focusing of the continuum is not possible. To minimize color dependent focal lengths in the probe path, our optical set up (Figure 2-8) utilized only achromatic lenses in the probe path beyond the continuum cell. An achromatic lens is generally constructed from two thin lenses of differing refractive index in optical contact and are designed so that the focal points of the blue Fraunhofer line (F) at 4861 Å and the red

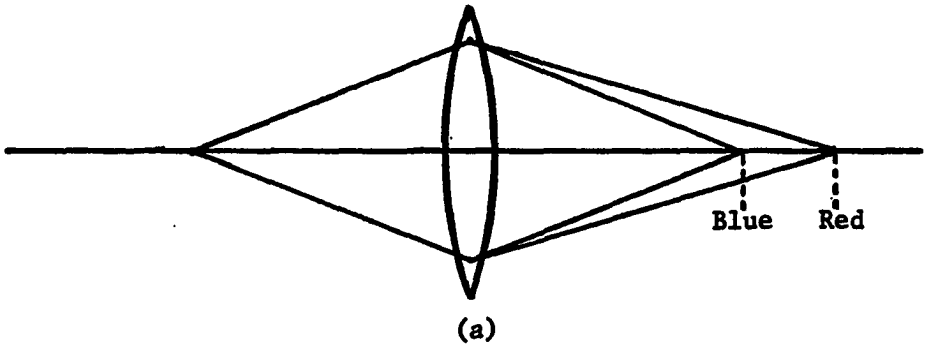

(a)

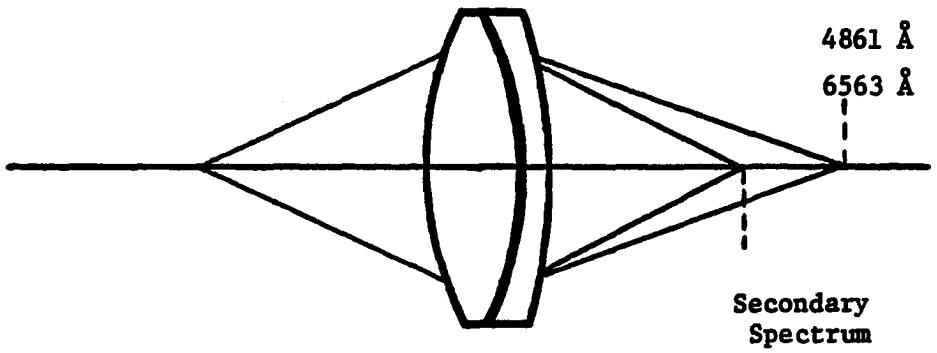

(b)

Figure 3-3. Chromatic aberrations
(a) Chromatic aberration of a positive convex lens;
(b) Secondary spectrum of an achromatic doublet

Fraunhofer line (C) at 6563 Å coincide (Figure 3-3b). The focal points for the wavelengths that lie between these two specified wavelengths cannot coincide with that of the red and blue lines, but instead focus over a range of points slightly before it. This distribution in focal lengths is called the secondary spectrum of the achromatic lens, and it is necessary to estimate this spread in focal points of the secondary spectrum. An estimate is possible by starting with the thin lens equation (219),

$$\frac{1}{f} = (n_\lambda - 1)\left[\frac{1}{R_1} - \frac{1}{R_2}\right] = (n_\lambda - 1)\rho \quad , \tag{3.28}$$

where f is the focal length of the lens, n_λ is the refractive index at wavelength λ, and R_1 and R_2 are the radii of curvature for the front and rear surfaces of the lens, respectively, using the standard notations of geometrical optics (219-221). For a single lens, the relationship between the focal lengths of two different wavelengths is

$$f_{\lambda_2} = \frac{(n_1 - 1)}{(n_2 - 1)} f_{\lambda_1} \quad , \tag{3.29}$$

where n_1 and n_2 are the refractive indices for wavelengths λ_1 and λ_2, respectively. For two contacted thin elements with indices of refraction n_1 and n_1', the focal length or power of the lens system can be expressed, as

$$\frac{1}{f} = \frac{1}{f_{1_\lambda}} + \frac{1}{f'_{1_\lambda}} = (n_1 - 1)\rho_1 + (n_1' - 1)\rho_1' \quad . \tag{3.30}$$

Using equations 3.29 and 3.30, the expression for a thin lens combination becomes

$$\frac{1}{f_{\lambda_2}} = \frac{n_2' - 1}{n_1' - 1}\frac{1}{f_{\lambda_1}} + \frac{n_2 - 1}{n_1 - 1}\frac{1}{f_{\lambda_1}} \quad . \tag{3.31}$$

With a given focal length, f_{λ_1}, and an accurate dispersion curve for the glasses used in the thin lens combination, one can calculate the focal length, f_{λ_2}, using the above equation.

In their text on optics, Hecht and Zajac (219, p. 190) discuss how to construct an achromat with a focal length of 50 cm at 5875 Å out of BK1, a crown glass, and F2, a flint glass. Using the results of their calculation, the power of the crown glass should be 4.685 diopters and -2.685 diopters for the flint to obtain the desired focal length at the specified wavelength (note, using equation 3.30, that $(4.685 - 2.685)^{-1} = 0.50$ m is the desired focal length). We will use this achromat to estimate a representative secondary spectrum. Table 3-3 gives the focal lengths for various visible wavelengths calculated from equation 3.31. The wavelength dependent indices of refraction for BK1 and F2 glasses came from Hecht and Zajac (219), Schott Glass Company sales literature, or extrapolated from the known data points. As can be seen from the table, over the visible, the focal point does not change significantly--by approximately 0.2 mm from 650-400 nm. One can infer from this calculation that the color-dependent variation in focal length that characterizes the secondary spectrum is negligible when one is using a sample cell $\geq$ 2 mm long.

SRS wavelength-dependent emission angles

Since stimulated anti-Stokes Raman scattering is often accompanied by an angular distribution of the radiation and, from the experiments

Table 3-3. Secondary spectrum of a 50 cm achromat composed of BK1-F2 glass

λ(Å)	n_1(BK1)	n_2(F2)	Focal length (cm)
6562.8	1.50763	1.6150	50.02
6000.0	1.50964	1.6191	50.00
5875.6	1.51009	1.62004	50.00
5400.0	1.51270	1.6257	50.01
4861.3	1.51566	1.63208	50.02
4358.4	1.51998	1.64202	50.11
4046.6	1.52355	1.65063	50.22

mentioned earlier, Stokes and anti-Stokes emission were present in our continuum, an estimate of the approximate magnitude of off-axis angles is necessary to evaluate the contribution of this effect to the transverse components of the continuum light. To accurately determine the angles, one needs to know the frequency dispersion of CCl_4 very accurately. Hellwarth (223) has provided a Sellmeier formula for CCl_4 that is accurate to 5 parts in 10^4 for wavelengths as short as 400 nm. Expressing the refractive index at λ(nm) as

$$n_\lambda^2 = a_1 + a_2(1 - \lambda_v^2/\lambda^2)^{-1} \qquad (3.32)$$

with $a_1 = 2.040$, $a_2 = 0.0562$, and λ_v(nm) = 342, one can determine the refractive index of CCl_4 at 23°C. Table 3-4 gives the refractive index for 8 orders of anti-Stokes and 6 orders of Stokes scattering for the 460 cm^{-1} Raman-active a_1 mode for CCl_4.

We have considered in previous sections three different mechanisms

Table 3-4. Index of refraction and k vector for Stokes and anti-Stokes wavelengths in CCl_4

n	λ(nm)	n^a	$k \times 10^{-5}$ (cm^{-1})
8	444.9	1.47560	2.08394
7	454.2	1.47302	2.03770
6	463.9	1.47075	1.99203
5	474.0	1.46875	1.94693
4	484.6	1.46696	1.90202
3	495.6	1.46536	1.85778
2	507.2	1.46392	1.81350
1	519.3	1.46262	1.76967
0	532.0	1.46143	1.72602
-1	545.3	1.46036	1.68269
-2	559.4	1.45936	1.63916
-3	574.2	1.45846	1.59592
-4	589.7	1.45763	1.55309
-5	606.2	1.45686	1.51002
-6	623.6	1.45615	1.46717

[a]Calculated from equation 3.32.

for the generation of anti-Stokes lines in our continuum--four photon parametric generation and the two classes of stimulated Raman. Although Class II SRS is the most likely component in our continuum under our experimental conditions, for completeness we have compared the estimated angles of emission for the first 6 anti-Stokes lines in each of the three mechanisms in Table 3-5. The angles for Class I radiation were calculated from the volume phase matching conditions derived in Chiao and Stoicheff's paper on the angular emission from calcite (209); for Class II, from Shimoda's work on Raman emission from filaments (211); and for parametric generation, from equation 3.23.

Table 3-5 shows that if any of these mechanisms are operative, the

angular dispersion introduced is severe enough to cause serious focusing and overlap errors. In comparison to the primatic effect or the focusing error inherent in the achromats, this contribution is by far the most deleterious to uniform focusing of the blue continuum probe pulses in the sample cell.

Table 3-5. Emission angles for noncollinear phase matched anti-Stokes scattering from a 532 nm excitation pulse

n	λ(nm)	Class I[a] (mrad)	Class II[b] (mrad)	Parametric[c] (mrad)
1	519.3	13.28	19.02	13.27
2	507.2	24.22	30.08	18.01
3	495.6	37.28	54.61	28.74
4	484.6	46.82	62.21	38.09
5	474.0	59.53	73.51	46.94
6	463.9	71.03	84.01	55.21

[a]Calculated from Chiao and Stoicheff (209).

[b]Calculated from equation 3.21, based on Shimoda (211).

[c]Calculated from equation 3.23.

Experimental Evaluation of Transverse Effects on Transient Absorptions

To ascertain whether the prismatic effect and the residual chromatic aberrations of the secondary spectrum were as negligible as the foregoing calculations seem to indicate, a continuum generated by a tungsten lamp was directed through the continuum optics and observed. The broadband emission from a tungsten lamp has no preferred direction for specific wavelengths as does the laser generated continuum. The tungsten

emission was passed through a diffuser and, as needed, neutral optical density filters, then focused onto the mirror which is used to direct the 532 nm pump pulse into the continuum cell (M_2, Figure 2-8). This allowed the tungsten light to pass through all the optics--lens, continuum cell, achromats and sample cell--that would be encountered by the laser-generated continuum in a transient absorption experiment. If the CCl_4 cell introduced a prism effect and/or significant focusing effects accumulated as the light travelled through the optical path, one would expect to see some wavelength dependent effects on the vidicon. As discussed in Chapter 2 and in Appendix C, the I and I_0 probe beams are imaged onto two spatially different regions on the vidicon grid. The acquisition of the spectral information is governed by two strobe pulses synchronized to allow storage of the video signal produced by the continuum images, I and I_0, when the electron beam is sampling the proper diodes. Consider Figure 3-4a. Two identical images are positioned on the vidicon grid. The left hand image has 4 vertical dashed lines (a-d) which represent an arbitrary sequence of I strobe positions; when the strobe is set in any position, say b, the video signal for the I image is derived from that region of the spectral image. Obviously, varying the strobe's position from a through d changes the spatial region from which the video signal is acquired.

Figure 3-5a through d show the I (circles) and I_0 (triangles) spectra for the tungsten continuum. For each of these spectra, the I_0 strobe position (e) was kept stationary while the I strobe was varied over four different positions approximately ~0.17 mm apart on the

Figure 3-4. Spatial positions of I and I_0 strobes on the signal half of the vidicon. In both (a) and (b), the solid lines indicate the area on the vidicon grid where the continuum beams are imaged; the dotted lines a-e are discrete spatial positions of strobes 1 and 2

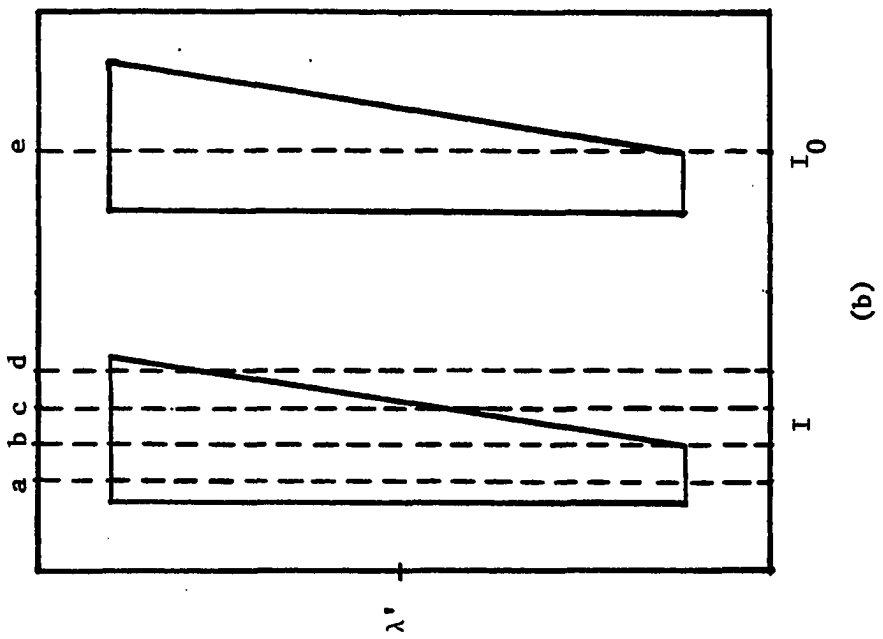
e
a b c d
I_0
I
(b)
λ'

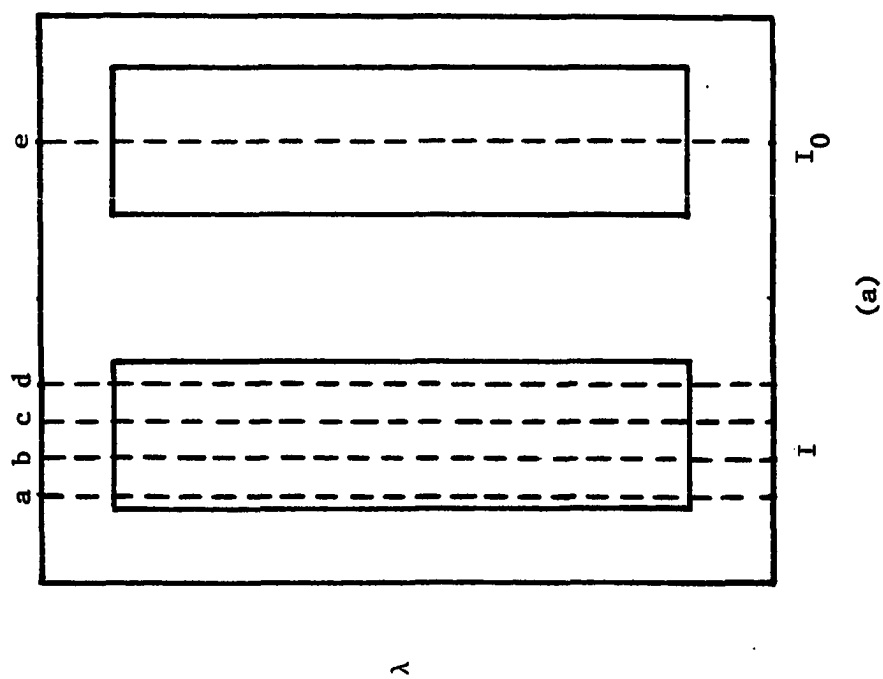
e
a b c d
I_0
I
(a)
λ

Figure 3-5. Spectral distribution and variation in optical density for continuum generated by a tungsten lamp for different strobe 1 positions (I continuum)

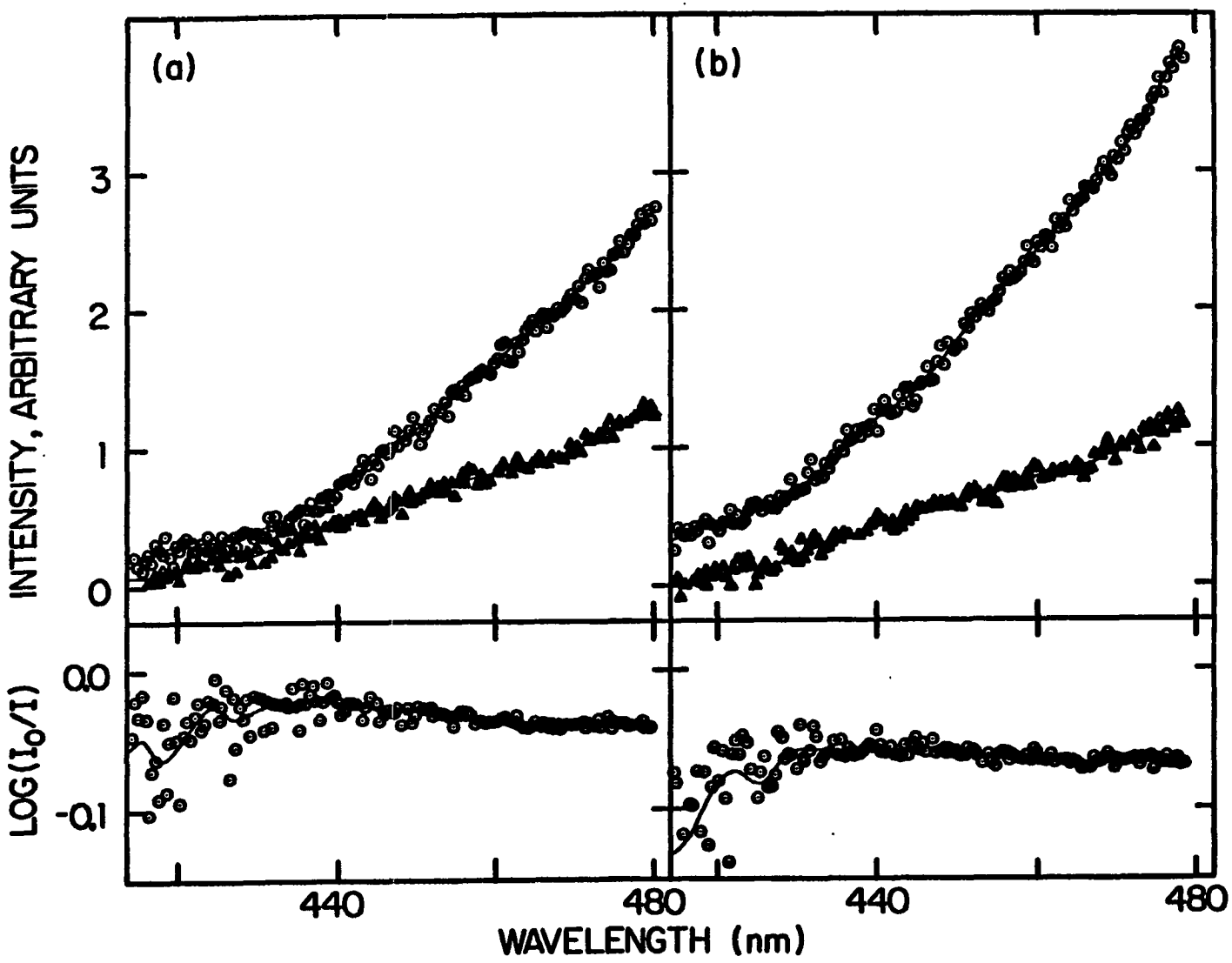
(a)
(b)
INTENSITY, ARBITRARY UNITS
3
2
1
0
LOG(I0/I)
0.0
-0.1
440
480
440
480
WAVELENGTH (nm)

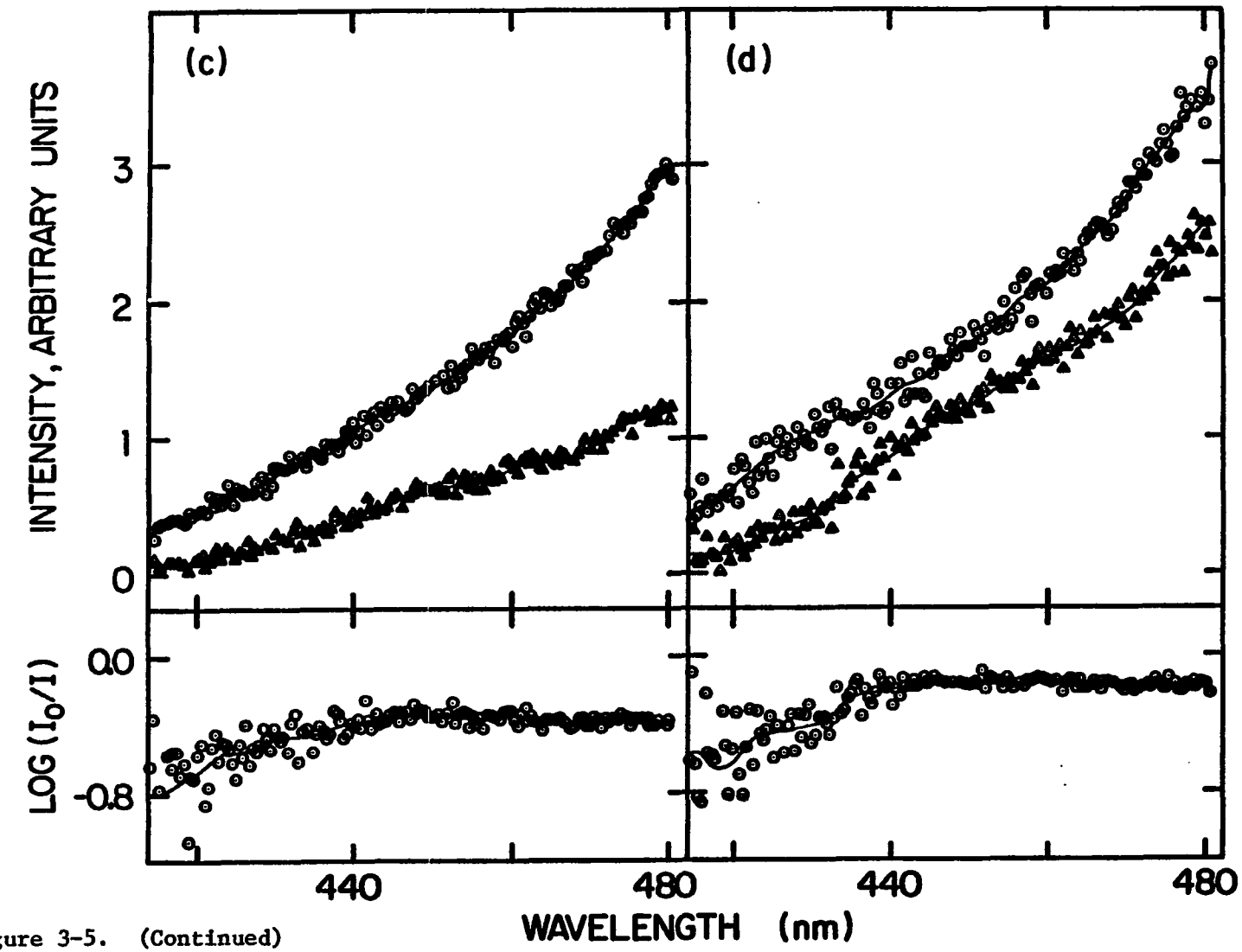

Figure 3-5. (Continued)

vidicon across the 1 mm wide I image. Below each set of spectra is the optical density plot, I/I_0, for that particular set of spectra. Except for the blue portion of the spectra (420 nm) where the weak intensity of the tungsten continuum and the averaging routine in the computer software combined to cause some scatter, the OD plots are fairly flat across the wavelengths shown. This implies that the variations in intensity as a function of wavelength for different spatial regions of the image on the vidicon grid are identical for the I and I_0 spectra. In contrast, a similar examination of the spatial dependence of the spectral intensity of the laser-generated continuum images reveals considerable asymmetry with respect to wavelength and intensity. The OD plots of Figure 3-6a-d show substantial changes in the optical density plots (log I/I_0) over the 420-480 nm range shown. Of the four continua shown, the optimum continuum distribution for transient absorption experiments would be Figure 3-6b, where the OD plot is almost constant over the region of interest, in analogy to the OD plots for the tungsten continuum. The variation of continuum intensity with the spatial position of the image can be qualitatively explained using Figure 3-4b. The images I and I_0 have been drawn to display a flared distribution of light intensity as a function of wavelength; analogous spectral distributions have been photographed by Alfano and Shapiro (178) for picosecond continua excited at 532nm in BK7 silicate glass. Consider some arbitrary wavelength, λ'. As the I strobe is moved transversely across the I image (positions a-d), the ratio $I(\lambda')/I_0(\lambda')$ will change significantly if the I_0 strobe is held

Figure 3-6. Spectral distribution and variation in optical density for continuum generated by the 532 nm picosecond pulse in CCl_4 for different strobe 1 positions (I continuum). Each pair of spectra was generated by a single laser shot

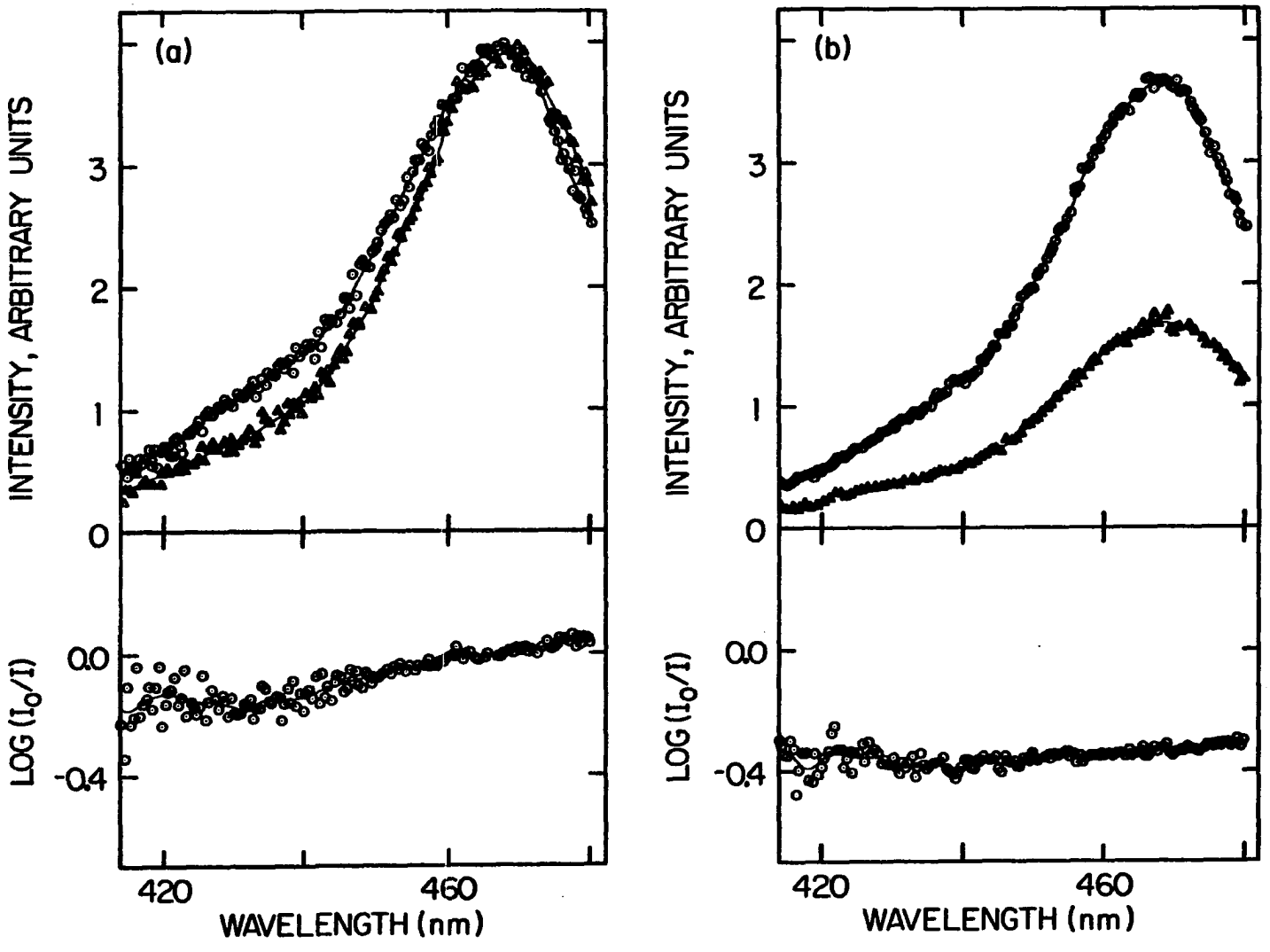
(a)
(b)
INTENSITY, ARBITRARY UNITS
LOG (I_0/I)
3
2
1
0
0.0
-0.4
420
460
WAVELENGTH (nm)

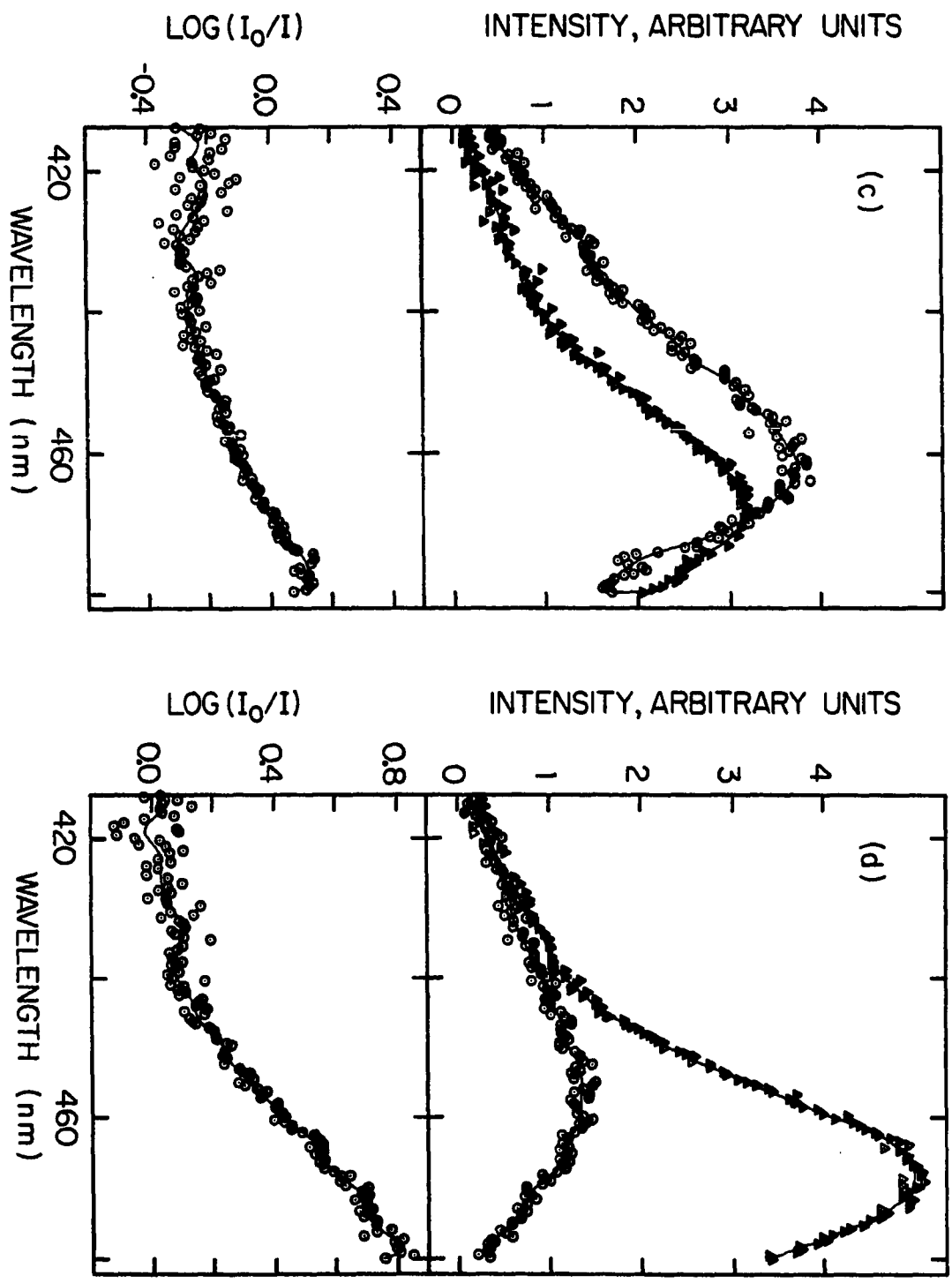

Figure 3-6. (Continued)

stationary. Similar fluctuations occur over the entire continuum spectrum, and can result in OD plots such as those shown in Figure 3-6.

The importance of the correct sampling geometry when obtaining transient absorption spectra can be illustrated by examining the effects of sampling geometry on known transient absorption spectra. One of the better studied transient absorption spectra is the $T_1 \rightarrow T_n$ spectrum of acridine in both the picosecond (184, 224) and the long-time regime (225). In Figure 3-7, we show the spectral distribution of the I and I_0 beams in the absence of the acridine sample for two different I strobe positions. The effect of sampling two spatially different probe images on the transient absorption spectra is illustrated in Figure 3-8; (a) and (b) correspond to spectra taken when the I strobe positions were the ones shown in 3-7a and 3-7b, respectively. Both spectra were taken at ~122 ps after excitation by a 354 nm pulse. The long-time transient absorption spectrum obtained by Land (225) with long-time pulse radiolysis techniques is superimposed for comparison (dot-dashed line) on the spectrum obtained in our laboratory in Figure 3-8a. The optical density background, obtained by blocking the 354 nm pulse, is shown for each spectrum by the dashed line. There are noticeable differences between the two transient absorptions: Figure 3-8a shows greater optical density for longer wavelengths (>450 nm), less optical density for shorter ones (<420 nm) and has a different absorption maximum than Figure 3-8b. These variations in spectra can significantly complicate the interpretation of time resolved absorption spectra, especially if the absorption is a composite of more than one

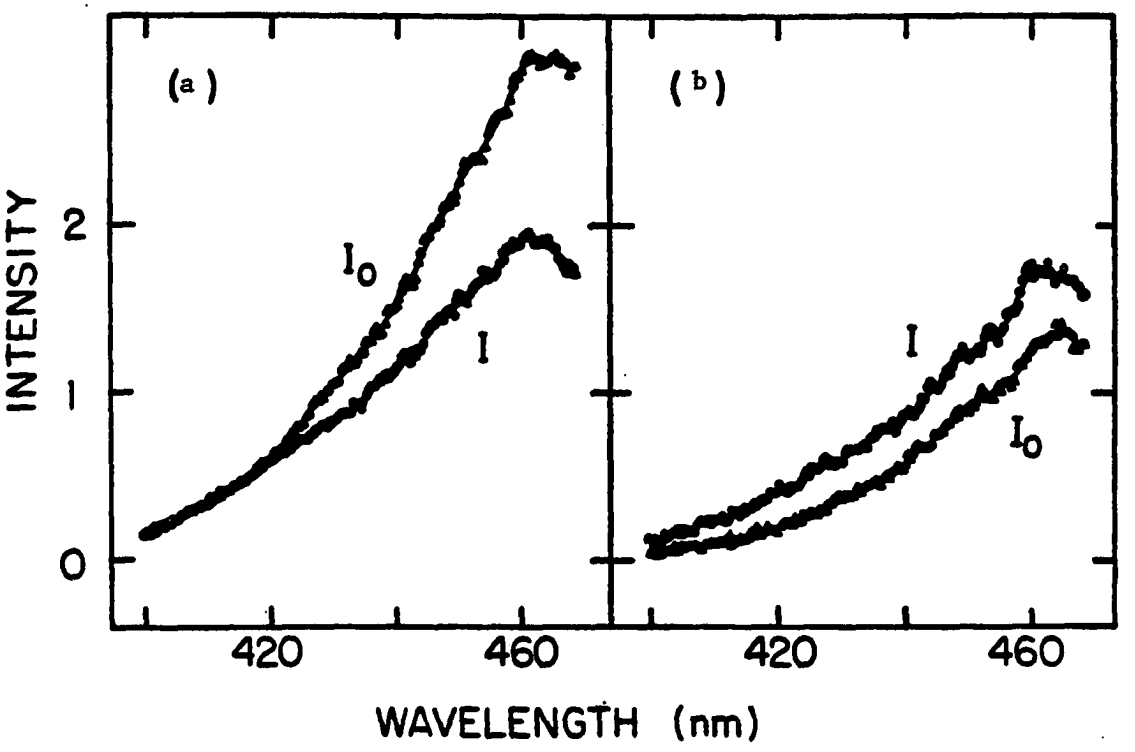

Figure 3-7. I and I_0 continuum spectra for 2 different I sampling areas ~0.35 mm apart

Figure 3-8. Transient absorption spectra of acridine in n-hexane 122 ps after excitation. I sampling areas in (a) and (b) are identical to those in Figs. 3-7a and b, while I_0 sampling areas are adjusted for approximately level baselines (dashed lines). Dot-dashed curve in (a) is triplet-triplet spectrum of acridine from pulse radiolysis (ref. 225)

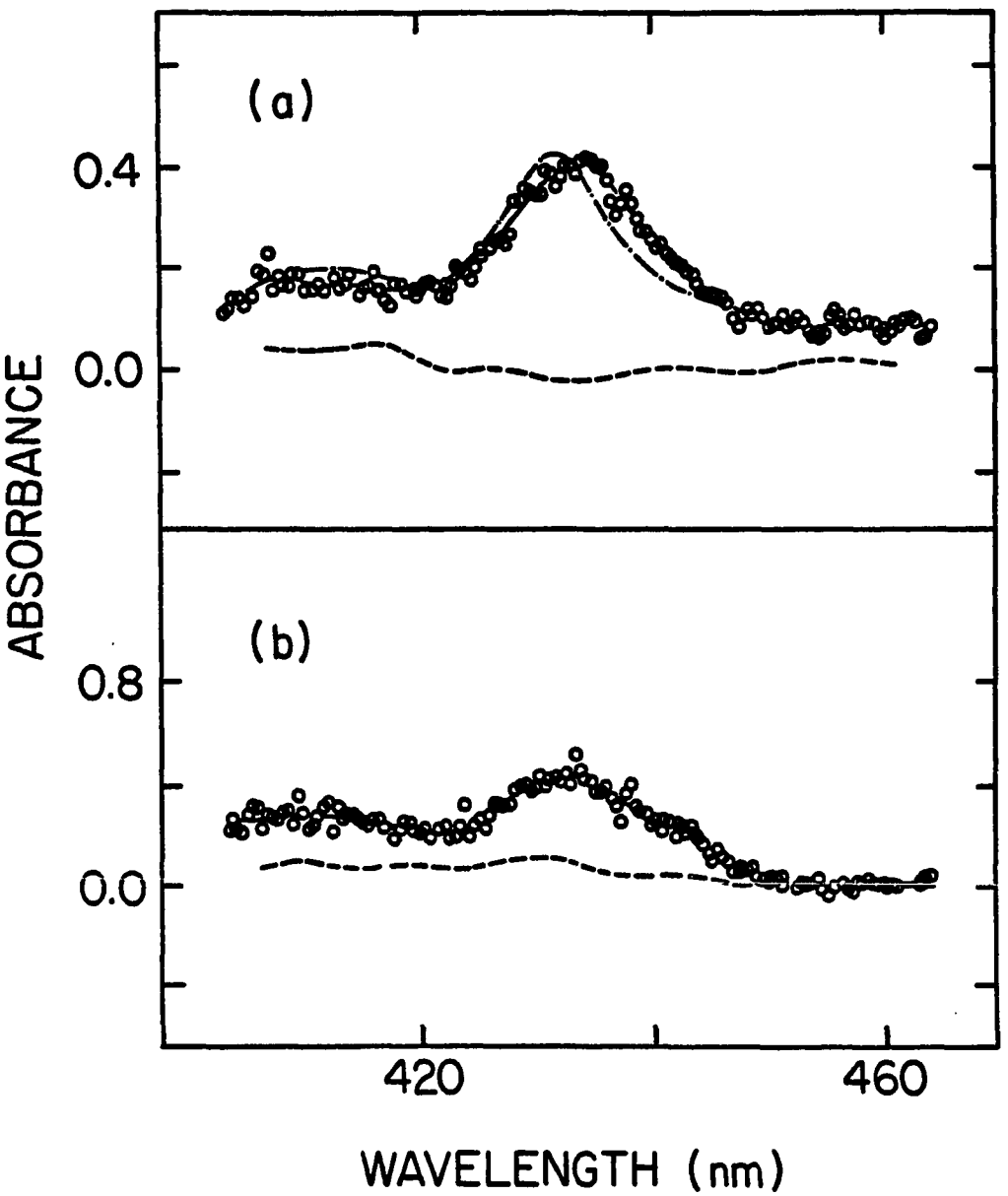
(a)
0.4
0.0
(b)
0.8
0.0
ABSORBANCE
420
460
WAVELENGTH (nm)

electronic transition.

Summary

The foregoing sections have demonstrated that when one is conducting picosecond transient absorption experiments with a laser-generated continuum, the transverse nature of the created continuum can be the source of serious artifacts. These artifacts can be especially deceptive if the purpose of the experiment is to elucidate the spectral time evolution of the transient absorption, or if there is more than one absorbing species in the wavelength region being probed. One method to correct this problem is to pass the continuum probe through an apertured (~1 mm) ground glass diffuser plate to homogenize the continuum spatially (50, 51). Furthermore, the continuum cell need not be 20 cm long; we have conducted several transient absorption experiments using a 5 cm continuum cell filled with CCl_4, although the intensity from the 20 cm cell is about 2.5 times stronger. Since a diffuser reduces the continuum intensity by ~2-3 orders of magnitude, a more sensitive vidicon detector would be required. If the vidicon-based detection system is to be retained, a silicon intensified target would probably be necessary to observe the continuum light at substantial wavenumbers away from the pump source. From the perspective that Nd:glass-continuum systems are the only ones capable at the present time of easily performing broadband transient absorption studies, and that there is significant chemical dynamical information to be obtained from such experiments, the investment in a more sensitive detection equipment is certainly warranted.

CHAPTER 4

Introduction

The understanding of photodissociation dynamics in large polyatomics has been substantially increased in the past decade by a wide variety of time-resolved experiments on aryl halides (150, 170, 226-228), and also by theoretical treatments of photodissociation on multidimensional potential energy surfaces (229-231).

The introduction of a halogen, especially iodine, into an organic molecule adds a photodissociation channel involving the cleavage of the weak C-X bond to the available photophysical processes possible following visible and near-UV excitation. Moreover, the halogen atom accelerates intersystem crossing (ISC) due to the enhancement of the spin orbital coupling Hamiltonian, which has a Z^4 dependence (Z = heavy-atom atomic number). This heavy atom effect and its influence on photochemistry have been discussed by McGlynn et al. (232).

One of the earliest discussions on the photodissociation of aryl halides was that of Durie et al. (233) who observed that the $S_0 \rightarrow S_1$ UV absorption of iodobenzene vapor was a structureless continuum, more analogous to the spectra observed in alkyl iodides than the structured absorption shown by substituted benzenes. The structureless absorption in alkyl halides had been attributed to lifetime broadening by an extremely short-lived dissociative excited state. Similarly, Durie suggested that the observed spectral anomaly in iodobenzene was due to a predissociating state. Vapor phase studies on the monohalogen substituted napthalenes showed similar broadening in the 1- and

2-iodonapthalenes in the UV absorption spectra of the first and second excited states (234).

Using molecular beam techniques, R. Bershon's group at Columbia examined the photodissociation lifetimes, as inferred from the anisotropies in the photofragment distributions, in several haloaromatics and alkyl halides (226). The angular distributions of the photofragments depend on the lifetime of the optically excited state and the direction of its transition dipole moment. Mathematically, the angular distribution can be expressed as (226, 231):

$$I(\theta) = \frac{1}{4\pi} [1 + \beta P_2(\cos \theta)] \qquad (4.1)$$

where $P_2(\cos \theta)$ is the second Legendre polynomial, θ is the angle between the direction of the detector and the polarization of the exciting light, and β is the anisotropy parameter. If fragmentation occurs fast enough so that the molecule has no time to rotate, anisotropy is introduced into the angular distribution. Rapid dissociations result in large β values. Contrastingly, in long-lived species, the excited molecule can undergo several rotations before dissociating, resulting in a more uniform distribution of the fragments and hence smaller anisotropy parameters. The absolute lifetimes can only be determined if the lifetime, τ, is not too short or long compared to $(I/kT)^{\frac{1}{2}}$, where I is the principal moment of inertia. Bersohn was able to assign lifetimes for 4 molecules: methyl iodide, 0.07 ps; iodobenzene, 0.5 ps; α-iodonapthalene, 0.9 ps; and 4-iodobiphenyl, 0.6 ps. Experimental anisotropies of the analogous bromides were found to be smaller, and Bersohn estimated their lifetimes

to be approximately 2 orders of magnitude longer. From these lifetimes, Dzvonik et al. (226) concluded that the aryl iodides and bromide analogs undergo dissociation by a distinctly different mechanism than that followed in alkyl iodides.

The extremely short lifetime found for the methyl iodide, ≤ 0.07 ps, is approximately the time it would take for two particles to separate on a repulsive potential. Classically, the time, τ_d, for this separation can be found from

$$\tau_d \sim \left(\frac{2\mu Q}{\bar{\alpha}}\right)^{\frac{1}{2}} \tag{4.2}$$

where μ is the reduced mass of the fragments along the reaction coordinate Q and $\bar{\alpha}$ is the linearized slope of the repulsive potential. Using the reduced mass for methyl and iodine fragments, a Q value of 5 Å, and a linearized slope $\bar{\alpha} \simeq 2.7 \times 10^{-9}$ J/m (estimated from the slope of repulsive state, $^1\pi_{1_u}$ of I_2), one finds $\tau_d \simeq 0.095$ ps. From the foregoing, Bersohn concluded that methyl iodide is directly dissociated by photoexcitation into a repulsive state. The aryl iodides with slightly longer lifetimes, $\lesssim 1$ ps, are believed to be predissociated by spin-orbital coupling from the $S_2(\pi\pi^*)$ state, in which excitation is delocalized primarily within the aromatic moiety, to a repulsive triplet α^* state localized on the R-X bond. Dissociation after internal conversion to S_1 or S_0 would involve a time consuming (> 1 ps) Franck-Condon redistribution of the excitation energy into IC-promoting high frequency CH modes, and then subsequent accumulation of sufficient energy into the C-X bond to cleave it--a process not temporally

consistent with those observed in aryl iodides. For the aryl bromides which exist ~100 times longer than the iodides, the magnitude of the spin-orbital coupling matrix is ~4 times smaller than the iodides, and hence their ISC processes are slower. According to Bersohn and co-workers, dissociation in the bromides is preceded by IC to lower singlets and then by ISC to a dissociative triplet state (226).

Photodissociation processes of molecules in the condensed phase are even more poorly understood than those in the vapor phase. The introduction of a solvent bath which can dissipate excitation energy can alter the dynamics of the reaction considerably. A salient example of solvent effect on photodissociation dynamics is seen in 1-iodo-napthalene. In the gas phase, the experimental evidence suggests that excitation to S_2 directly predissociates the molecule; yet, in methyl cyclohexane, Levy et al. (235) observe no wavelength dependence in photodissociation yields for excitation into either the S_1 (313 nm) or S_2 (254 nm) electronic states.

We have performed time-resolved fluorescence and triplet-triplet transient absorption experiments on 9- and 2-iodoanthracene in room temperature cyclohexane solutions (150, 170). Below we describe the procedures and results of the triplet-triplet absorption (TTA) experiments. These results on the early time evolution of the triplet state, combined with previous fluorescence studies (150) and recently obtained wavelength-dependence photoproduct quantum yields, are used to revise a previously proposed scheme (170) for haloanthracene photodissociation.

Procedure and Results

Picosecond studies

In Figure 4-1, we show the optically allowed energy levels for CI single-excitation π states as calculated by Hummel and Ruedenberg (236). To the right of the levels, a bracket delineates the estimated range of dissociation energies for the iodide bond in haloanthracenes, based on values derived from electron impact or pyrolytic studies on iodobenzene and alkyl iodides (237). Recent variable temperature pulse radiolysis studies (238) on iodonapthalene and iodobiphenyl have estimated the C-I bond dissociation energies of these molecules to be ~65 kcal/mole (~22730 cm^{-1}).

The pump and probe scheme utilized in our TTA experiments to elucidate the nonradiative pathways is illustrated in Figure 4-2. In this figure, Pariser notation is used to denote the symmetry of the electronic states. The 354 nm third harmonic was used to excite the aryl halides to their first excited state S_1. Because of differences in S_1 origins, a 354 nm photon deposits ~3,800 cm^{-1} and 3,000 cm^{-1} of excess vibronic energy into the 9- and 2-iodoanthracene singlet manifolds, respectively. After the continuum was generated, it was used to probe the time-dependent spectral changes throughout the 400-500 nm wavelength region. With the apparatus described in Chapter 2, the transient absorption spectra were obtained for probe delays over a time period extending from ~1-12.6 to 291.5 ps with zero time corresponding to maximum coincidence with the excitation pulse.

Due to a mean group velocity dispersion of -0.13 nm^{-1} over the

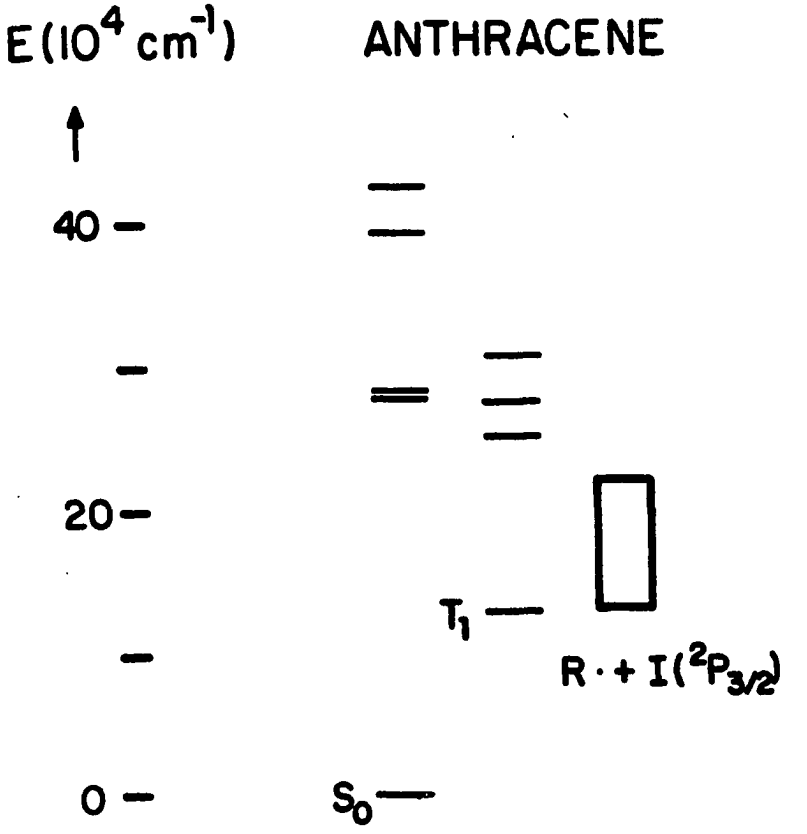

Figure 4-1. Optically active singlet states and triplets states of anthracene from electronic structure calculation in ref. 236. Probable dissociation energies of iodoanthracenes into $R\cdot + I(^2P_{3/2})$ are bounded by the rectangle

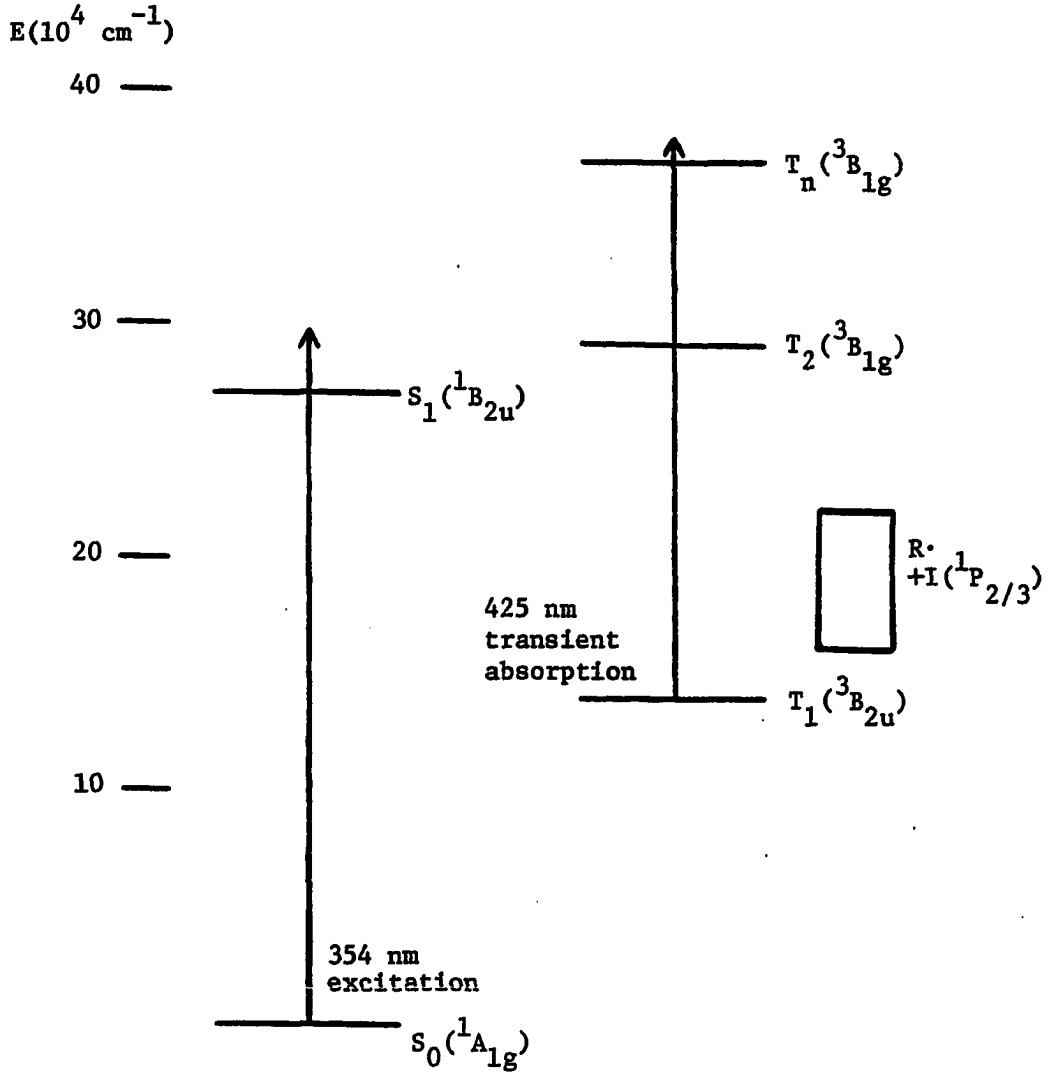

Figure 4-2. Pump and probe scheme used for iodoanthracene triplet-triplet transient absorption study

range of 420-532 nm (see Table 3-4 for an estimate of $dn/d\lambda$), for the blue continuum in CCl_4 the blue wavelengths will be delayed with respect to the longer wavelengths (assuming simultaneous production). The reported delays are specified at 432 nm, the longtime transient absorption maximum of 2-iodoanthracene in cyclohexane.

The region of maximum $T_n \leftarrow T_1$ absorption for both iodoanthracenes is 420-440 nm; this is the same spectral region for the $T_n \leftarrow T_n$ transient absorption identified in anthracene (239), the bromoanthracenes (225), and several other anthracene analogs (224, 240). In anthracene, the upper triplet state has been identified as the in-plane polarized $^3B_{1g}^-$ state, the transition to which has an oscillator strength of 0.25 (241).

Subnanosecond transient spectroscopy on anthracene in cyclohexane solutions (239) has established that the strongest $S_1 \rightarrow S_n$ absorption occurs around 600 nm, and the analogous transition to higher singlets in iodoanthracenes is expected to be in the same red wavelength region. Consequently, substantial singlet state absorption should not contribute to the spectral changes in the 410-480 nm region.

Representative transient absorption spectra for 2-iodoanthracenes in cyclohexane at 2 different delays is shown in Figure 4-3. For each time delay, several spectra were taken after the sample had been excited by the 354 nm excitation; several other shots were taken with the excitation beam blocked. These latter spectra constituted background spectra that were averaged and subtracted from the former spectra to derive the actual optical density changes for that time delay (see Figure 2-16).

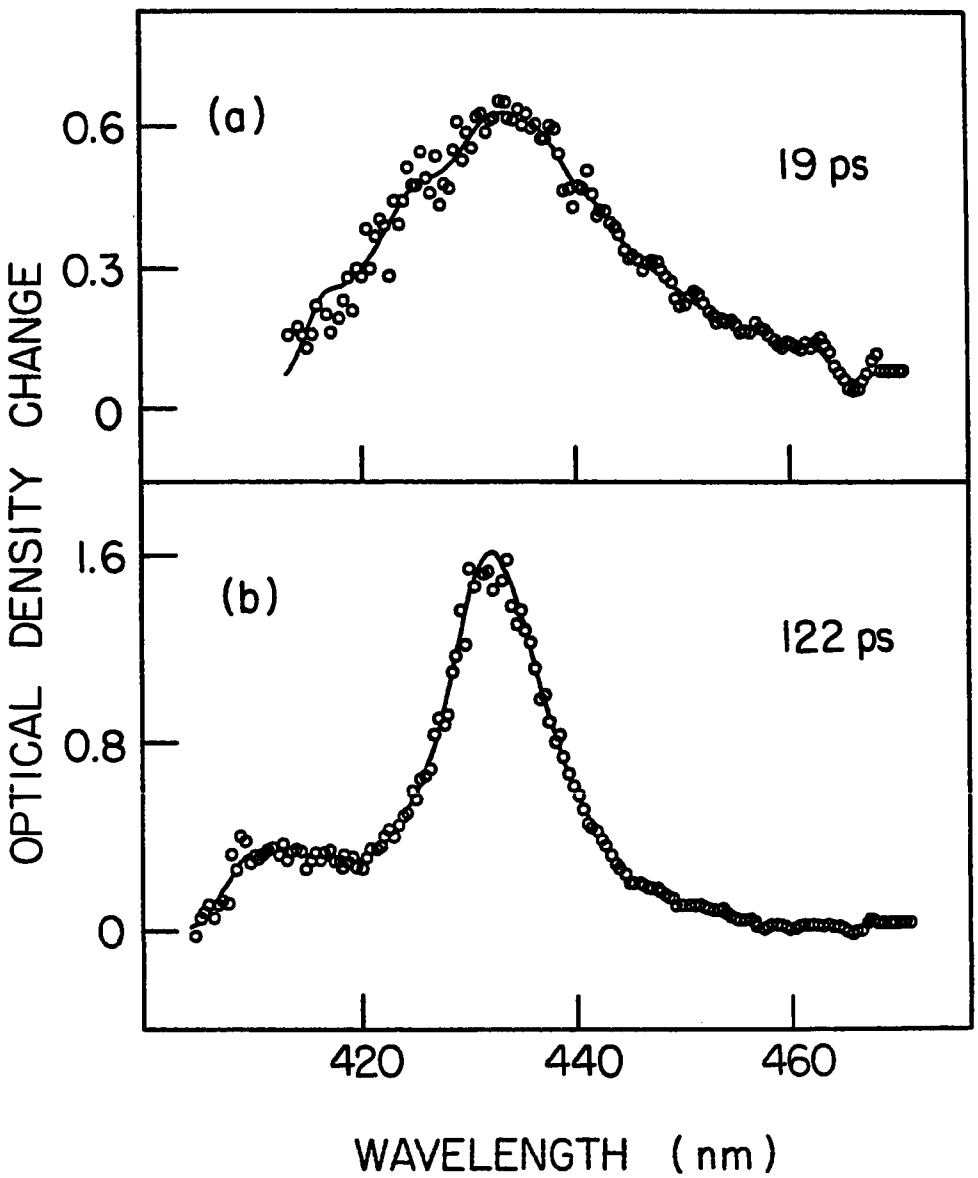

Figure 4-3. Transient absorption spectra of 2-iodoanthracene in cyclohexane (a) 19 ps and (b) 122 ps after excitation

The optical density changes at the wavelength of maximum long-time $T_1 \rightarrow T_n$ absorption of both iodoanthracenes were plotted as a function of time and are shown in Figure 4-4.

To explain these time dependent OD changes, we tentatively suggested in an earlier paper (170) that the data could be reproduced by a phenomenological though reasonable model (scheme I) expressed as

$$S_1(v) \xrightarrow{k_T} S_1(T) \xrightarrow{k_{isc}} T_2 \xrightarrow{k_d} \text{photofragments}$$

$$\Big\downarrow k_{ic}$$

$$T_1$$

$S_1(v)$ is the initially excited vibronic state with excess vibrational energy, $S_1(T)$ is the thermalized S_1 state, T_2 is the triplet state into which the thermalized S_1 state intersystem crosses, and T_1 is the lowest excited triplet state.

Since that paper (170), photolysis experiments optically exciting higher vibronic states (>7000 cm^{-1} of excess energy) within S_1 in the iodoanthracenes have been performed, and show that photodissociation does not occur exclusively via scheme I. Note that in scheme I, T_2 dissociates through a spin allowed nonadibatic crossing. The new information, to be discussed in the next section, combined with the picosecond studies discussed in this section suggest a revision of scheme I.

In the picosecond fluorescence experiments performed on 9-iodoanthracene in cyclohexane in our laboratory using an optical Kerr shutter and monitoring at 420 nm, we observed the S_1 lifetime after

Figure 4-4. Time-dependent optical density changes ($\Delta OD(t) = \Delta OD(\infty)\{1 - \exp(-t/\tau_r)\}$) at 432 nm for (a) 9-iodoanthracene in cyclohexane and (b) 2-iodoanthracene in cyclohexane for various rise times τ_r: (a) ——, τ_r = 10 ps; ---, τ_r = 50 ps; -·-, τ_r = 200 ps; (b) ---, τ_r = 30 ps; -·-·, τ_r = 50 ps. The error bars are twice the standard deviation of the normalized optical density changes at each delay

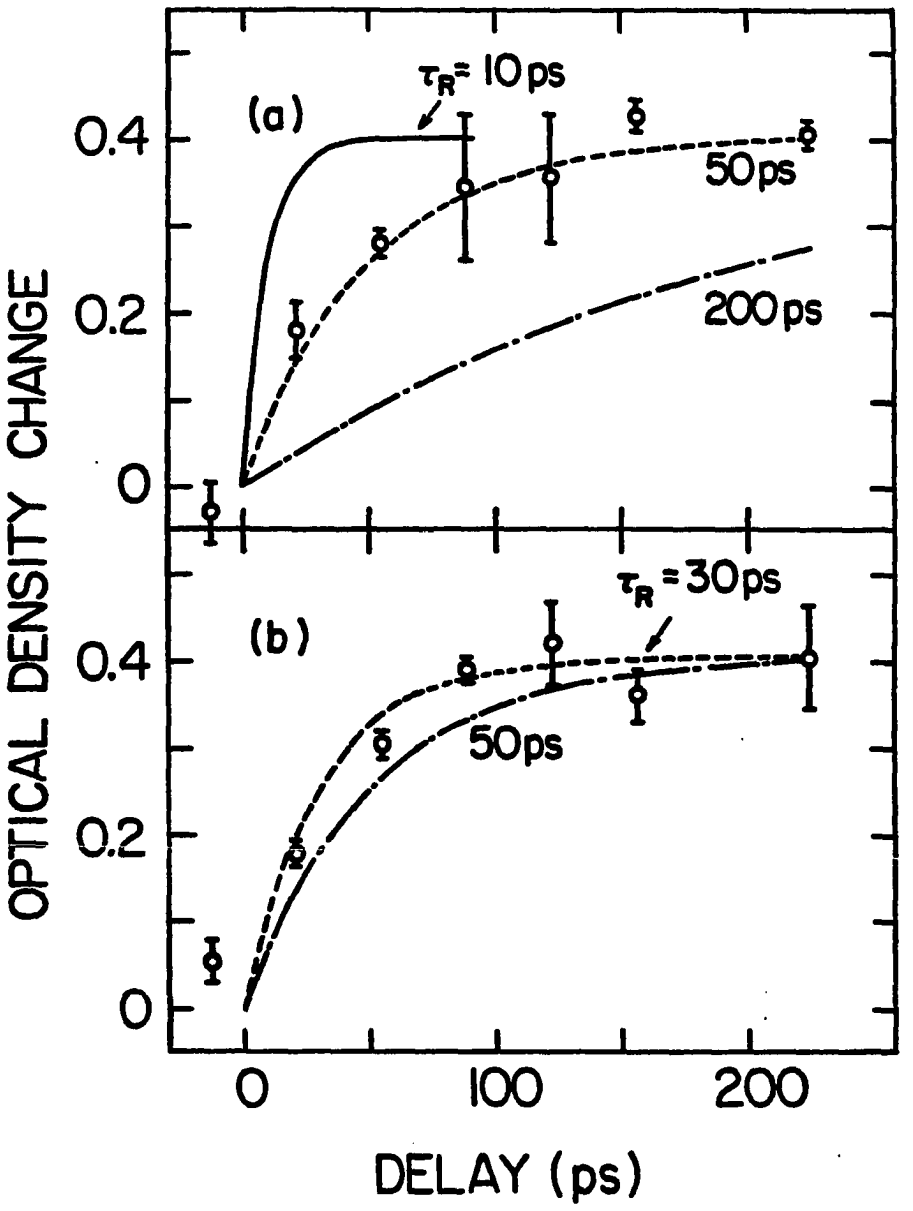
τ_R= 10ps
(a)
50ps
200ps
τ_R = 30ps
(b)
50ps
0.4
0.2
0
0.4
0.2
0
0
100
200
OPTICAL DENSITY CHANGE
DELAY (ps)

excitation by 354 nm pulses to be approximately 65 ps at room temperature with no detectable risetime within the ~10 ps resolution of the experimental apparatus (150). Subsequently, Rentzepis' group at Bell Laboratories using a streak camera and monitoring the visible broadband emission found a 55 ps fluorescence decay time with a prompt risetime (<5 ps) in 9-iodoanthracene under similar excitation conditions (242). The fluorescence behavior in these experiments and in other studies on IC process in polyatomics (243, 244), rapid thermalization of the vibronic levels is indicated.

In this limit, the T_1 state population, $N_{T_1}(t)$ can be expressed:

$$N_{T_1}(t) = N_{S_1}(0) \frac{k_{ic}}{k_{ic} + k_d} [1 - \frac{k' \exp(-k_{isc}t)}{k' - k_{isc}} + \frac{k_{isc} \exp(-k't)}{k' - k_{isc}}] \quad (4.3)$$

where k_{ic} is the internal conversion rate constant for $T_2 \rightarrow T_1$, k_{isc} is the rate constant for $S_1 \rightarrow T_2$ ISC, k_d is the dissociation rate constant and $k' = k_{ic} + k_d$.

Examination of the time behavior of the transient absorption in Figure 4-4 reveals no detectable inflection point expected of the dual exponential behavior, within the time resolution of the experiment. A better fit to the data can be made by a single exponential curve,

$$\Delta OD(t) = \Delta OD(\infty)\{1 - \exp(-t/\tau_r)\} \quad . \quad (4.4)$$

The single exponential behavior exhibited by the $T_1 \rightarrow T_n$ risetimes can be rationalized in terms of scheme I if the total dissipative rate constant, k', from the emergent triplet T_2 substantially exceeds the rate

of k_{isc} and if $k_{isc} \tilde{=} (\tau_r)^{-1}$. Physically this corresponds to no appreciable buildup of T_2 population due to rapid branching into a photodissociative channel or internal conversion to T_1, the rate limiting step being the ISC rate into the triplet manifold.

From Figure 4-4, the risetime for the 9-iodoanthracene transient absorption is approximately 50 ps, while that in 2-iodoanthracene appears somewhat shorter, ~30-40 ps although the inherent scatter in OD data derived from multishot techniques does not justify assigning significant differences to the time dependent changes in optical density behavior of the two aryl halides.

An estimation of the quantum yield for the formation of T_1 state or 9-iodoanthracene was made by comparing the normalized optical density changes for the 9-iodoanthracene to those for acridine in n-hexane, a molecule which has been studied extensively (224, 225). As in other anthracene-like molecules, acridine has a $T_1 \rightarrow T_n$ absorption band in the vicinity of 430 nm. For the quantum yield evaluation, solutions of both acridine and 9-iodoanthracene were prepared with identical optical densities at 354 nm, and examined at the long-time delay ($\pm$ 290 ps).

The change in optical density can be written

$$OD = \varepsilon_{TT}\phi_{isc}I_p \quad . \qquad (4.5)$$

here ε_{TT} is the extinction coefficient for the transition $T_1 \rightarrow T_n$, ϕ_{isc} is the ISC quantum yield for $S_1 \rightarrow T_1$, and I_p is the intensity of the pump light. To standardize ϕ_{isc}^{9IA} to ϕ_{isc}^{ACR}, one needs to evaluate

$$\frac{\phi_{isc}^{9IA}}{\phi_{isc}^{ACR}} = \frac{\varepsilon_{TT}^{ACR} I_p^{ACR} \Delta OD^{9IA}}{\varepsilon_{TT}^{9IA} I_p^{9IA} \Delta OD^{ACR}} \quad . \qquad (4.6)$$

Recent literature values for acridine are $\phi_{isc} = 0.4$ and $\varepsilon_{TT} = 31,500$ (225). The TTA extinction coefficient for 9-iodoanthracene has not been determined. If one uses the TTA coefficient of the 9-bromoanthracene in cyclohexane ($\varepsilon = 66500$ at 425 nm (224)) as an approximate value for ε_{9IA}, the experimentally derived ϕ_{isc} for $S_1 \rightarrow T_1$ transition in 9-iodoanthracene is found to be ≈ 0.2. From equation 4.3,

$$\frac{k_{ic}}{k_d + k_{ic}} \approx 0.2 \text{ , or } k_d \approx 4\, k_{ic} \text{ .}$$

The above estimates depend on the validity of the model proposed in scheme I and the values for the constants in equation 4.6. A comparison between the long-time transient absorption FWHM for our aryl iodides (Figure 4-3) and the 9-bromoanthracene in cyclohexane absorption (224) indicates that the iodides are approximately 1.2 times broader. If the value of the ε_{TT} for 9-iodoanthracene were only half of the ε_{TT} of 9-bromoanthracene and the ISC yield was substantially larger, say unity, the value for $k_{ic}/(k_d + k_{ic}) \approx 0.8$, indicating that T_1 is still created with less than unit quantum efficiency. From the photolysis results (vide infra), some part of this disparity in quantum efficiency is due to dissociation.

Photochemical results from photolysis of iodoanthracenes

The picosecond photophysical experiments have recently been complemented by the results from small-scale photolysis experiments on

iodoanthracenes carried out under the direction of Dr. Richard Johnson at Iowa State University. In these experiments, degassed solutions of 1-, 2-, and 9-iodoanthracene in cyclohexane or benzene were irradiated under argon by a 200 W high pressure mercury lamp, and the photo products analyzed by high pressure liquid chromatography. The results from these experiments are summarized in Table 4-1.

Table 4-1. Quantum efficiencies for photoreactions of isomeric iodoanthracenes

Substrate	Solvent	λ	ϕ anthracene	ϕ phenylanthracene	ϕ reaction[a]
1-iodo	benzene	313 nm	0.003	0.030	0.03
2-iodo	benzene	313 nm	0.002	0.091	0.09
9-iodo	benzene	313 nm	0.076	0.012	0.4
1-iodo	cyclohexane	313 nm	0.019	--	0.02
2-iodo	cyclohexane	313 nm	0.053	--	0.05
9-iodo	cyclohexane	313 nm	0.058	--	0.06
9-iodo	cyclohexane	250 nm	0.057	--	0.06
9-iodo	cyclohexane	402 nm	0.034	--	0.03

[a]Quantum yield for disappearance of starting material (courtesy of Dr. R. P. Johnson, Iowa State University, Ames, Iowa).

Irradiation at 313 nm in benzene yielded primarily phenylanthracene with small amounts of anthracene for the 1- and 2-isomers of iodoanthracene; anomalously, the 9 isomer yielded primarily anthracene. In cyclohexane at 313 nm, only anthracene and iodine were found as photoproducts for all three isomers. Table 4-1 also displays a preliminary study of

the wavelength effect on quantum yields of 9-iodoanthracene in cyclohexane. At the wavelengths 250 nm and 313 nm, the anthracene formation quantum yields were 0.057 and 0.058 respectively, whereas at 402 nm the yield is 0.034, approximately 40% lower. Of particular interest are the differences between irradiation at 402 nm and 313 nm. Presumably both of these excitation wavelengths excite vibronic levels within S_1 and differences in the photoproduct yields are not normally expected (245), because complete vibrational relaxation occurs prior to photoreaction in most photochemistry. Triplet photosensitization experiments were performed on 9-iodoanthracene using biacetyl (E_T ~ 19,240 cm^{-1}) and acetophenone (E_T ~ 25,880 cm^{-1}) as sensitizers. Analyses by high pressure liquid chromatography found no anthracene photoproducts.

From the photoproduct analyses, one sees that the quantum efficiency for dehalogenation for both the 9 and 2 isomers in cyclohexane is less than 0.1. This represents a lower bound on the efficiency of the photodissociation process in solution, since geminate recombination of the anthryl and iodine radicals can occur.

The magnitude of the recombinations can be quite large due to the cage effect of the solvent. In picosecond studies on the photodissociation of I_2 in CCl_4, Chaung et al. (246) found ~75% of all the photodissociated I_2 molecules underwent geminate recombinations within 100 ps of excitation. Similar geminate recombinations can be occurring in these solutions although the magnitude of this process is not known.

Discussion

The nonradiative processes governing the photophysics of anthracenes have been studied extensively. In nonreactive anthracenes, one of the principal determinants governing the rates of radiationless processes is the relative positions of the triplet states with respect to the S_1 origin (247-250). For example, the decrease in fluorescence quantum yield with an increase in temperature in meso-substituted anthracenes was postulated to have been due to an increase in the ISC rate due to thermal activation (247-250). The large energy gap between the S_1 and T_1 origins in anthracenes, ~12,000 cm^{-1}, theoretically argues against direct ISC coupling of S_1 and T_1 due to unfavorable Franck-Condon overlap factors (251-252). Authors have, therefore, invoked the participation of higher-lying triplet states in the ISC process (240, 250, 253, 254). Direct experimental evidence for such participation has been demonstrated by Gillispie and Lim (253-254), who observed triplet-triplet fluorescence (TTF) in the near IR in several substituted anthracenes after excitation into the S_1 state. Using the results from the TTF experiments and phosphorescence studies, Gillispie and Lim established the presence of a fluorescencing triplet state 330 cm^{-1} and 780 cm^{-1} above the S_1 origin in 9-bromoanthracene (9BA) and in 9,10-dibromoanthracene (DBA), respectively. Analogous temperature dependence on the fluorescence lifetime of 9-iodoanthracene in cyclohexane has been demonstrated in our laboratory (150). At 23°C, the fluroescence lifetime is ~68 ps; raising the temperature to 65°C truncates the fluorescence lifetime to 31 ps. This temperature behavior is indicative

of a triplet lying ~1200 cm^{-1} above S_1.

In anthracene, Pariser (255) has calculated that the second triplet state is of $^3B_{1g}$ symmetry and Kellogg (256), in his study on triplet-triplet absorption in the near IR, assigned the 895 nm transient absorption band to a $^3B_{2u} \rightarrow {}^3B_{1g}$ triplet-triplet transition, suggesting that it was responsible for the temperature independent ISC in anthracene. In meso-substituted anthracenes, however, assignment of $^3B_{1g}$ to the second triplet may not be warranted in light of the anomalous TTF quantum yields reported by Gillispie and Lim (254). If one assumes that T_2 decays primarily by IC to T_1 in nonphotoreactive anthracenes, the quantum yield for fluorescence can be expressed,

$$\phi_{TTF} = \phi_{isc}^{S_1 \rightarrow T_2} \, k_{T_2-T_1}^{rad} \, \tau_{T_2} \quad , \tag{4.7}$$

where $\phi_{kc}^{S_1-T_1}$ is the quantum yield for formation of T_2 via ISC from S_1, $k_{T_2-T_1}^{rad}$ is the radiative rate constant derivable from the integrated TTA spectrum, and τ_{T_2} is the lifetime of the T_2 state.

For most anthracenes at room temperature, the range of ϕ_{isc} is between 0.3-1.0 (247-250). Estimates for the radiative rate constant from the integrated TTA spectrum typically range from 2-6 x 10^5 s^{-1} (257). The lifetime of the T_2 state has been estimated by 2 methods: photosensitization studies by Campbell and Liu (258) give an inferred value of ~200 ps; an energy gap law correlation of IC rates in aromatics also gives an approximate lifetime of 200 ps (259). Using the above estimates, one predicts a TTF quantum yield of ~10^{-5} in contrast to the experimentally found values of ~10^{-8} (254). The extremely low

fluorescence yield suggest a much shorter T_2 lifetime than is predicted by the energy gap law or deduced from photosensitization experiments.

Other studies on the picosecond photophysics of the triplet states of unreactive anthracenes have demonstrated that T_1 is formed rapidly. Hamanoue et al. (240), performing comparable picosecond TTA experiments on nitroanthracenes, found $T_1 \rightarrow T_n$ absorption risetimes on the order of 70-90 ps. The fluorescence quantum yields at 77 K in the studied nitroanthracenes was estimated to be considerably less than 7×10^{-3}, corresponding to the limit of sensitivity in the detection system, and the ISC rate constant was suggested to be $\geq 10^{11}$ sec^{-1}. Even without the additional decay channel provided by a dissociative process, the emergent higher level triplet state created during ISC from S_1 seems to undergo rapid radiationless processes in many anthracenes.

In the context of scheme I and the behavior of the risetime data presented in Figure 4-4, the dissipative rate for T_2, $k_d + k_{ic}$, should be $\geq 10\ k_{isc}$, or $k_{ic} \geq 4 \times 10^{10}$ s^{-1}. The rate for k_{ic} could change if the conservative approximations made to calculate the branching ratio in equation 4.6 were to change significantly; however, even in that case (vide supra immediately after equation 4.6), it is unlikely that the IC rate will decrease to 5×10^9 sec^{-1}.

In view of the ultrafast IC rates within the triplet manifold in anthracenes and the anomalous TTF quantum yields, examination of the validity of the energy gap law in anthracenes is warranted.

Nonradiative transitions in large polyatomics are often discussed within the context of Fermi's golden rule (260),

$$k_{nr}^{s\to\ell} = \frac{2\pi}{h} |V_{s\ell}|^2 \rho_\ell(E_s) \qquad (4.8)$$

where $V_{s\ell}$ is the matrix coupling element between the initial state $|s\rangle$ and the final state $|\ell\rangle$ and $\rho_\ell(E_s)$ is the density of states in $|\ell\rangle$ isoenergetic with E_s, the energy of $|s\rangle$. Within the Born-Oppenheimer approximation, $V_{s\ell}$ can be considered the product of an electronic factor, $\beta_{e\ell}$, and a vibrational overlap factor, $\langle\chi_s(Q)|\chi_T(Q)\rangle$ where $\chi_i(Q)$ is the vibrational wavefunction in $|i\rangle$ for the normal coordinate Q. The nonradiative rate constant for $|s\rangle \to |\ell\rangle$ can now be expressed

$$k_{s\ell}(\underline{m}) = \frac{2\pi}{h} \beta_{s\ell}^2 \sum_{\underline{n}} |\langle\underline{m}|\underline{n}\rangle|^2 \delta(\Delta E_{s\ell} + \sum_i m_i h\omega_i^{(s)} - \sum_i n_i h\omega_i^{(\ell)}) \qquad (4.9)$$

$\underline{m}$ and $\underline{n}$ denote the sets of 3N-6 quantum numbers specifying the vibrational excitation in $|s\rangle$ and $|\ell\rangle$ respectively. $\Delta E_{s\ell}$ is the energy separation between the vibrationless $|s\rangle$ and $|\ell\rangle$ and ω_i is the frequency of the ith vibrational degree of freedom. The delta function over the energy expressions requires the process to conserve energy. For clarity, Figure 4-5, schematically depicts the relations in equation 4.9. Considering the simplest situation where $|s\rangle$ is vibrationally relaxed, $\underline{m} = 0$, and only one vibrational mode, designated 1, is undergoing the transition to $|\ell\rangle$ from $|s\rangle$ without a change in frequency, $\Delta\omega_i = 0$ but experiences a displacement in equilibrium position, $\Delta Q = Q_s^\circ - Q_i^\circ$. All the other modes have identical frequency and equilibrium positions in both states. This allows equation 4.9 to be written

$$k_{s\ell}(\underline{0}) = \frac{2\pi}{h} \beta_{s\ell}^2 \sum_{n_1} |\langle 0|n_1\rangle|^2 \delta(\Delta E_{s\ell} - n_1 h\omega_1) \qquad (4.10)$$

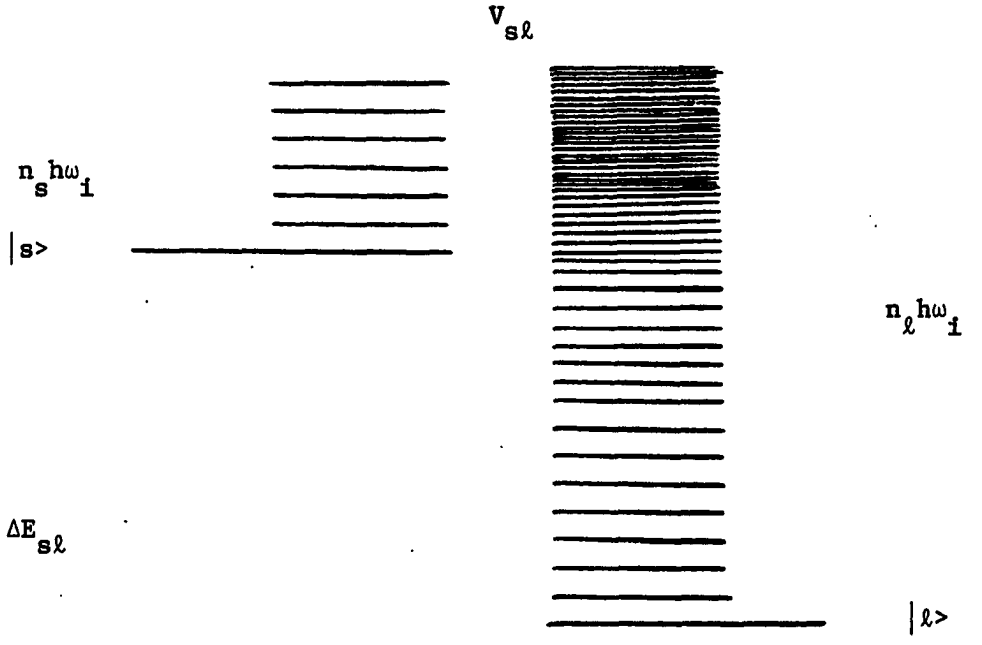

Figure 4-5. Electronic level scheme used to derive the expression for the nonradiative rate constant; see text

n_1 is the vibrational quantum number in $|\ell>$ for mode 1. When $n_1 \equiv \Delta E_{s\ell}/h\omega_1$ is large, the summation can be replaced by an integral and

$$k_{s\ell}(0) \rightarrow \frac{2\pi}{h} \beta_{s\ell}^2 \int_0^\infty dn_1 |<0|n_1>|^2 \delta\left[h\omega_1\left(\frac{\Delta E_{s\ell}}{h\omega_1} - n_1\right)\right]$$

$$= \frac{2\pi}{h^2\omega_1} \beta_{s\ell}^2 |<0|n_1>|^2 \Big|_{n_1 \equiv \gamma} \qquad (4.11)$$

where the property of the delta function has been used and $\gamma \equiv \Delta E_{s\ell}/h\omega_1$. For the case of harmonic oscillators and large $\Delta E_{s\ell}$, equation 4.11 becomes

$$k_{s\ell}(0) \approx \left(\frac{2\pi h\omega_1}{\Delta E_{s\ell}}\right)^{\frac{1}{2}} \frac{\beta^2}{h^2\omega_1} \exp(-\gamma) \exp[-\gamma(\ln \frac{\gamma}{\Delta} - 1)] \qquad (4.12)$$

where $\Delta = \mu\omega(Q_s^\circ - Q_i^\circ)^2/2h$ is a dimensionless parameter which contains the reduced mass and shift in equilibrium position for the mode promoting the transition. Because the last exponential term of equation 4.12 contains $\Delta E_{s\ell}$, the nonradiative rate constant has an exponential dependence on the energy gap. The expression derived is the simplest computationally and more detailed treatments are available elsewhere (9, 10), but equation 4.12 contains the salient features of the energy gap law. If the variations in the electronic matrix element, the equilibrium position and frequency distortion of the promoting oscillators are small between the same nonradiative process occurring in different aromatic molecules, the nonradiative rate can be correlated with the normal mode structure and the energy gap. Siebrand and Williams (251-252) pioneered these correlations for $T_1 \rightarrow S_0$ ISC in rigid

aromatics and Murata et al. (261) demonstrated the principle for $S_2 \rightarrow S_1$ IC in substituted azulenes. In the polyacenes, relevant to our discussion, Gillispie and Lim (259) correlated experimental IC rate constants to those predicted by the energy gap formalism. Within a factor of 2.5, the predicted rate constants and the experimental ones were in agreement. For the $T_2 \rightarrow T_1$, IC in 9,10-dibromoanthracene with $\Delta E_{T_2T_1} \simeq 12{,}000\ cm^{-1}$, the IC rate constant is calculated to be $4.3 \times 10^9\ sec^{-1}$ or ~230 ps.

Considering the previously mentioned experimental data, one might ask why the usually valid energy gap law has predicted a considerably slower $T_2 \rightarrow T_1$ IC rate than that which is found experimentally. Several groups (170, 240, 259) have advanced the proposal that there exists at least one additional nearly degenerate triplet in the vicinity of the triplet to which ISC occurs from S_1. Two vicinal triplets could easily undergo internal conversion rapidly in accordance with the energy gap law and then undergo further IC to the T_1 state. Lim postulated the existence of such a state to explain the anomalously low TTF quantum yields in substituted anthracenes (254).

In regard to the anomalous TTF yields, if the ordering of the adjacent triplet states was $T_2 = {}^3B_{3u}$ and $T_3 = {}^3B_{1g}$, the reverse of what they are assigned to be in anthracene (247, 256), then the fluorescence quantum yield of ${}^3B_{1g} \rightarrow {}^3B_{2u}$ ($T_3 \rightarrow T_1$) would be truncated by rapid IC to the electric-dipole forbidden triplet, ${}^3B_{3u}$. In addition to rapid IC between two closely-lying electronic states, if the two states became vibronically coupled, proximity effects could be

induced enhancing nonradiative decay to T_1 and exceeding nonradiative rates predicted by the energy gap law.

Both Kellogg (256) and Bennett and McCartin (250), in their studies on long-time TTA from T_1 to the first optically allowed triplet in anthracenes, observed a substantial structureless absorption immediately to the blue of the structured spectra they both assigned $^3B_{2u} \rightarrow {}^3B_{1g}$. Kellogg suggested the absorption was to other unassigned triplets in the same region (256). Theoretical calculations by Pariser (255) predicted 8 triplets below 40000 cm^{-1}, and the results from Ruedenberg's CI calculation of optically allowed triplet states, in anthracene shown in Figure 4-1, also illustrate that the existence of more than one triplet is possible near S_1. The conjecture that a third triplet state plays a vital role in the triplet state dynamics in anthracenes offers a reasonable answer to the observed picosecond data without discarding the energy gap law.

As mentioned in the introduction, the recent photochemical results discussed in the Procedure and Results section of this chapter require a revision of scheme I. Excitation of 9-iodoanthracene in cyclohexane at 313 nm and 402 nm produced anthracene formation yields of 0.058 and 0.038 respectively. The disparity in the quantum yields indicates that a more efficient channel for photodissociation is available for molecules excited by 313 nm light, and that thermalization of S_1 is not a prerequisite for dissociation as indicated by scheme I. The most likely (but not unique) mechanism for the dissociation of the higher vibronic levels is predissociation of S_1 vibronic levels via spin-orbit coupling

to a repulsive triplet state. An analogous mechanism has been postulated for the gas-phase photodissociation of iodobenzene, iodonapthalene and 4-iodobiphenyl which occurs from S_2 within ~1 ps after excitation (226).

A caveat to this interpretation is that it depends on the validity of the assumption that excitation at 312 nm (~32,000 cm^{-1}) is strictly localized in S_1. As in the triplet manifold, electronic states may be present that are not optically active, or so weak as to be masked by the intense $^1A_{1g} \rightarrow {}^1B_{2u}$ transition. Anthracene has a second singlet state, $^1B_{3u}$, the origin of which has yet to be experimentally detected, although several groups using different techniques have estimated it to lie at ~30,000 cm^{-1} (262, 263). A nonadiabatic transition to another singlet via vibronic coupling is a possibility and, if it occurs, could also alter the photodissociation yields. Furthermore, in anthracene, Astier and Meyer (264) have confirmed the presence of 4 triplets below 40,000 cm^{-1} other than T_1. Pariser's calculations (255) also show the possibility of 8 triplet states, 3 in the vicinity of 30,000 cm^{-1}. Participation of higher excited state triplets may also play a role in providing a nonradiative pathway.

Because substantial photodissociation still occurs from the lower vibronic levels of S_1 in 9-iodoanthracene upon excitation with 402 nm light, the importance of ISC from S_1 to the triplet manifold and subsequent spin-allowed dissociation as suggested by scheme I cannot be ruled out, especially since it reproduces the picosecond dynamics reasonably well. The lack of detectable photoproduct after triplet

photosensitization experiments with biacetyl, which only has enough energy to activate the T_1 level of 9-iodoanthracene, confirms the assumption that no dissociation occurs from thermalized T_1. The results from the sensitization with acetophenone are ambiguous, because the exact origin of T_2 is not known and the triplet energy of acetophenone may not be enough to activate T_2 in iodoanthracene.

A revision to scheme I which rationalizes the vibronic level dependence of photodissociation is presented in scheme II:

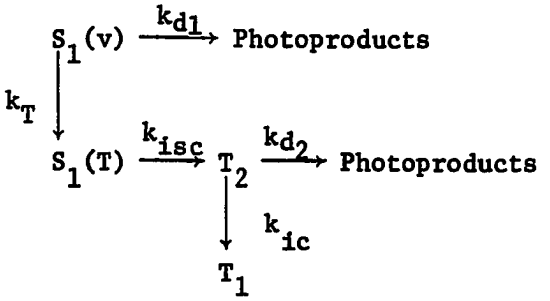

For this scheme, k_T would still proceed extremely rapidly, ~10^{11} sec^{-1}, as established by the single wavelength fluorescence studies on 9-iodoanthracene (150), and can also vary as a function of excess vibronic energy. Because we have photoproduct yields from excitation at only two wavelengths, 313 nm and 402 nm, scheme II may undergo some additional modifications when more detailed wavelength dependence data become available. More extensive photolysis experiments comparing photoproduct yields as a function of wavelength over the S_1 manifold would provide needed information to help clarify the photodissociation mechanisms in iodoanthracenes.

In conclusion, there is enough experimental evidence to believe that, in the iodoanthracenes, at least two photodissociation channels exist: one from the higher vibronic levels of S_1 which probably proceed via direct predissociation to a repulsive triplet induced by spin orbital coupling, and which is competitive with thermalization in the S_1 manifold; and a second channel, a spin allowed crossing involving 2 triplets, which opens after the molecule has undergone ISC to the triplet manifold from S_1. Two or more dissociation channels are not without precedent in the aryl halides. Recently, Freedman et al. (228) demonstrated that iodobenzene in the gas phase undergoes dissociation via two distinct pathways. After excitation to S_3, the molecule relaxes by IC into S_1 and then ISC to a dissociative triplet or the molecule undergoes an extreme distortion of the aromatic ring, similar to what is hypothesized to occur when benzene forms benzvalene or Dewar benzene, and dissociates the C-X bond.

One aspect of this study worth emphasizing is the fruitful collaboration between photophysical studies and photochemical studies which, when properly directed, can produce a more complete understanding of the phenomena being examined.

LITERATURE CITED

1. C. V. Shank, E. P. Ippen, S. L. Shapiro (eds.): Picosecond Phenomena, Springer Series in Chemical Physics, Vol. 4 (Springer, Berlin, 1978)

2. R. M. Hochstrasser, W. Kaiser, C. V. Shank (eds.): Picosecond Phenomena II, Springer Series in Chemical Physics, Vol. 14 (Springer, Berlin, 1980)

3. S. L. Shapiro (ed.): Ultrashort Light Pulses, Topics in Applied Physics, Vol. 18 (Springer, Berlin, 1977)

4. H. W. Mocker, R. J. Collins: Appl. Phys. Lett. 7, 270 (1965)

5. A.J. DeMaria, D. A. Stetser, H. Heynau: Appl. Phys. Lett. 8, 174 (1966)

6. J. W. Shelton, J. A. Armstrong: IEEE J. Quantum Electron. QE-3, 696 (1967)

7. R. I. Scarlet, J. F. Figueria, H. Mahr: Appl. Phys. Lett. 13, 11 (1968)

8. P. M. Rentzepis: Chem. Phys. Lett. 2, 117 (1968)

9. S. A. Rice: Excited States, Vol. 2, ed. by E. C. Lim (Academic Press, New York, 1975) p. 112-320

10. N. Turro: Modern Molecular Photochemistry (Benjamin-Cummings, Menlo Park, 1978)

11. J. I. Steinfeld, P. L. Houston: Lasers and Coherence Spectroscopy, ed. by J. I. Steinfeld (Plenum Press, New York, 1978) p. 38

12. P. Wirth, S. Schneider, F. Doerr: Chem. Phys. Lett. 46, 20 (1977)

13. E. C. Lim: In Excited States, Vol. 3, ed. by E. C. Lim (Academic Press, New York, 1977) p. 305-351

14. S. Marata, C. Iwanaga, T. Toda, H. Kokuhum: Ber. Bunsenges. Phys. Chem. 76, 1976 (1972)

15. P. M. Rentzepis: Science 169, 239 (1970)

16. J. P. Heritage, A. Penzkofer: Chem. Phys. Lett. 44, 76 (1976)

17. T. C. Felder, K. Choi, M. R. Topp: Chem. Phys. 64, 175 (1982)

18. L. Halliday, H. B. Lin, M. Topp: In Picosecond Phenomena, ed. C. V. Shank, E. P. Ippen, S. L. Shapiro (Springer, Berlin, 1978) p. 314-318

19. D. von der Linde, K. F. Rodgers: IEEE J. Quantum Electron. QE-9, 960 (1973)

20. J. P. Morand, C. P. Christensen, C. Wittig: IEEE J. Quantum Electron. QE-15, 1202 (1979)

21. D. Magde, M. W. Windsor: Chem. Phys. Lett. 24, 144 (1974)

22. R. G. W. Norrish, G. Porter: Nature 164, 658 (1949)

23. R. W. Anderson, R. M. Hochstrasser, H. Lutz, G. W. Scott: Chem. Phys. Lett. 28, 153 (1974)

24. V. Sundstrom, P. M. Rentzepis, E. C. Lim: J. Chem. Phys. 66, 4287 (1977)

25. R. R. Alfano, S. L. Shapiro: Chem. Phys. Lett. 8, 631 (1971)

26. R. B. Weisman, B. I. Greene: In Multichannel Image Detectors, ed. by Y. Talmi (American Chemical Society, Washington, 1971) p. 227-235

27. B. I. Greene, R. M. Hochstrasser, R. B. Wiesman: J. Chem. Phys. 70, 1247 (1979)

28. B. I. Greene: Chem. Phys. Lett. 79, 51 (1981)

29. B. I. Greene: Chem. Phys. Lett. 75, 206 (1980)

30. G. R. Fleming, O. L. Gijzeman, S. H. Lin: J. Chem. Soc. Faraday II 70, 1074 (1974)

31. D. Magde, S. T. Gaffney, B. F. Campbell: IEEE J. Quantum. Electron. QE-17, 489 (1981)

32. D. Magde, B. A. Bushaw, M. W. Windsor: Chem. Phys. Lett. 28, 263 (1974)

33. C. Lin, A. Dienes: Opt. Commun. 9, 21 (1973)

34. D. J. Bradley: In Ultrashort Light Pulses, ed. S. L. Shapiro, Topics in Applied Physics, Vol. 18 (Springer, Berlin, 1977) p. 18

35. W. Koechner: Solid State Laser Engineering, Springer Series in Optical Sciences, Vol. 1 (Springer, New York, 1976) p. 65

36. D. von der Linde: IEEE J. Quantum Electron. QE-6, 725 (1972)

37. D. J. Bradley, W. Sibbett: Opt. Communi. 9, 17 (1973)

38. L. A. Lompre, G. Mainfray, J. Thebault: Appl. Phys. Lett. 26, 500 (1975)

39. D. J. Bradley, M. H. R. Hutchinson, H. Koetser, T. Morrow, G. H. C. New, M. S. Petty: Proc. Roy. Soc. London 328A, 97 (1972)

40. M. M. Malley, P. M. Rentzepis: Chem. Phys. Lett. 3, 334 (1969)

41. M. R. Topp, P. M. Rentzepis, R. P. Jones: Chem. Phys. Lett. 9, 1 (1971)

42. G. E. Busch, M. L. Applebury, A. A. Lamola, P. M. Rentzepis: Proc. Nat. Acad. Sci. USA 69, 2802 (1972)

43. T. Kobayshi, S. Nagakura: Chem. Phys. 23, 153 (1977)

44. J. M. Grzybowski, S. E. Sugamori, D. F. Williams, R. W. Yip: Chem. Phys. Lett. 65, 456 (1979)

45. Y. Hirata, I. Tanaka: Chem. Phys. Lett. 41, 336 (1976)

46. G. E. Busch, P. M. Rentzepis: Science 194, 276 (1976)

47. G. E. Busch, P. M. Rentzepis, R. P. Jones: Chem. Phys. Lett. 18, 178 (1973)

48. D. Magde, M. W. Windsor: Chem. Phys. Lett. 27, 31 (1974)

49. D. Magde, M. W. Windsor, D. Holten, M. Gouterman: Chem. Phys. Lett. 29, 183 (1974)

50. R. M. Hochstrasser, A. C. Nelson: Lasers in Physical Chemistry and Biophysics, ed. by J. Jousiot-Dubien (Elsevier, Amsterdam) p. 305-322.

51. T. Netzel, R. Bucks, S. Boxer, J. Fujita: J. Phys. Chem. 86, 1947 (1982)

52. C. Creutz, M. Chou, T. Netzel, M. Okumura, N. Sutin: J. Am. Chem. Soc. 102, 1309 (1980)

53. J. A. Welch, K. S. Peters, V. Valda: J. Phys. Chem. 80, 1941 (1982)

54. L. J. Rothberg, N. J. Cooper, K. S. Peters, V. Valda: J. Am. Chem. Soc. 104, 3536 (1982)

55. T. R. Royt: In Picosecond Phenomena II, eds. R. M. Hochstrasser, W. Kaiser, C. V. Shank, Springer Series in Chemical Physics, Vol. 14 (Springer, Berlin, 1981) p. 3-6

56. B. Kopainsky, A. Seilmeier, W. Kaiser: In Picosecond Phenomena II, eds. R. M. Hochstrasser, W. Kaiser, C. V. Shank, Springer Series in Chemical Physics, Vol. 14 (Springer, Berlin, 1981) p. 7-11

57. S. M. George, C. B. Harris: Rev. Sci. Instr. 52, 852 (1981)

58. E. P. Ippen, C. V. Shank: In Quantum Electronics, Part B, ed. by C. L. Tang, Methods in Experimental Physics, Vol. 15 (Academic Press, New YOrk, 1979) p. 192-193

59. E. P. Ippen, C. V. Shank: Appl. Phys. Lett. 27, 488 (1975)

60. I. S. Rudduck, D. J. Bradley: Appl. Phys. Lett. 29, 296 (1976)

61. J. C. Diels, E. W. Van Stryland, D. Gold: In Picosecond Phenomena, eds. C. V. Shank, E. P. Ippen, S. L. Shapiro, Springer Series in Chemical Physics, Vol. 4 (Springer, Berlin, 1978) p. 117-120

62. D. L. Rosen, A. G. Doukas, Y. Budansky, A. Katz, R. R. Alfano: IEEE J. Quantum Electron. QE-17, 2264 (1981)

63. C. V. Shank, R. L. Fork, R. Yen, R. H. Stolen, S. Tomlinson: Appl. Phys. Lett. 40, 761 (1982)

64. J. K. Kuhl, R. Lambrich, D. von der Linde: Appl. Phys. Lett. 31, 657 (1977)

65. A. J. Cox, D. E. Damschen, C. D. Meritt, G. W. Scott, L. D. Talley: In Picosecond Phenomena, eds. C. V. Shank, E. P. Ippen, S. L. Shapiro, Springer Series in Chemical Physics, Vol. 4 (Springer, Berlin, 1978) p. 63-66

66. J. N. Eckstein, A. J. Ferguson, T. W. Hansch, C. A. Minard, C. K. Chan: Opt. Commun. 27, 466 (1978)

67. E. P. Ippen, C. V. Shank, A. Dienes: Appl. Phys. Lett. 21, 348 (1972)

68. F. O'Neill: Opt. Commun. 6, 360 (1972)

69. D. J. Bradley: In Ultrashort Light Pulses, ed. S. L. Shapiro, Topics in Applied Physics, Vol. 18 (Springer, Berlin, 1977) p. 57

70. E. P. Ippen, C. V. Shank, R. L. Woerner: Chem. Phys. Lett. 46, 20 (1977)

71. C. V. Shank, E. P. Ippen, O. Teschke, R. L. Fork: Chem. Phys. Lett. 57, 433 (1978)

72. E. P. Ippen, C. V. Shank, A. Lewis, M. Marcus: Science 200, 1279 (1978)

73. C. V. Shank, E. P. Ippen, R. Bersohn: Science 193, 50 (1976)

74. C. V. Shank, D. H. Austin, E. P. Ippen, O. Teschke: Solid State Commun. 26, 567 (1978)

75. J. M. Wiesenfeld, E. P. Ippen, A. Corin, R. Bersohn: J. Am. Chem. Soc. 102, 7256 (1980)

76. G. R. Fleming: In Advances in Chemical Physics, ed. by I. Prigogine, S. A. Rice, Vol. 49 (John Wiley & Sons, New York, 1982) p. 1-46

77. A. Icsevgi, W. E. Lamb: Phys. Rev. 185, 517 (1969)

78. D. J. Bradley, A. J. F. Durrant: Phys. Lett. 27A, 73 (1968)

79. W. H. Glenn, M. J. Brienza, A. J. DeMaria: Appl. Phys. Lett. 12, 54 (1968)

80. B. H. Soffer, J. W. Linn: J. Appl. Phys. 39, 5859 (1968)

81. C. K. Chan, S. O. Sari: Appl. Phys. Lett. 25, 403 (1974)

82. E. P. Ippen, C. V. Shank: In Ultrashort Light Pulses, ed. by S. L. Shapiro, Topics in Applied Physics, Vol. 18 (Springer, Berlin, 1977) p. 109

83. A. von Jena, H. Lessing: Appl. Phys. 19, 131 (1979)

84. J. Langclaar, M. Leeuw, D. Bebelaar, R. P. Rettschnick: In Picosecond Phenomena II, ed. by R. M. Hochstrasser, W. Kaiser, C. V. Shank, Springer Series in Chemical Physics, Vol. 14 (Springer, Berlin, 1980) p. 171-174

85. P. M. Felker, W. R. Lambert, A. H. Zewail: J. Chem. Phys. 77, 1603 (1982)

86. W. R. Lambert, P. M. Felker, A. H. Zewail: J. Chem. Phys. 75, 5958 (1981)

87. C. V. Shank, E. P. Ippen, O. Teschke: Chem. Phys. Lett. 45, 291 (1977)

88. C. V. Shank, E. P. Ippen: Appl. Phys. Lett. 26, 62 (1975)

89. D. H. Waldeck, A. J. Cross, D. B. McDonald, G. R. Fleming: J. Chem. Phys. 74, 3361 (1981)

90. D. H. Waldeck, G. R. Fleming: J. Phys. Chem. 85, 2614 (1981)

91. D. H. Waldeck, W. T. Lotshaw, D. B. McDonald, G. R. Fleming: Chem. Phys. Lett. 88, 797 (1982)

92. R. K. Jain, J. P. Heritage: Appl. Phys. Lett. 32, 41 (1978)

93. W. H. Hesselink, D. A. Wiersma: Chem. Phys. Lett. 56, 227 (1978)

94. E. P. Ippen, C. V. Shank: In Picosecond Phenomena, ed. by C. V. Shank, E. P. Ippen, S. L. Shapiro, Springer Series in Chemical Physics, Vol. 4 (Springer, Berlin, 1978) p. 103-106

95. A. Migus, C. V. Shank, E. P. Ippen, R. L. Fork: IEEE J. Quantum Electron. QE-18, 101 (1982)

96. T. Gillbro, V. Sundstrom: Chem. Phys. Lett. 74, 188 (1980)

97. J. M. Wiesenfeld, E. P. Ippen: Chem. Phys. Lett. 67, 213 (1978)

98. J. L. Martin, R. Astier, A. Antonetti, C. A. Minard, A. Orszay: C. R. Acad. Sci. Ser. B 289, 45 (1979)

99. C. V. Shank, R. L. Fork, R. F. Leheny, J. Shah: Phys. Rev. Lett. 42, 112 (1979)

100. S. R. Rotman, C. Roxlo, D. Bebelaar, T. K. Yee, M. M. Salour: Appl. Phys. B. 28, 319 (1982)

101. T. Kobayashi, Y. Ohashi: In Picosecond Phenomena II, ed. by R. M. Hochstrasser, W. Kaiser, C. V. Shank, Springer Series in Chemical Physics, Vol. 14 (Springer, Berlin, 1980) p. 181-185

102. P. Bado, S. B. Wilson, K. R. Wilson: Rev. Sci. Inst. 53, 706 (1982)

103. P. Bado, P. H. Berens, K. R. Wilson: In Picosecond Lasers/Applications, ed. by L. S. Goldberg, Proc. Soc. Photo-optic. Instrum. Engin. 322, 322 (1982)

104. J. P. Heritage: In Picosecond Phenomena II, ed. by R. M. Hochstrasser, W. Kaiser, C. V. Shank, Springer Series in Chemical Physics, Vol. 14 (Springer, Berlin, 1980) p. 343-347

105. B. F. Levine, C. G. Bethea: Appl. Phys. Lett. 86, 245 (1980)

106. B. F. Levine, C. G. Bethea: IEEE J. Quantum Electron. QE-16, 85 (1980)

107. K. B. Eisenthal: Ann. Rev. Phys. Chem. 28, 207 (1977)

108. H. Laubereau, W. Kaiser: Ann. Rev. Phys. Chem. 26, 83 (1975)

109. T. L. Netzel, W. J. Struve, P. M. Rentzepis: Ann. Rev. Phys. Chem. 24, 473 (1973)

110. S. C. Pyke, M. W. Windsor: In Chemical Experimentation Under Extreme Conditions, ed. by A. Weissberger, Techniques of Chemistry IX (John Wiley & Sons, New York, 1979) p. 205-276

111. A. E. Siegman: An Introduction to Lasers and Masers (McGraw-Hill, New York, 1971)

112. J. T. Verdeyen: Laser Electronics (Prentice-Hall, Englewood Cliffs, N.J., 1981)

113. A. Yariv: Quantum Electronics, 2nd Ed. (John Wiley & Sons, New York, 1975)

114. O. Svelto: Principles of Lasers (Plenum Press, New York, 1976)

115. Owens-Illinois is no longer in business. Comparable glasses can be obtained from Schott Glass (LG-670), Kigre (Q246), and Hoya (LSG-91H)

116. J. G. Gonce, W. J. Mitchell: IEEE J. Quantum Electron. QE-3, 330 (1967)

117. W. Koechner: Solid State Laser Engineering, Springer Series in Optical Science, Vol. 1 (Springer, Berlin, 1976) p. 465

118. D. J. Bradley, G. H. C. New, S. J. Caughey: Opt. Commun. 2, 41 (1970)

119. A. Penzkofer, D. von der Linde, A. Laubereau, W. Kaiser: Appl. Phys. Lett. 20, 351 (1972)

120. A. G. Doukas, J. Buchert, R. R. Alfano: In Biological Events Probed By Ultrashort Laser Spectroscopy, Chapter 17 (Academic Press Inc., New York, 1982) p. 387-416

121. Optical Cell Inc. (Woodbine, MD) Bulletin 65, Company product literature

122. D. von der Linde: IEEE J. Quantum Electron. QE-8, 328 (1972)

123. M. A. Duguay, J. W. Hansen, S. L. Shapiro: IEEE J. Quantum Electron. QE-6, 7250 (1970)

124. F. DeMartini, C. H. Townes, T. K. Gustafson, P. L. Kelly: Phys. Rev. 164, 312 (1967)

125. R. A. Fisher, P. L. Kelly, T. K. Gustafson: Appl. Phys. Lett. 14, 140 (1969)

126. V. V. Korobkin, A. A. Malyatin, M. Yu Schelev: Sov. Phys. JETP Lett. 11, 103 (1970)

127. R. Goldstein: Laser Focus 4, 21 (1968)

128. W. Koechner: Solid State Laser Engineering, Springer Series in Optical Sciences, Vol. 1 (Springer, Berlin, 1976) p. 413

129. Lasermetrics Inc. (Englewood, N.J.) OEM-813 product literature

130. A. H. Guenther, J. R. Bettis: Proc. IEEE 59, 689 (1971)

131. L. L. Steinmetz: Rev. Sci. Inst. 39, 904 (1968)

132. A. J. Alcock, M. C. Richardson, K. Leopold: Rev. Sci. Inst. 41, 1028 (1970)

133. D. von der Linde, O. Bernecker, A. Laubereau: Opt. Commun. 2, 215 (1970)

134. N. Bloembergen: Nonlinear Optics (Benjamin-Cummings, Reading, 1965)

135. D. H. Austin: In Ultrashort Light Pulses, ed. by S. L. Shapiro, Topics in Applied Physics, Vol. 18 (Springer, Berlin, 1977) p. 123-203

136. E. P. Ippen, C. V. Shank: In Ultrashort Light Pulses, ed. by S. L. Shapiro, Topics in Applied Physics, Vol. 18 (Springer, Berlin, 1977) p. 83-122

137. D. J. Bradley, J. F. Higgins, M. H. Key: Appl. Phys. Lett. 16, 53 (1970)

138. M. Y. Shelev, M. C. Richardson, A. J. Alcock: Appl. Phys. Lett. 18, 354 (1971)

139. M. A. Duguay, J. W. Hansen: Appl. Phys. Lett. 15, 192 (1969)

140. J. Kerr.: Phil. Mag. 50, 337 (1875)

141. A. D. Buckingham: Proc. Phys. Soc. London B69, 344 (1956)

142. G. Mayer, R. Gires: C. R. Acad. Sci. 258, 2039 (1964)

143. B. J. Greene, R. C. Farrow: J. Chem. Phys. 77, 4779 (1982)

144. R. W. Hellwarth: J. Chem. Phys. 52, 2128 (1970)

145. A. C. Chevng, D. M. Rank, R. Y. Chiao, C. H. Townes: Phys. Rev. Lett. 20, 786 (1968)

146. P. M. Rentzepis, M. R. Topp, R. R. Jones, J. Jortner: Phys. Rev. Lett. 25, 1742 (1970)

147. W. S. Struve: Chem. Phys. Lett. 51, 603 (1977)

148. C. G. Morgante, W. S. Struve: Chem. Phys. Lett. 63, 344 (1979)

149. C. G. Morgante, W. S. Struve: Chem. Phys. Lett. 68, 267 (1979)

150. C. G. Morgante, W. S. Struve: Chem. Phys. Lett. 68, 272 (1979)

151. C. G. Morgante, W. S. Struve: Chem. Phys. Lett. 69, 56 (1980)

152. P. P. Ho, R. R. Alfano: Phys. Rev. A 20, 2170 (1979)

153. M. A. Duguay, A. T. Mattick: Appl. Opt. 10, 2162 (1971)

154. S. L. Shapiro, H. P. Broida: Phys. Rev. 154, 129 (1967)

155. W. S. Struve: Opt. Commun. 21, 215 (1977)

156. M. R. Topp, G. C. Orner: Opt. Commun. 13, 276 (1975)

157. M. R. Topp, P. M. Rentzepis: J. Chem. Phys. 56, 1066 (1972)

158. Y. Talmi: Anal. Chem. 47, 658A; 699A (1975)

159. K. S. Petche: In Handbook of Optics, ed. by W. G. Driscoll (McGraw-Hill Book Company, 1978) p. 5-15

160. F. Pellegrino, R. R. Alfano: In Multichannel Image Detectors, ed. by Y. Talmi (American Chemical Society, Washington, 1979) p. 183-198

161. R. G. Neuhauser: The Silicon-Target Vidicon, technical note P.E.-696 (RCA Corporation, Lancaster, PA, 1977)

162. RCA Corporation (Lancaster, PA. 1974) Electro-Optic Handbook (EOH-11)

163. D. M. Hunter, C. J. Strump: Appl. Optics 15, 3105 (1976)

164. A. A. Liff: Color and Black and White Television Theory and Servicing (Prentice-Hall, New York, 1979) p. 28-63

165. J. Reader: J. Opt. Soc. 59, 1189 (1969)

166. A. Penzkofer, A. Seilmeier, W. Kaiser: Opt. Commun. 14, 363 (1975)

167. W. L. Smith, P. Liu, N. Bloembergen: Phys. Rev. A 15, 2396 (1977)

168. W. C. Baird, J. H. Surridge: J. Org. Chem. 35, 3436 (1970)

169. E. C. Lim, J. D. Laposa, J. M. H. Yu: J. Mol. Spectrosc. 19, 412 (1966)

170. R. L. Pineault, C. G. Morgante, W. S. Struve: J. Photochem. 17, 435 (1981)

171. American Society or Metals: Metals Handbook, 9th Ed., Vol. 3 (ASM, Metals Park, Ohio, 1980) p. 794

172. R. C. Hyer, H. D. Sutphin, K. R. Winn: Rev. Sci. Instrum. 46, 1333 (1975)

173. E. J. Woodbury, W. K. Ng: IRE 50, 2347 (1962)

174. G. Eckardt, R. W. Hellwarth, F. J. McClung, S. E. Schwartz, D. Weiner, E. J. Woodbury: Phys. Rev. Lett. 9, 455 (1962)

175. B. P. Stoicheff: Phys. Lett. 7, 186 (1963)

176. N. Bloembergen, P. Lallemand: Phys. Rev. Lett. 16, 81 (1966)

177. N. Bloembergen: Am. J. Phys. 35, 989 (1967)

178. R. R. Alfano, S. L. Shapiro: Phys. Rev. Lett. 24, 584 (1970)

179. R. R. Alfano, L. L. Hope, S. L. Shapiro: Phys. Rev. A 6, 433 (1972)

180. R. R. Alfano, S. L. Shapiro: Phys. Rev. Lett. 24, 592 (1970)

181. W. Werneke, A. Lau, M. Pfeiffer, K. Lenz, H. J. Weigmann, C. D. Thuy: Opt. Commun. 4, 413 (1972)

182. M. Clerc, R. P. Jones, P. M. Rentzepis: Chem. Phys. Lett. 26, 167 (1974)

183. C. A. G. O. Varma, P. M. Rentzepis: J. Chem. Phys. 58, 5237 (1973)

184. R. M. Hochstrasser, R. B. Weisman: In Radiationless Transitions, ed. by S. H. Lin (Academic Press, New York, 1980) p. 317-362

185. A. Penzkofer, A. Laubereau, W. Kaiser: Phys. Rev. Lett. 31, 863 (1973)

186. A. Penzkofer: Opt. Commun. 11, 265 (1974)

187. N. Bloembergen: Opt. Commun. 8, 285 (1973)

188. D. K. Sharma, R. W. Yip, D. F. Williams, S. E. Sugamory, L. T. Bradley: Chem. Phys. Lett. 41, 460 (1976)

189. A. Penzkofer, W. Kaiser: Opt. and Quantum. Electron. 9, 315 (1977)

190. P. N. Butcher: Nonlinear Optical Phenomena, Engineering Experiment Station, Ohio State University, Bulletin 100, 1965

191. P. W. Terhune, P. D. Maker: In Lasers, Vol. 2, ed. by A. K. Levine (Marcel Dekker, New York, 1968) p. 295-372

192. Y. R. Shen: Rev. Mod. Phys. 48, 1 (1976)

193. S. A. Akhmanov, R. V. Khokhlov, A. P. Sukhorukov: In Laser Handbook, Vol. 2, ed. by F. T. Arecchi, E. O. Schulz-Dubois (North Holland Publishing Co., Amsterdam, 1972) p. 1151-1228

194. S. Belke, R. Gase, K. Volger: Opt. and Quantum Electron. 12, 9 (1980)

195. M. D. Levenson: Introduction to Nonlinear Laser Spectroscopy (Academic Press, New York, 1982)

196. E. L. Kerr: ASTM Spec. Tech. Publ. No. 469 (ASTM, Philadelphia, 1969)

197. J. P. McTague, C. H. Lin, T. K. Gustafson, R. Chiao: Phys. Lett. 33A, 82 (1970)

198. Y. R. Shen: Prog. Quantum Electron. 4, 1 (1975)

199. J. H. Morburger: Prog. Quantum Electron. 4, 35 (1975)

200. A. Lugovoi, A. M. Prokhorov: JETP Lett. 7, 117 (1968)

201. M. M. Loy, Y. R. Shen: Phys. Rev. Lett. 22, 994 (1969)

202. R. C. Brewer, J. R. Lifsitz, E. Garmire, R. Y. Chiao, C. H. Townes: Phys. Rev. 166, 326 (1968)

203. R. Y. Chiao, E. Garmire, C. H. Townes: Phys. Rev. Lett. 13, 479 (1964)

204. P. L. Kelley: Phys. Rev. Lett. 15, 1005 (1965)

205. R. R. Alfano, A. Lempicki, S. L. Shapiro: IEEE J. Quantum Electron. QE 7, 416 (1971)

206. E. Garmire: Phys. Lett. 17, 251 (1965); In Physics of Quantum Electronics, ed. by P. L. Kelley, B. Lax, P. E. Tannenwald (McGraw-Hill, New York, 1966)

207. R. W. Hellwarth, F. J. McClung, W. G. Wagner, D. Weiner: Bull. Am. Phys. Soc. 9, 490 (1964)

208. R. W. Terhune, P. D. Maker: Phys. Rev. 137, A816 (1965)

209. R. Chiao, B. P. Stoicheff: Phys. Rev. Lett. 12, 290 (1964)

210. R. Chiao, M. A. Johnson, S. Krinsky, H. A. Smith, C. H. Townes, E. Garmire: IEEE J. Quantum Electron. QE-2, 467 (1966)

211. K. Shimoda: Jap. J. Appl. Phys. 5, 86 (1966)

212. M. J. Colles: Opt. Commun. 1, 169 (1969)

213. A. Penzkofer, A. Laubereau, W. Kaiser: Prog. Quantum Electron. 6, 55 (1979)

214. A. Penzkofer, J. Kraus, J. Sperka: Opt. Commun. 37, 437 (1981)

215. B. Hampel: In UV Atlas of Organic Compounds, Vol. 5 (Plenum Press, New York, 1971), p. M/10

216. W. Yu, R. R. Alfano, C. L. Sam, R. J. Seymour: Opt. Commun. 14, 344 (1975)

217. P. Brounlich, P. L. Kelley: J. Appl. Phys. 46, 5205 (1975)

218. P. Lallemand: In The Raman Effect, Vol. 1, ed. by A. Anderson (Marcel Dekker Inc., New York, 1971) p. 282

219. E. Hecht, A. Zajac: Optics (Addison-Wesley Publishing Co., Reading, 1974)

220. W. J. Smith: Modern Optical Engineering (McGraw-Hill Book Co., New York, 1966)

221. A. Nussbaum: Geometric Optics (Addison-Wesley Publishing Co., Reading, 1968)

222. D. E. Gray (Ed.): American Institute of Physics Handbook, 3rd Edition (1972) p. 6-105

223. R. W. Hellwarth: Prog. Quantum Electron. 5, 1 (1977)

224. V. Sundstrom, P. M. Rentzepis, E. C. Lim: J. Chem. Phys. 66, 4287 (1977)

225. E. J. Land: Proc. Roy. Soc. A305, 457 (1968)

226. M. Dzvonik, S. Yang, R. Bersohn: J. Chem. Phys. 61, 4408 (1974)

227. S. Yang, R. Bersohn: J. Chem. Phys. 61, 4400 (1974)

228. A. Freedman, S. Yang, M. Kawasaki, R. Bersohn: J. Chem. Phys. 72, 1028 (1980)

229. K. F. Freed, Y. B. Band: In Excited States, Vol. 3, ed. by E. C. Lim (Academic Press, New York, 1978) p. 109-201

230. M. Shapiro, R. Bersohn: Ann. Rev. Phys. Chem. 33, 409 (1982)

231. W. M. Gelbart: Ann. Rev. Phys. Chem. 28, 323 (1977)

232. S. P. McGlynn, T. Azumi, M. Kinoshita: Molecular Spectroscopy of the Triplet State (Prentice-Hall, Inc., Englewood Cliffs, 1969)

233. R. A. Durie, T. Iredale, A. H. Kingsbury: Nature 164, 786 (1949)

234. T. Iredale, J. W. White: Trans. Faraday Soc. 56, 1719 (1960)

235. A. Levy, D. Meyerstein, M. Ottolenghi: J. Phys. Chem. 77, 3044 (1973)

236. R. L. Hummel, K. Ruedenberg: USAEC Res. Dev. Rep. IS-450 (Office of Technical Services, Washington, 1964)

237. T. L. Cottrell: The Strengths of Chemical Bonds, 2nd edition, (Academic Press, New York, 1958)

238. F. Grieser, J. K. Thomas: J. Chem. Phys. 73, 2115 (1980)

239. N. Nakashima, N. Mataga: Chem. Phys. Lett. 35, 487 (1975)

240. K. Hamanoue, S. Hirayama, T. Kakayama, H. Teranishi: J. Phys. Chem. 84, 2074 (1980)

241. R. M. Hochstrasser, S. K. Lower: J. Chem. Phys. 40, 1041 (1964)

242. D. Huppert, S. D. Rand, A. Reynolds, P. M. Rentzepis: J. Chem. Phys. 77, 1214 (1982)

243. P. M. Rentzepis: Science 202, 174 (1978)

244. R. W. Anderson, R. Hochstrasser, G. Scott: Chem. Phys. Lett. 32, 204 (1975)

245. N. J. Turro, V. Ramamurthy, W. Cherry, W. Farneth: Chemical Reviews 78, 125 (1978)

246. T. J. Chaung, G. W. Hoffman, K. B. Eisenthal: Chem. Phys. Lett. 25, 201 (1974)

247. A. Kearvell, F. Wilkinson: J. Chim. Phys. Special Edition, Transitions Non Radiatives Dan Les Molecules, 125 (1970)

248. E. J. Bowen, J. Sahu: J. Phys. Chem. 63, 4 (1959)

249. W. R. Ware, B. A. Baldwin: J. Chem. Phys. 43, 1194 (1965)

250. R. G. Bennett, P. J. McCartin: J. Chem. Phys. 44, 1969 (1966)

251. W. Siebrand: J. Chem. Phys. 47, 2411 (1967)

252. W. Siebrand, D. Williams: J. Chem. Phys. 46, 403 (1967)

253. G. D. Gillispie, E. C. Lim: J. Chem. Phys. 65, 2022 (1976)

254. G. D. Gillispie, E. C. Lim: Chem. Phys. Lett. 63, 355 (1979)

255. R. Pariser: J. Chem. Phys. 24, 250 (1956)

256. R. E. Kellogg: J. Chem. Phys. 44, 411 (1966)

257. Y. H. Meyer, R. Astier, J. M. Leclereq: J. Chem. Phys. 56, 801 (1972)

258. R. O. Campbell, R. Liu: J. Amer. Chem. Soc. 95, 6560 (1973)

259. G. D. Gillispie, E. C. Lim: Chem. Phys. Lett. 63, 193 (1979)

260. P. Avouris, W. M. Gelbart, M. A. El-Sayed: Chem. Rev. 77, 793 (1977)

261. S. Murata, C. Iwanaga, T. Toda, H. Kukubun: Chem. Phys. Lett. 13, 101 (1972)

262. B. Dick, G. Hohlneicher: Chem. Phys. Letts. 83, 615 (1981)

263. R. P. Steiner, J. Michl: J. Amer. Chem. Soc. 100, 6861 (1978)

264. R. Astier, Y. Meyer: In The Triplet State, ed. by A. B. Zahlan (Cambridge University Press, Cambridge, 1967) p. 447

265. R. D. Stuart: An Introduction to Fourier Analysis (Methnen & Co., Ltd., London, 1961)

266. D. O'Shea, W. R. Callen, W. Rhodes: Introduction to Lasers and their Applications (Addison-Wesley Publishing Co., Reading, 1977)

267. A. Yariv: J. Appl. Phys. 36, 338 (1965)

268. J. Herrmann, F. Weidner: Optical and Quantum Electron. 11, 119 (1979)

269. G. H. New: J. Quantum Electron. QE-10, 115 (1974)

270. F. Zernike, J. Midwinter: Applied Nonlinear Optics (John Wiley & Sons, New York, 1973)

271. D. Anafi, J. Machewirth: Optical Spectra 5, 12 (1975)

ACKNOWLEDGMENTS

As with the majority of students who obtain their doctorate, I am deeply indebted to my advisor--Professor Walter S. Struve. His conscientious direction and seemingly inexhaustible patience has benefited my graduate education immensely. Dr. Struve's comments and physical insights about chemistry and physics made not only the area of picosecond spectroscopy but also many other areas comprehensible.

I acknowledge Dr. Richard Johnson and Thomas Stierman for supplying the iodoanthracenes and their preliminary photoproduct analyses, Richard Pineault for his diligent technical assistance, especially in the computer programming, and Carolyn Taylor for typing the manuscript.

I owe an enormous debt of gratitude to one of the few people in the world who would probably try to collect, David Hart. Not only was this poor soul unmercifully subjected to proofreading drafts, he reliably waded through Iowa State's bureaucratic quagmire to facilitate the completion of this dissertation. I give him my sincerest thanks with the hope that his thesis takes fewer pages (and years). John Hedstrom provided the essential third viewpoint for a trio--he, Dave, and myself--who tried to enjoy reasonable conversation, good science, and cold beer simultaneously (these activities turn out to be mutually exclusive). The other members of the Struve group--Stanley Prybyla, Richard Pineault, Bob Crackel, and Phillip Anfinrud--deserve thanks for considerably broadening the spectrum (see Chapter Three) of social and scientific interactions available within the group.

In addition, there are many who have raised the quality of life in Ames for me such as Lester Hughes, David Evans, Robert Cole, the CARG group, Cherie Garretson, and Sally Dunphy. These friendships and many unnamed others will be truly missed, but hopefully maintained despite distances and time.

Finally, I express my warmest thanks to Tamara Lorenz (and her six friends) for being my good friend for four enlightening years.

APPENDIX A

It is well-known from Fourier theory that extremely short duration pulses are created from a broad range of frequencies locked together in phase (265). To generate ultrashort pulses from a Nd-glass laser, the large number of longitudinal (or axial) modes available due to the extensive lasing bandwidth are locked in phase to produce the pulse. Longitudinal modes are frequencies within the laser's bandwidth which simultaneously exceed the gain threshold necessary for lasing and fulfilling the resonance conditions for stable oscillation in the laser cavity (111-114). From the latter condition, it can be shown that the longitudinal modes are spaced apart in frequency by

$$\Delta\nu_{\ell} = \frac{c}{2L} \qquad (A.1)$$

where c is the speed of light and L is the length of the resonator.

Figure A-1 shows schematically the longitudinal modes which typically could oscillate. The overall number of modes, N, which can oscillate is equal to the lasing bandwidth, $\Delta\nu$, divided by the mode spacing,

$$N = \frac{\Delta\nu}{\Delta\nu_c} \quad . \qquad (A.2)$$

In the Nd-glass media, $\Delta\nu$ is approximately 8 THz (~150 Å at 1.06 microns) and for an one meter cavity, the number of longitudinal modes is ~5 x 10^4.

Each of the modes oscillates with a random phase resulting in interference between the modes. This causes the output of the laser to fluctuate in a chaotic manner and reduces both the maximum intensity

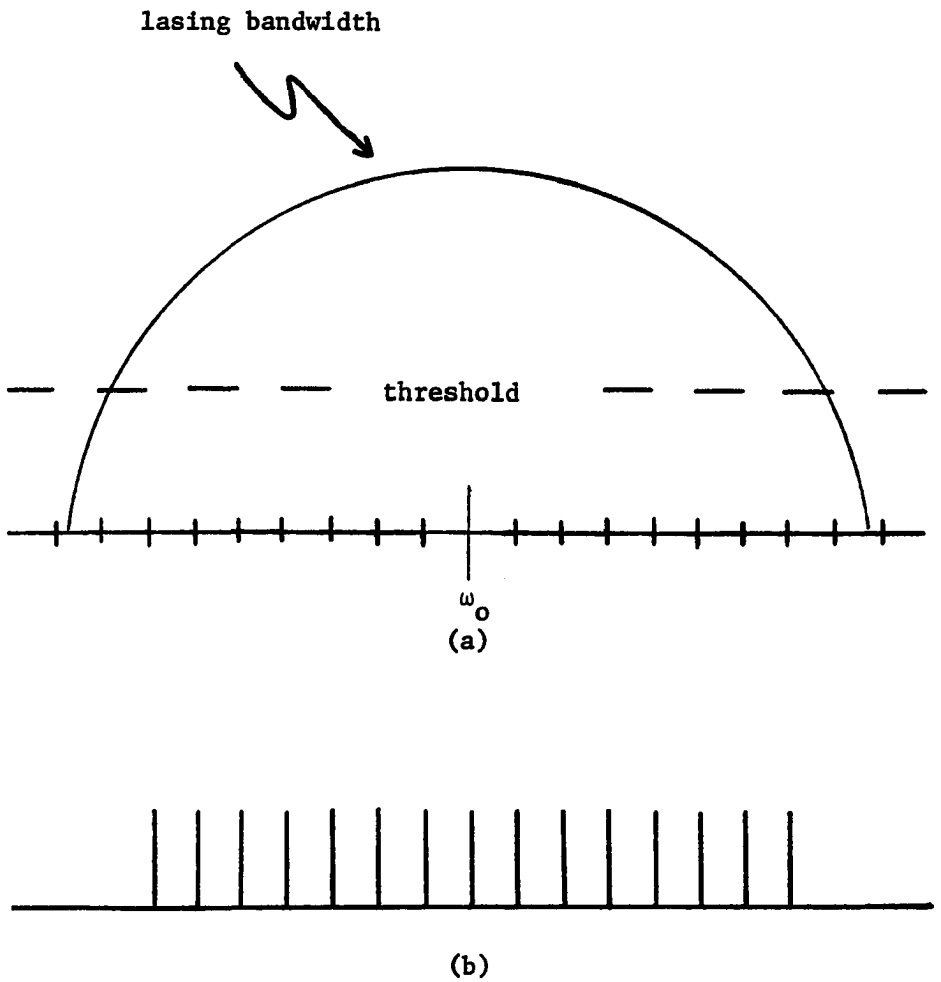

Figure A-1. Longitudinal modes of laser
(a) ω_o is the center frequency of the lasing bandwidth
(b) the longitudinal modes exceeding threshold and c/2L apart in frequency

possible and the temporal coherence (113). If a definite phase correlation was established between the modes, the laser output becomes pulsed, temporally coherent, extremely intense, and of a duration that is inversely proportional to the number of modes locked together. The two different conditions, phases random and locked, are emphasized in Figure A-2a and Figure A-2b, respectively. (This figure is based on a similar one given by O'Shea et al. (266).)

A simple mathematical description of modelocking can be presented as follows.

The total instantaneous field at time t can be expressed as:

$$E_T(t) = \sum_{\frac{-N-1}{2}}^{\frac{N-1}{2}} E_o e^{i[(\omega_o + n\omega_\ell)t + \phi_n]} \qquad (A.3)$$

where ω_o is the frequency (in radians/sec) of the lasing bandwidth $\Delta\omega$, ω_ℓ is the mode spacing ($= 2\pi\Delta\nu_\ell$), N is the number of longitudinal modes, and ϕ_n is a random phase associated with a mode n. For simplicity, the amplitude for each mode has been assumed to be the same and equal to E_o. If one locks all the phases together and arbitrarily sets it equal to zero, equation A.3 becomes

$$E_T(t) = E_o e^{i\omega_o t} \sum_{\frac{-N-1}{2}}^{\frac{N-1}{2}} e^{in\omega_\ell t} \qquad (A.4)$$

or

$$E_T(t) = E_o e^{i\omega_o t} \frac{\mathrm{Sin}(N\omega_\ell t/2)}{\mathrm{Sin}(\omega_\ell t/2)} \quad . \qquad (A.5)$$

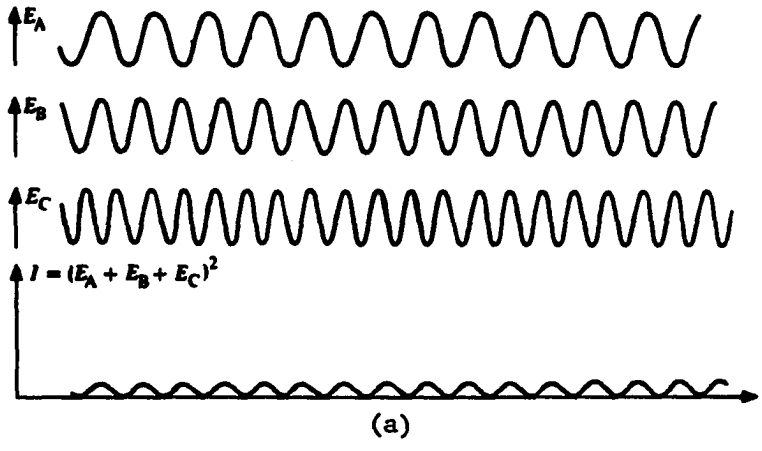

(a)

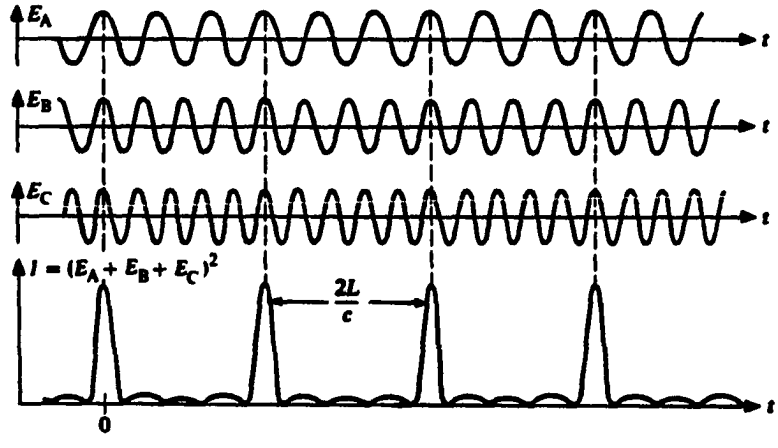

(b)

Figure A-2. Random phase (a) and modelocked (b) laser outputs from three longitudinal modes. From ref. (226)

The analytical properties of equation A.5 have been discussed in the literature (113, 267), some of which are:

(1) the power, proportional to E(t)E(t)*, is emitted in a train of pulses with a period of $T = 2\pi/\omega_c$;

(2) the peak power of the pulse equals N times the average power;

(3) the individual pulse width is $\tau = T/N$.

From property (3), the pulse duration is approximately,

$$\tau \approx \frac{T}{N} = \frac{2\pi}{\omega_\ell} \cdot \frac{\omega_\ell}{\Delta\omega} = \frac{1}{\Delta\nu} \qquad (A.6)$$

or the pulse duration is inversely proportional to the lasing bandwidth as mentioned earlier.

Locking the phases of longitudinal modes is generally accomplished by passive modelocking by inserting a saturable absorber dye solution within the laser cavity. In the inchoative lasing stages, the emission from the lasing media is spontaneous and fluctuates considerably in intensity and duration. The saturable absorber dye which has an absorption coefficient which decreases with intensity will preferentially absorb the weaker pulses and transmit the stronger ones. These latter pulses, allowed to undergo gain, increase in intensity and begin to oscillate modulated at a frequency roundtrip time for the laser cavity, $\frac{2L}{c}$. The modulation imposed by the dye cell causes sidebands to form at $\pm \frac{2L}{c}$ in phase. As the pulse evolves through numerous passes through the cavity, it very rapidly draws in more modes in phase until a

substantial number of longitudinal modes are oscillating and a very short pulse is formed. More quantitative treatments of modelocking emphasizing the statistical nature of the process can be found in the literature (268, 269).

The saturable absorber dye used in our system was Kodak #9860 with spectroquality dichloroethane concentrated to ~61% transmission at 1.06 microns. The dye bleaches at an intensity of ~65 Mw/cm^2 and has a lifetime on the order of 9 picoseconds (117).

APPENDIX B

To obtain visible or ultraviolet wavelengths from the 1.06 micron fundamental of the Nd-glass laser, we utilized optical harmonic generation processes in addition to the continuum generation discussed in Chapter 3. Second harmonic generation (SHG) and third harmonic generation was used to produce light at approximately 532 nm and 354 nm, respectively.

To frequency double, two 1.06 micron fundamental photons were mixed to produce one second harmonic photon at 532 nm; the third harmonic at 354 nm was produced by mixing a fundamental photon and a 532 nm photon.

When an intense electromagnetic field, such as those associated with a laser, propagates through a dielectric medium, it induces a polarization wave which departs from the typical linear response observed in optical phenomena. In the presence of large electric fields, the polarization can be cast in terms of a power expansion of the source electric fields,

$$P = \chi_1 E + \chi_2 E^2 + \chi_3 E^3 + \ldots \qquad (B.1)$$

where the χs are the electric susceptibilities. χ_1 is associated with linear phenomena such as the index of refraction and one photon absorption; χ_2 governs three photon interactions, $\omega_1 + \omega_2 \rightarrow \omega_3$, hence is responsible for harmonic generation. The higher order terms, χ_3 in particular, relevant to continuum generation are discussed in Chapter 3.

If one assumes a sinusoidal fundamental electric field,

$$E = E_o \cos \omega_1 t \qquad (B.2)$$

and neglects terms higher than χ_2, equation B.1 can be written,

$$P = \chi_1 E_o \cos \omega_1 t + \frac{E_o^2}{2} \chi_2 \{1 + \cos 2\omega_1 t\} \quad . \qquad (B.3)$$

From equation B.3, the second order term produces a component in the polarization wave with a frequency $2\omega_1$ which in turn will radiate at the second harmonic frequency. If the source electric fields has two frequency components, ω_1 and ω_2, the resulting nonlinear polarization would have sum, $\omega_1+\omega_2$ and difference, $\omega_1-\omega_2$, in addition to the doubled frequencies, $2\omega_1$ and $2\omega_2$.

For efficient energy transfer between the polarization wave and the radiated electromagnetic field, the two waves must conserve energy, $h\omega_1 + h\omega_2 = h\omega_3$, and momentum, $k_1 + k_2 = k_3$. Due to dispersion in a condensed medium, the nonlinear polarization wave vector k_1+k_2 is not equal to k_3 but has a phase mismatch of Δk. This mismatch results in the "driven" polarization wave becoming decoupled from the free radiated wave after propagating a short distance within the medium ending the conversion process.

To phase match the two waves ($\Delta k = 0$), a standard technique is using a birefringent crystal such as potassium dideuterium phosphate, KD*P, as the nonlinear medium and angle tuning it (270). In a birefringent crystal, the index of refraction depends on the orientation of the polarization vector and propagation vector with respect to the

crystal optic axis.

This variation in the extraordinary index of refraction, n_e, with the angle θ between the direction of propagation and optic axis is given by (270)

$$n_e(\theta) = \frac{n_o n_e}{(n_e^2 \sin^2\theta + n_o^2 \cos^2\theta)^{\frac{1}{2}}} \qquad (B.4)$$

where n_o is the ordinary index of refraction and n_e is the extraordinary index with $\theta = 90°$. By proper choice of propagation direction and polarization, one can set $\Delta k = 0$ for the three wave vectors of interest. If the two input waves have the same polarization, the process is termed type I phasematching or if they are orthogonal, type II phase matching (270).

In our experiments, we used KD*P as the media for generating the optical harmonics. KD*P is often used for Nd-glass and Nd.YAG laser systems because it can be easily grown as large, optical homogeneous crystals, has a high optical damage threshold of ~6 GW/cm^2 and has a relatively minimal absorption of 0.4% to 0.5% at 1.06 microns. This last property reduces the deleterious effects of heat on the index of refraction (271).

The 1.06 micron fundamental of our laser was emitted as linearly polarized light so in the second harmonic conversion process, $\omega_1 + \omega_1 \rightarrow \omega_2$, type I phase matching was used with the resultant second harmonic polarized orthogonal to the input fundamental. The second harmonic and residual fundamental was then directed into a second KD*P crystal to produce the 354 nm third harmonic via a type II process (Figure B-1).

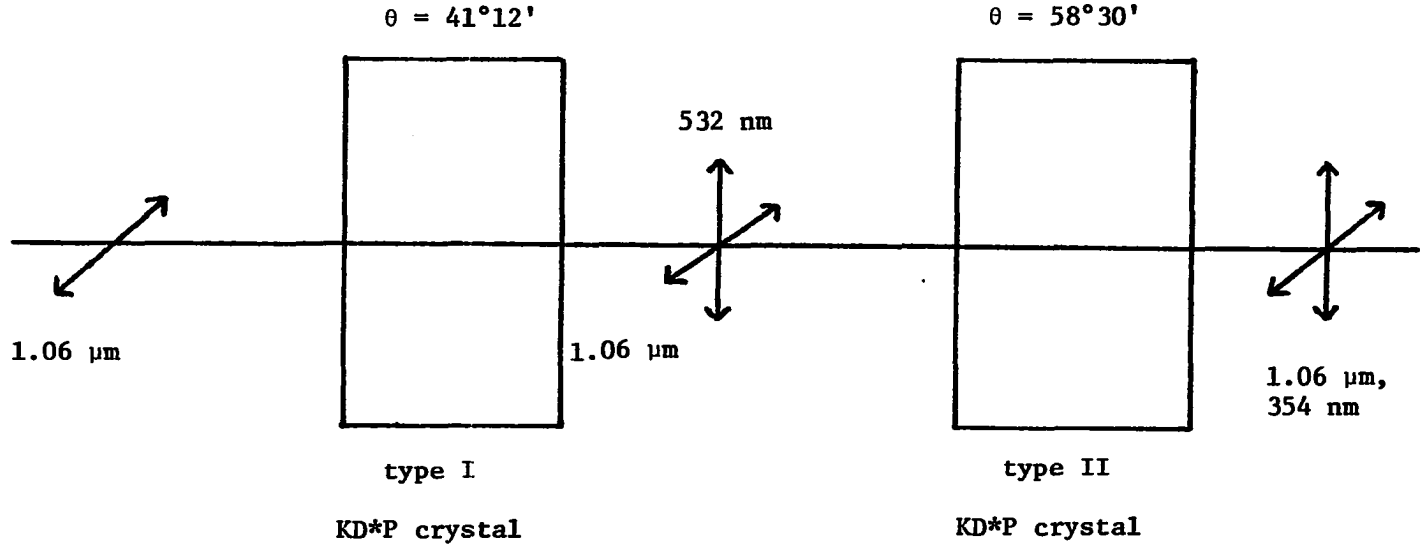

Figure B-1. Second and third harmonic generation

Both KD*P crystals were obtained from Lasermetrics Inc. (Teaneck, N.J.) and cut at $\theta = 41°12'$ and $58°30'$ for type I phasematching (SHG) and type II phasematching (THG), respectively (271). More explicit descriptions of optical harmonic generation are widely available (113, 270).

APPENDIX C

The control and synchronization of the electronic systems for transient absorption experiments was accomplished by the vidicon-Biomation interface. A description of these circuits is given in this appendix. The interface allows several adjustable parameters to be preset before the spectral data are gathered. The time between charging of the laser flashbanks and the generation of signals for firing the laser and strobing data points from the video signal is controlled by a manually set front panel switch, variable from 5-20 seconds in increments of 5 seconds. The spatial positions on the vidicon array that were sampled by the data gathering strobe pulses are governed by two independently variable potentiometers on the front panel. After these parameters have been set and the internal counter started by a manual push button, the various timing sequences are derived from the vertical and horizontal blanking pulses generated by the Cohu camera assembly. All three camera-generated signals--video, horizontal and vertical blanking pulses--are connected via shielded BNC cables to the interface box. Both the 60 Hz vertical blanking signal and the 15.75 kHz horizontal blanking signals are passed through Schmitt triggers to generate clean TTL waveforms which have the same frequency as the blanking pulses. The vertical blanking pulses are directed into a series of decade counters configured to issue the laser fire pulse after accumulating a prerequisite number, determined by the preset time delay switch, of 60 Hz pulses. The 15.75 kHz horizontal pulses are used for the data strobing and background suppression.

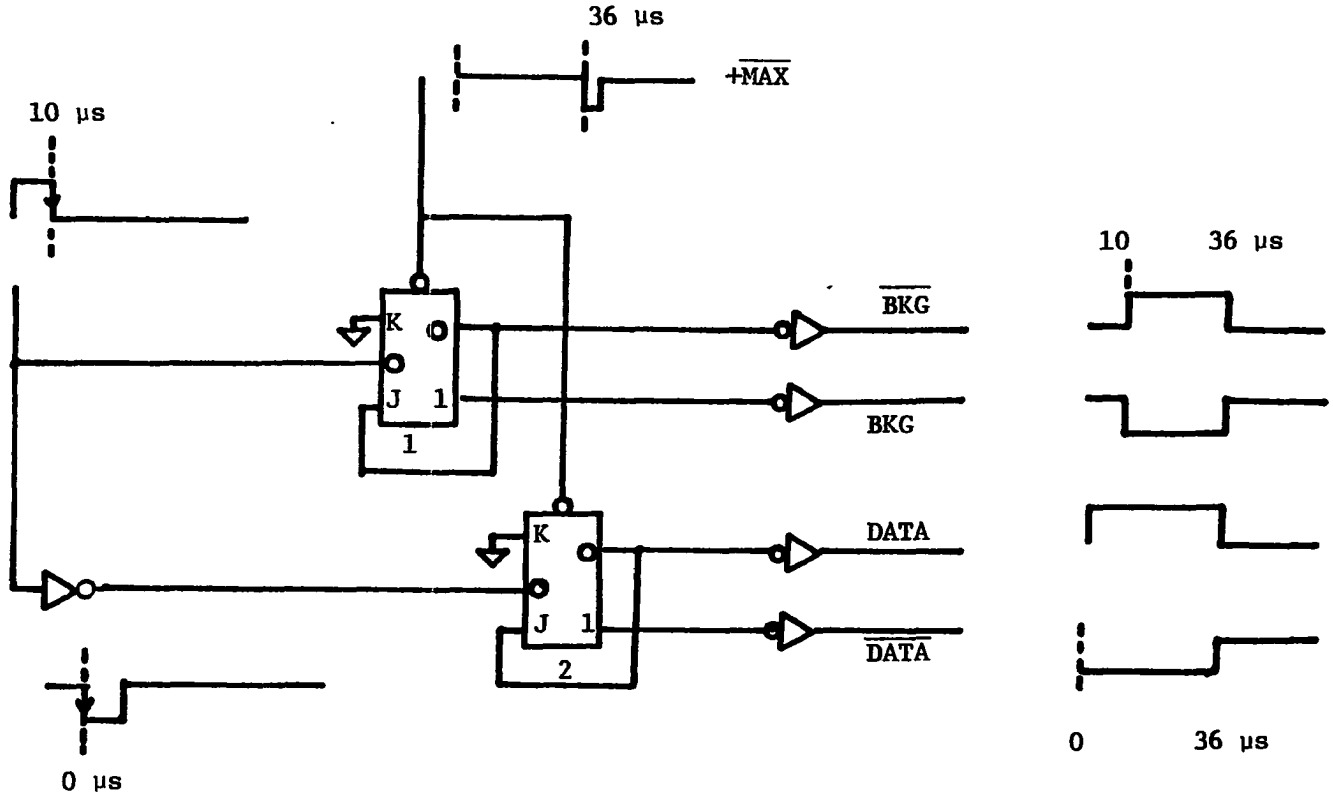

Figure C-1. JK flipflop circuit used to generate DATA and BKG signals

To follow the discussion of the following circuits, it is important to note that the JK flipflop, timing generator, and strobe circuits are interactive and provide feedback to each other throughout the duration of the 63.5 microsecond horizontal scan. The zero time for all of the wave forms in this appendix is the start of the horizontal blanking pulse.

Figure C-1 illustrates the behavior of the JK flipflop circuit. The horizontal blanking signal is fed directly into flipflop 1, the background (BKG) flipflop. In contrast, an inverted horizontal signal is fed into flipflop 2, the data flipflop. Both JK flipflops (74107) have their K inputs grounded and set inputs high. In this configuration, the 1 output will go high upon being clocked by a falling pulse and remain that way until grounded by a simultaneous ground of the clear input. In the case of the BKG flipflop, the 1 output goes high at 10 μs due to the falling edge at 10 μs of the horizontal pulse; the J input and the 0 input, tied together, fall to low level simultaneously with the rise to high level at 1. These outputs remain constant until the clear input is grounded by the $+\overline{MAX}$ pulse (vide infra) at 36 μs resulting in both outputs changing states. Both output signals are inverted, shown as BKG and $\overline{BKG}$, before being further processed. A similar generation of signals is occurring at the DATA flipflop. The 1 output goes high at 0 μs since the inverted horizontal signal has a falling edge at 0 μs. As with the BKG flipflop, the J input and 0 output are tied together in the opposite state of the 1 output. The flipflop also receives the $+\overline{MAX}$ pulse at 36 μs and each output changes state. The output pulses, DATA

and $\overline{\text{DATA}}$, are both inverted before being conveyed to the background suppression circuit.

As mentioned in Chapter 2, the data only imaged on a small portion of the vidicon surface; the rest of the vidicon grid only contributes a dark current to the video signal when it is swept. Since this dark current can be significant, approximately 8nA when typical signal currents from visible radiation are approximately 140-150 nA for a RCA 4532 silicon vidicon, the background suppression circuit averages the video signal derived from the dark portion of the vidicon and then subtracts this averaged value from the video signal carrying the data. The four signals generated by the dual JK flipflops are used as gating signals to control FET gates that direct the video signal to either a background averaging filter or a data averaging filter (both are lag filters). A general schematic of this is presented in Figure C-2. During the first half of the horizontal sweep, FET 2 is opened by the $\overline{\text{BKG}}$ waveform. This allows the video signal to be averaged by operational amplifier (op amp) 1. The RC time constant of 4.4 ms is approximately equal to the duration of 70 horizontal sweeps. Also during the first half of the horizontal sweep, the $\overline{\text{DATA}}$ waveform keeps FET 4 open, disconnecting the video from op amp 2, the data averager. After the gating signals are changed at 36 μs by the timing generator, the background averager is cut off from the video signal and the data averager is connected. In op amp 2, the RC time constant is 2 μs, so the averaged signal is updated more than 30 times during the last half of a horizontal scan. Since the images of the two spectra are separated

Figure C-2. Background suppression circuit

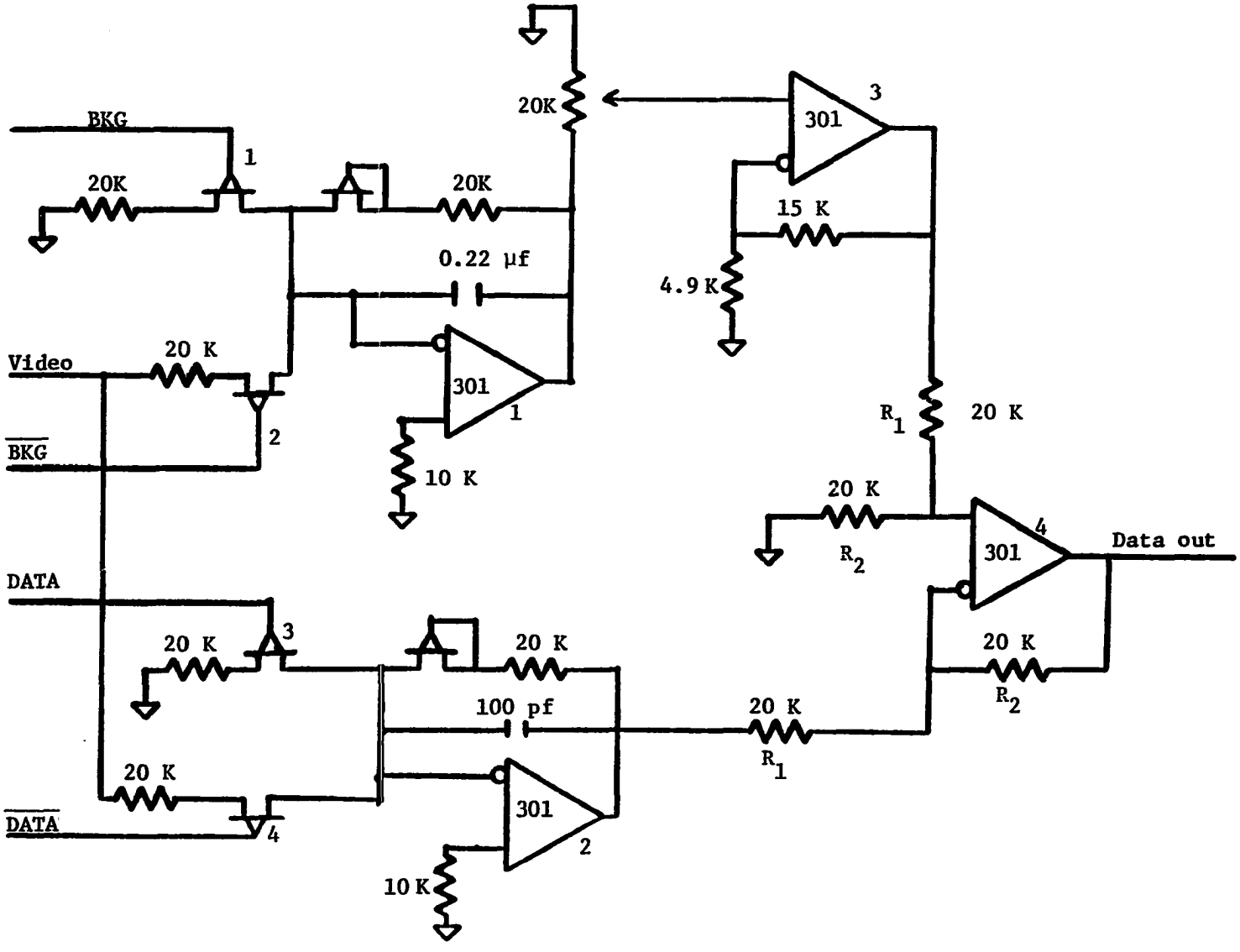
BKG
1
20K
20K
20K
0.22 µf
301
3
15 K
4.9 K
Video
20 K
2
BKG
10 K
301
1
R1
20 K
20 K
R2
301
4
Data out
DATA
20 K
3
20 K
100 pf
20 K
R1
20 K
R2
20 K
301
2
DATA
4
10 K

by ~2-3 mm on the vidicon surface, the averaged data signal is derived from either the I or I_0 spectra, but not both. The averaged background signal is passed through a noninverting amplifier with offset balancing, and then subtracted from the data signal by a difference amplifier. The output signal is then directed into the Biomation transient recorder where it will be stored if the Biomation external time base has been triggered by the data strobing pulses (vide infra).

The crucial circuit is the Timing Generator circuit (Figure C-3). This circuit orchestrates the generation of the data strobing pulses, JK flipflop circuits, and background suppression circuit by use of feedback. Two regulated voltages, $-V_{REF}$ and $+V_{REF}$, are integrated alternatively by the gating input waveforms $\overline{\text{CHARGE}}$ and $\overline{\text{DISCHARGE}}$, respectively. The $\overline{\text{CHARGE}}$ waveform originates in the JK flipflop circuit initiated by the horizontal blanking pulse. This waveform opens FET 1 at +10 μs, the onset of horizontal scanning of the Si array. When the integrated output voltage of op amp 1 exceeds +2 volts, op amp 2, a 710 voltage comparator, goes positive. The output from op amp 2 is defined as +MAX on the circuit diagrams (Figures C-1, C-3). This positive-going pulse is inverted and is used to clear the JK flipflops (Figure C-1), setting their 1 outputs to ground. Since the $\overline{\text{CHARGE}}$ pulse is derived from the JK flipflops, a change of state in these flipflops results in a concomitant change in $\overline{\text{CHARGE}}$ which switches off FET 1 (Figure C-3), halting the integration of $-V_{REF}$.

Concurrently to acting on the JK flipflops, the +MAX pulse goes to a RS flipflop circuit (Figure C-4) which generates the $\overline{\text{DISCHARGE}}$

Figure C-3. Timing generator circuit. The 301 circuits are configured as operational amplifiers; the 710 circuits are identical comparators

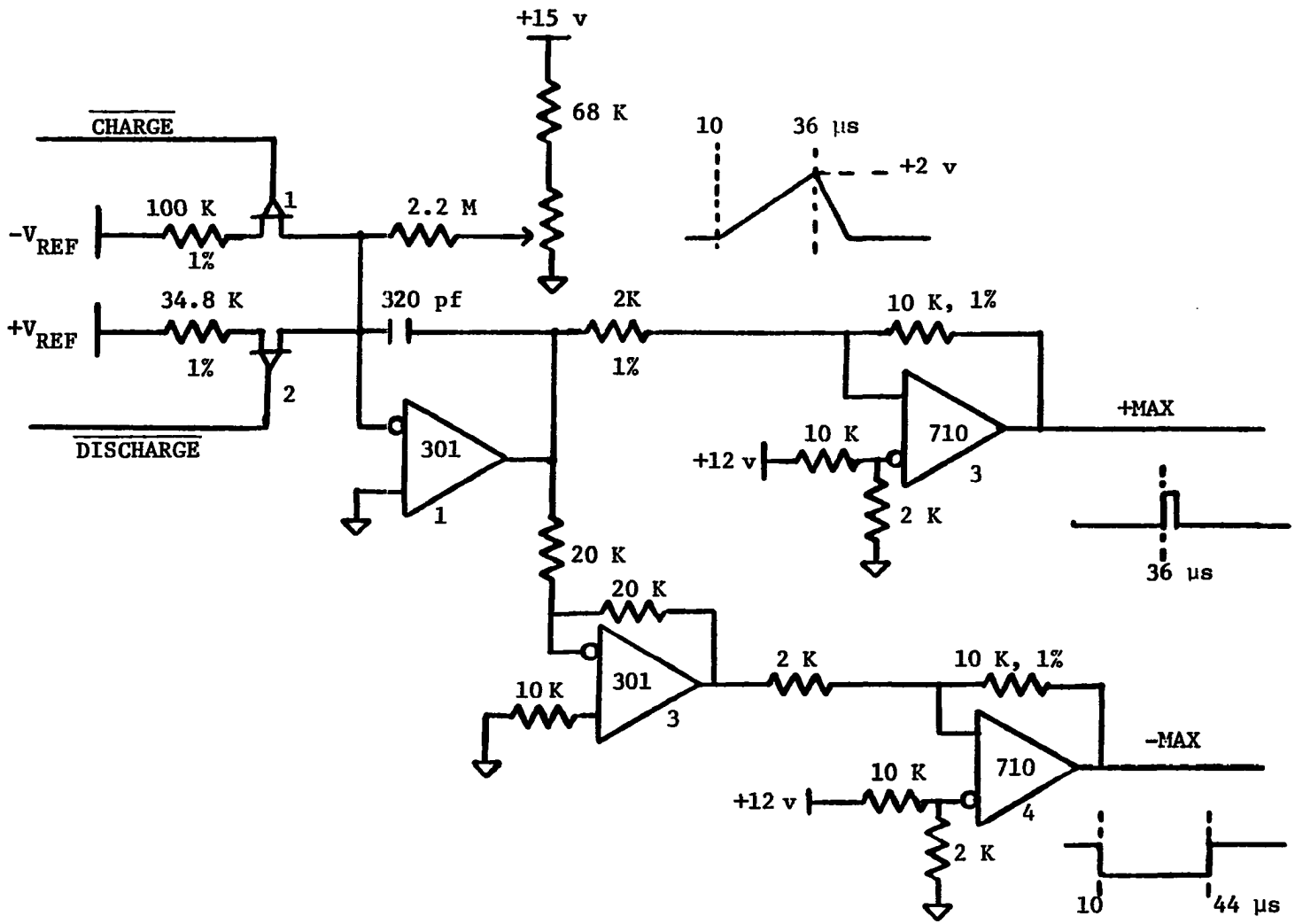
+15 v
68 K
CHARGE
100 K
1%
1
-V REF
2.2 M
10
36 µs
+2 v
34.8 K
1%
+V REF
320 pf
2K
1%
10 K, 1%
2
DISCHARGE
301
1
710
3
+MAX
10 K
+12 v
2 K
36 µs
20 K
20 K
10 K
301
3
2 K
10 K, 1%
710
4
-MAX
10 K
+12 v
2 K
10
44 µs

pulse, switching on FET 2 (Figure C-3). When FET 2 is open, the integrated voltage positive level begins to drop, causing the comparator (op amp 2) to switch to its low state. Because the input resistance of $+V_{REF}$ is one third of the input resistance of $-V_{REF}$, the respective RC constants differ by a factor of 3; this produces an asymmetrical triangular waveform in the output voltage of op amp 1. Simultaneously, an identical voltage level discriminator to op amp 2 (op amp 4) has been receiving an inverted integrated signal via op amp 3, and has produced the waveform -MAX which is the second input to the data strobing RS flipflop (Figure C-4).

Both +MAX and -MAX waveforms are inverted and passed into the RS flipflop circuit (Figure C-4). The falling edges of the resulting pulses, Q and $\overline{Q}$, are used to trigger 74121 monostable multivibrators (MM1, MM2). The duration of the pulse created at either MM1 or MM2 is controlled by an independently variable external resistor which is part of the external RC time constant of the monostable. Each of these monostable pulses triggers another monostable (MM3, MM4). MM3 and MM4 are configured to produce 1 μs pulses which are directed to the external time base ($\overline{XTB}$) of the Biomation. Video signals present at the input of the Biomation coincident with the $\overline{XTB}$ pulses are then recorded. The variable resistors governing MM1 and MM2 allow one to adjust the timing between the activating pulses, +MAX and -MAX, and the generation of the two data strobing pulses. A timing diagram of all the relevant waveforms is shown in Figure C-5.

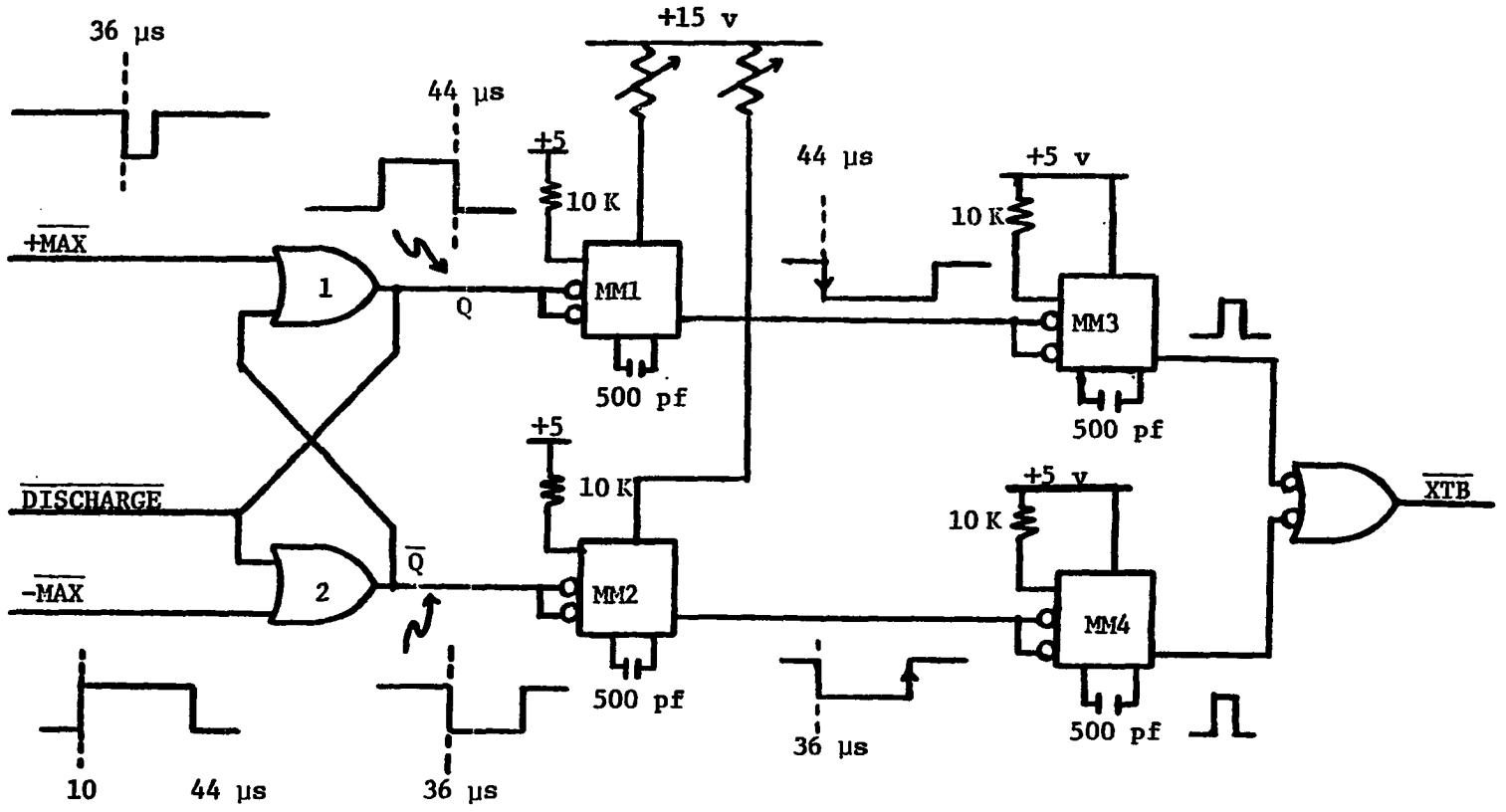

Figure C-4. Data strobe pulse generator

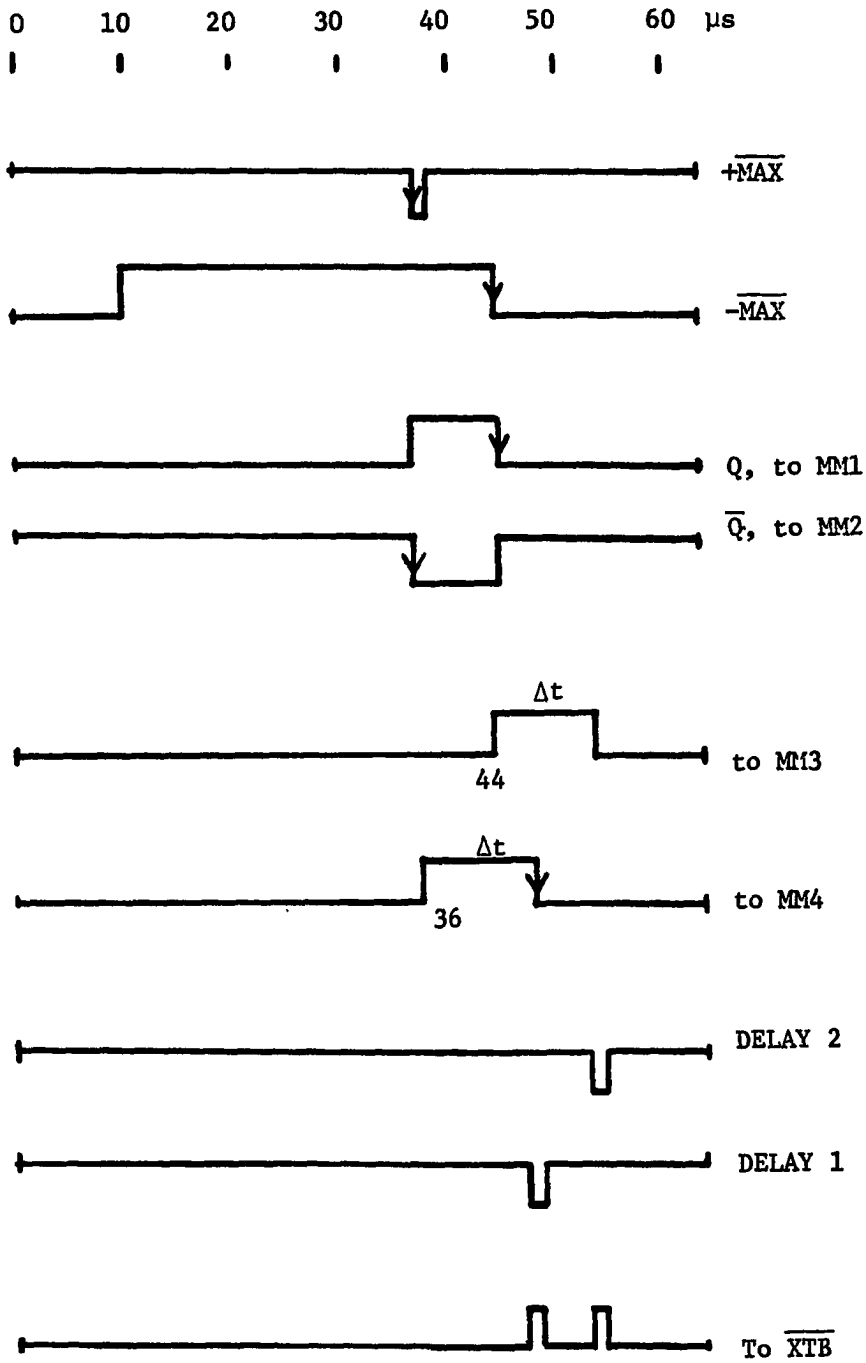

Figure C-5. Timing diagram for DATA strobe pulse circuit